Electrochemical syntheses assisted by new nano-structured catalysts

Davide Scarpa

UNIVERSITY OF SALERNO

DEPARTMENT OF INDUSTRIAL ENGINEERING

Ph.D. Course in Industrial Engineering
Curriculum in Chemical Engineering - XXXIV Cycle

Ph.D. thesis in

ELECTROCHEMICAL SYNTHESES ASSISTED BY NEW NANO-STRUCTURED CATALYSTS

Supervisor
Prof. Maria Sarno

Ph.D. student
Davide Scarpa

Scientific Referees
Prof. Todor Batakliev
Dr. Sergio Galvagno

Ph.D. Course Coordinator
Prof. Francesco Donsì

Academic Year
2022/2023

Acknowledgements

First and foremost, I would like to express my sincere gratitude to my supervisor, Prof. Maria Sarno, for her invaluable advice, continuous support and great patience during all the course of my PhD study. Her immense knowledge and plentiful experience have encouraged me during all the time of my academic research and daily life. I would also like to thank my PhD coordinator, Prof. Francesco Donsì, for his constant availability and great kindness in the technical as well as moral support of my study. Moreover, my gratitude extends to my scientific referees, Prof. Todor Batakliev and Dr. Sergio Galvagno, for their insightful and precious comments which encouraged me to widen my research from various perspectives. Finally, I would like to thank all my colleagues and lab members for the kind help and support they gave me during these formative years.

List of publications derived from the project

M. Sarno, E. Ponticorvo, **D. Scarpa**, *PtRh and PtRh/MoS_2 nano-electrocatalysts for methanol oxidation and hydrogen evolution reactions*, Chemical Engineering Journal, 377 (2019) 120600. https://doi.org/10.1016/j.cej.2018.12.060

M. Sarno, E. Ponticorvo, **D. Scarpa**, *Active and stable Ruthenium/Osmium Based Electrocatalysts-based electrocatalyst for Hydrogen Evolution by Seawater Splitting,* Chemical Engineering Transactions, 74 (2019) 1209-1314. https://doi.org/10.3303/CET1974219

M. Sarno, E. Ponticorvo, **D. Scarpa**, *Active and stable graphene supporting trimetallic alloy-based electrocatalyst for hydrogen evolution by seawater splitting,* Electrochemistry Communications, 11 (2020) 106647. https://doi.org/10.1016/j.elecom.2019.106647

D. Scarpa, M. Sarno, *Single atom catalysts for the electro-reduction of CO_2 to both CO and syngas: a review*, Catalysts, 12 (2022) 275. https://doi.org/10.3390/catal12030275

Contents

List of Figures

List of Tables

Abstract

Nowadays, the necessity of a full transition towards green chemistry has become of fundamental importance. In order to guarantee such transition, an increasing reduction of fossil-based sources and, consequently, a growing shift towards recycled and renewable resources would be the most feasible and desirable idea. Among renewables, molecular hydrogen gas (H_2) is one of the most promising energy carriers for the future. Although 95% of the global hydrogen is currently produced from fossil fuels, turning to the so-called sustainable "green hydrogen" is of such fundamental relevance for the development of a carbon-neutral economy. Water electrolysis enables the generation of H_2 at its highest level of purity and at the lowest temperatures when compared to all the other hydrogen generation processes, starting from an easily available and economic source such as water, and with the possibility of receiving as input energy the one from renewables, hence overcoming also the issues related with them. Nano-structured platinum (Pt)-based electrocatalysts and their derivatives are by no means the most efficient catalysts towards the cathodic hydrogen evolution reaction (HER) in acid electrolyte solutions. However, their industrial-scale production and application have been significantly limited by the scarce availability and high price of Pt. In view of all this, as well as by considering that platinum is anyhow indispensable in the formulation of efficient HER electro-catalysts, the primary objective of the following PhD research project has been to design, with the help of Nanotechnology, new nano-structured catalysts for the hydrogen evolution reaction (HER) with the purpose of: (i) increasing catalytic performance compared to current literature and, at the same time (ii) using a reduced amount of platinum and (iii) studying new combinations of small quantities of other metals with platinum, also adopting more economic and, at the same time, highly efficient supports. Therefore, two new nano-electrocatalysts were synthesized, PtRh and PtRh/MoS_2, with a scalable, simple, and cost-effective bottom-up wet chemistry synthesis approach. Subsequently, the samples were extensively characterized and their electrocatalytic properties for HER were evaluated, proving to be more efficient than most of the current HER catalysts reported in the literature. Throughout this study, carried out during the first year of the PhD course,

another important issue emerged: distilled water adopted in the electrolytic cell is obtained only after a series of expensive and complex purification steps, followed by the addition of either acid or basic electrolytes, which obviously increase the total costs of the process. Considering this, an interesting and attractive alternative is represented by the electrochemical generation of H_2 directly from seawater, about which, however, a mature scientific literature background is still missing. Furthermore, in the unpurified seawater there are hundreds of different impurities which might lead to catalyst poisoning, especially with platinum-based catalysts. That is why the catalysts prepared for the "traditional" HER could not be adopted for seawater electrolysis. Therefore, throughout the second year of the following PhD project, efforts have been devoted to design two new and stabler, more active and robust nano-structured catalysts for HER in seawater, such as a trimetallic alloy (NiRuIr_G) and a quaternary nanostructure (RuOs_G), both supported on graphene and exhibiting high stability in the new electrolytic environment. Once again, they were synthesized through a wet-chemistry, easily reproducible and scalable synthesis approach, and after being broadly characterized, they were tested in an electrolytic cell with seawater, showing remarkable performance when compared to literature and Pt itself. Eventually, during the third year, a further step forward towards sustainability has been undertaken, based on the following rationale: combining water and renewable sources to produce clean and pure hydrogen in a green perspective is appealing, but it would be even more fascinating if also a detrimental greenhouse gas, such as carbon dioxide (CO_2), could be employed in the same process along with the same reactant with the double purpose of reducing the carbon footprint and obtaining a valuable chemical, such as a "greener" syngas, with a tunable CO/H_2 ratio, enabling the integration of a sustainable process into production lines of different chemicals. From an accurate search and evaluation of the available scientific literature on the most efficient catalysts thus far proposed for the simultaneous HER and carbon dioxide reduction reaction to carbon monoxide (CO_2RR to CO), it emerged that catalytic activity and stability can be significantly increased by turning from metal-based nano-sized catalysts to metal single atom catalysts (SACs) in the M-N-C form. However, literature on this cutting-edge topic is still limited and there are still many routes to explore such as, for instance, better regulating the H_2 and CO production by preparing two metals on the same carbonaceous support with dual N-M active sites. Following this idea, throughout the last period of PhD research, a novel dual-active sites single atom catalyst for the syngas electro-production has been prepared through a simple pyrolysis method, adopting nontoxic glucose as carbon precursor and very small quantities of two economic metals, i.e. zinc (Zn) and cobalt (Co). The as-prepared catalysts, named as ZnCo-NC, showed higher performance than most of the current catalysts reported in the literature.

Introduction

In the modern technological society, the continuous rise of the worldwide energy demand, caused by the world population growth and the global development, as well as the subsequent increase of the greenhouse gases emissions due to the enormous consumption of fossil-based feedstock have raised great concern regarding the need for environmentally clean and energy-efficient alternatives. According to the International Energy Agency, in 2021 worldwide energy-related carbon dioxide (CO_2) emissions are setting to reach their second-largest annual increase in history. Indeed, although the Covid-19 pandemic is still ongoing, demand for all fossil fuels has grown dramatically: for instance, coal demand for electricity generation is expected to increase by 60% over last-year value by the end of the year, i.e. more than the increment of all renewables combined. The expected boost would contrast the drop recorded in 2020 by almost 80% and the CO_2 emissions would be below the 2019 emissions level just by 1.2% (IEA, 2021). In this scenario, the need to move to renewable energy sources to overcome this critical issue is undeniable and undelayable.

Among renewables, molecular hydrogen gas (H_2) is one of the most promising energy carriers for the future. Although 95% of the global hydrogen, which can be rarely found in nature in its molecular form, is currently produced from fossil fuels, turning to the so-called "green hydrogen", whose colour indicates the sustainability of its production, is of such fundamental relevance for the development of a carbon-neutral economy that the recently approved European Union's Green Deal considers it as a fundamental goal to be achieved within 2050 (European Commission, 2020).

Water electrolysis, or electrochemical water splitting, is the process which enables the generation of H_2 at its highest level of purity and at the lowest temperatures when compared to all the other hydrogen generation processes, including room temperature. Moreover, in this process water is both the only starting molecule and by-product in a cycle where the H_2 combustion releases energy and generates again water at the same time. More specifically, water splitting is the conversion of electrical energy into

chemical energy through the development of redox reactions: at the anode, the oxidation of OH^- ions from water to form molecular oxygen (O_2), water (H_2O) and electrons (e^-); at the cathode, the reduction of hydrogen ions (H^+) by free electrons to form H_2, which is better known in the literature as hydrogen evolution reaction (HER) (Neagu et al., 2000).

Like any other endothermic chemical reactions, energy input in the form of electrical energy is required for the HER to occur, which could be considered as the main limitation of this synthesis method.

However, from the analysis of the most recent and reliable market forecasts, it becomes clear that water electrolysis technology is not doomed to be relegated from the hydrogen production industry. On the contrary, its market is expected to grow at the highest rate in the next few years because of (i) the increasing demand for fuel cells vehicles which, in order to be competitive, require low-cost and low-emission hydrogen production methods and (ii) the possibility of overcoming the main bottlenecks of both the electrolysis process and the renewable sources (which, for the latter ones, are mainly due to stationarity, intermittence and regionalism issues) by coupling them to each other (Allied Market Research, 2021).

Furthermore, since the energy, in the form of overpotential, required for the HER to occur is strictly influenced by the nature of the catalyst adopted at the electrode, the most crucial impulse to the development of water electrolysis can come from the design of novel, more cost-effective and more energy-efficient electrocatalysts.

The early industrial-scale technology adopts alkaline electrolyzers, whose main advantage is the fact they do not need expensive noble metals at the electrode. However, catalyst performance in alkaline electrolytic environment is worse due to the inefficient water dissociation step needful to initiate the first step of the HER.

On the other hand, when HER occurs in acid electrolytic environment, overpotentials are the lowest and catalytic performances are the highest.

Platinum (Pt)-based electrocatalysts and their derivatives are by no means the most efficient catalysts towards the hydrogen evolution in acid electrolyte solutions owing to their optimum atomic hydrogen adsorption energy and low H_2 binding energy to favor its desorption from the catalyst surface. They, indeed, exhibit an overpotential as close to thermodynamic potential as possible, very high current densities at low potentials, small Tafel slopes and high stability over time. However, their industrial-scale production and application have been significantly hindered by the scarce availability and high price of platinum. Hence, either reducing platinum loading or completely substituting it with earth-abundant and non-noble metals with high catalytic activity and durability is of fundamental relevance to further proceed towards a strong hydrogen economy (Zhu et al., 2019). In this scenario, Nanotechnology can be regarded as one of the key factors to consider for a significant development of the hydrogen electro-production

technology. This new discipline, which can be described as the modern evolution of 20th-century Chemistry, deals with the possibility of exploiting physical matter at a nanometer scale. Control of materials at this scale can lead to several advantages for catalytic applications, such as much higher contact areas at the interface between different phases as well as new and interesting properties, which do not belong to "bulk" matter, caused by the so-called quantum size effect. Through Nanotechnology, synthesizing nanostructures characterized with peculiar morphologies and audacious chemical couplings with enhanced electrochemical properties has recently become possible. Therefore, Nanotechnology represents a real opportunity to boost the production of hydrogen through electrolysis, allowing the design and synthesis of novel, more active, stabler and cheaper electrocatalysts. As can be inferred from simple research conducted on Scopus, the world-class Elsevier's abstract and citation database, the worldwide scientific literature on the hydrogen evolution reaction has skyrocketed within the last two decades, which corresponds exactly to the "prime" of the Nanotechnology era. To make an example, the number of scientific studies produced on the subject is so considerable that it amounts, nowadays, to about 1/10 of the number of studies produced on topics of enormous scientific relevance such as graphene and its application in all possible fields. After analyzing this large number of studies on the topic, it became evident that nano-structured platinum is indispensable in the formulation of efficient HER electro-catalysts, but also another important information emerged, which is that the platinum amount can be reduced in favor of other more available, more cost-effective which, combined with platinum, can lead, in virtue of synergistic effects, to much more efficient nanomaterials.

In view of all this, the primary objective of the following PhD research project has been to design new nano-structured catalysts for the HER with the purpose of: (i) increasing catalytic performance compared to current literature and, at the same time (ii) using a reduced amount of platinum and (iii) studying new combinations of small quantities of other metals with platinum, also adopting more economic and, at the same time, highly efficient supports. Considering the excellent stability and the top position in the Trasatti's volcano plot for HER of rhodium (Rh), as well as the remarkable electrochemical performance of molybdenum disulfide (MoS_2), which is attracting significant attention for its "graphene-like" nanosheet-based morphology and highly conductive properties, two nano-electrocatalysts were synthesized and named as PtRh and PtRh/MoS_2. They were obtained through a one-pot synthesis with a scalable and cost-effective bottom-up wet chemistry approach. Subsequently, the samples were extensively characterized and their electrocatalytic properties for HER were evaluated, proving to be excellent.

Throughout this study, carried out during the first year of the PhD course, another important issue emerged: adopting smaller quantities of efficient

electocatalysts at the electrode is not the only method to significantly improve the electrolysis process, but the preparation of the electrolytic solution must be considered as well. Indeed, distilled water adopted in the electrolytic cell is obtained only after a series of expensive and complex purification steps, followed by the addition of either acid or basic electrolytes, which obviously increase the total costs of the process (Pangarkar et al., 2014). Considering this, an interesting and attractive alternative is represented by the electrochemical generation of H_2 directly from seawater, about which a mature scientific literature background is still missing.

Nevertheless, about 97% of the water in nature originates from seas and oceans and therefore it is easily and freely available as seawater (S.A. Kalogirou et al., 2015). Rather than using solutions of electrolytes in distilled water, adopting directly these abundant saline water resources for electrolysis would be highly advantageous. Firstly, as also previously mentioned, by directly feeding seawater to an electrolyzer, the expensive and complex purification and desalination processes are not required anymore. Rather, salts contained in water (such as sodium chloride, which is mainly present) act themselves as charge carriers during electrolysis. Moreover, the high presence of these charge carriers in seawater means that there is no need of further addition of acid or basic electrolytes. Therefore, production costs are reduced compared to the ones of distilled water-based electrolysis and there are no costs related to the disposal of electrolytes and removed residual salts. On the other hand, the high presence of salts, which makes the conductivity of seawater higher compared to distilled water, determines a corrosive environment for the catalysts (Abdel-Aal et al., 2010). However, in the unpurified seawater, there are hundreds of different impurities which might lead to catalyst poisoning. Platinum, for instance, is one of the most susceptible catalysts to this kind of poisoning (Liu D. et al., 2017). That is why the catalysts prepared for the “traditional” HER could not be adopted for seawater electrolysis. Therefore, throughout the second year of the following PhD project, efforts have been devoted to design new, more economic, versatile and efficient nano-structured catalysts for HER in seawater, capable of ensuring not only higher performance, but also guaranteeing high tolerance towards impurities and good stability and resistance in corrosive environment compared to the ones recorded in the current literature. While the first year was dedicated to the study of bimetallic alloys, during the second year, focus has been placed on the study and synthesis of trimetallic alloys and quaternary compounds, which, due to positive synergistic effects, proved high performance in scientific literature. In particular, a nanomposite comprising osmium and ruthenium oxides, the corresponding metals and a graphene-based support (named as RuOs_G), and a trimetallic alloy based on iridium, ruthenium and nickel also supported on few-layer graphene (named as NiRuIr_G) were synthesized through a

wet-chemistry, easily reproducible and scalable synthesis approach. Afterward, they were broadly characterized and tested in an electrolytic cell with seawater, showing remarkable performance.

Eventually, at the end of the experimental campaign of the second year, a further step forward towards sustainability has been taken, based on the following rationale: combining water and renewable sources to produce clean and pure hydrogen in a green perspective is appealing, but would not be even more fascinating if also a detrimental greenhouse gas, such as carbon dioxide (CO_2), could be employed in the same process along with the same reactant with the double purpose of reducing the carbon footprint and obtaining a valuable chemical, such as syngas?

Indeed, since the last century, the global average atmospheric concentration of CO_2 has been dramatically increasing at an exponential rate, reaching, at present, over 414 ppm, which is about 50 % higher than the level at the beginning of the Industrial Revolution (Global Monitoring Laboratory- Earth System Research Laboratories, 2021). Among the emitted gases, CO_2 is one of the most dangerous, being the main responsible for the greenhouse effect and amounting to over 80% of the whole emissions (Dincer et al., 2015; Cortright et al., 2002; Weng et al., 2016; Raoof et al., 2010). At the same time, around 1.7×10^8 tons of syngas per year are produced worldwide mainly through steam methane reforming and coal gasification, with a global market that is expected to grow till 72.4 billion US dollars by 2022 at a compound annual growth rate of 9.1% (Jouny et al., 2018; BCC Publishing, 2018). Depending on its CO/H_2 ratio, a synthesis gas could be employed in several industrial processes, such as methanol synthesis, syngas fermentation and Fischer–Tropsch synthesis (Sheng et al., 2017; Ross et al., 2017). Although being cost-effective, it is worth noticing that current industrial processes for syngas generation are mostly fossil-fuels dependent, which means that they are not fully “optimized” from an environmental point of view. In this scenario, the co-electrolysis of carbon dioxide and water can lead to a syngas with a tunable CO/H_2 ratio, hence ensuring the integration of a sustainable process into production lines of different chemicals.

Prior to the experimental phase, to deepen the knowledge of the topic, an accurate search and evaluation of the available scientific literature on the most efficient catalysts thus far proposed for the electro-reduction of CO_2 and H_2O has been carried out. From this study, it emerged that catalytic activity and stability towards the carbon dioxide reduction reaction to CO (known in the literature as CO_2RR to CO) can be significantly increased by turning from metal-based nano-sized catalysts to metal single atom catalysts (SACs). Indeed, due to the reduced coordination environment, SACs are much more reactive with fewer limitations to diffusion phenomena and without the presence of inactive sites, which are typical of heterogeneous catalysis. Furthermore, small percentages of more economic and available

metals can be adopted in their formulation, since in their atomic form, some metals, which in their nano-size form were selective towards HER, can shift their selectivity from H_2 to CO.

Among them, metal single atoms in the form of M-N-C catalysts (with M: metal single atom; N: nitrogen atom; C: carbonaceous support) can achieve high performance since the structure of their active centers, typically formed by a single metallic atom coordinated with several nitrogen atoms on a carbon support, is particularly suitable for favoring the adsorption of the CO_2 molecule and its intermediates over the adsorption of H^+ ions, depending on the adopted metal. Indeed, the choice of an appropriate metallic element in its atomic form is crucial not only to the activity but also to the selectivity of the process, since CO_2 can be reduced to other chemicals besides CO, and HER must occur at the same time, with a hydrogen production rate in line with the desired CO/H_2 ratio. N atoms can contribute to increase the activity and stability of the metal single atoms by reciprocal coordination to form peculiar active centers and by avoiding their agglomeration in nanoclusters or nanoparticles. On the other hand, the contribution to the whole activity and stability given by highly electronic conductive and porous carbonaceous supports such as graphene-, carbon nanotubes- and other carbon precursors- (pyrrole, dicyandiamide, glucose etc.) derived supports is undeniable (Varela et al., 2019). However, literature on this cutting-edge topic is still limited and mainly focusing on monometallic SACs for CO production. Indeed, there are still many routes to explore in view of further increasing activity and stability of these catalysts as well as of better regulating their selectivity towards CO for their industrial-scale application to the production of a syngas with a wider CO/H_2 ratio, such as, for instance, regulating the H_2 and CO production by preparing two types of metallic atomic active centers on the same carbonaceous support. Following this idea, throughout the last period of PhD research, a novel dual-active sites single atom catalyst for the syngas electro-production has been prepared through a simple pyrolysis method, adopting nontoxic glucose as carbon precursor and very small quantities of two economic metals, i.e. zinc (Zn) and cobalt (Co). The as-prepared catalysts, named as ZnCo-NC, showed high performance towards the simultaneous production of CO and H_2.

Based on what written so far, the following thesis will be structured into several chapters, with each of them focused on one of the above-mentioned topics. The first chapter will be focused on the catalysis of the hydrogen evolution reaction in acid medium and on the results obtained with the prepared PtRh and $PtRh/MoS_2$ catalysts. The second chapter will deal with the catalysis of the same reaction in seawater, showing the results obtained with the novel RuOs_G and NiRuIr_G catalysts. The third chapter will report an in-depth study on the available scientific literature on the most efficient catalysts thus far proposed for the electro-reduction of CO_2 to CO

and of CO_2 and H_2O to syngas. The fourth chapter will, eventually, report the results obtained with the synthesized bimetallic ZnCo-NC catalyst for the catalysis of the syngas electro-generation. Conclusions, including future perspectives of research, will eventually be proposed.

Chapter 1:
New nano-structured catalysts for the hydrogen evolution reaction (HER)

1.1 Nano-structured catalysts for the hydrogen evolution reaction (HER): State of the Art

Electro-production of hydrogen through water splitting is one of the most promising technologies for the future not only because it enables the production of high-purity hydrogen at ambient conditions and in a sustainable way, but also because, in the view of adopting renewables as energy input, through this technology is possible to store intermittent, stationary and regional energy sources in the form of chemical compounds, which means overcoming the main limitations of renewable energies. Furthermore, in order to generate syngas from the electro-chemical reduction of carbon dioxide in an aqueous solution, it is essential not only to be able to favor the selectivity towards CO, but also to control the activity and the kinetic of the hydrogen evolution reaction so that to be able to efficiently tune the H_2/CO ratio. Therefore, in this first chapter focus will be placed on the study of the catalysis of the HER at the cathode of an electrolytic cell at ambient temperature and pressure (Neagu et al., 2000; Allied Market Research, 2021).

As mentioned in the introduction, pure platinum has been thoroughly studied for its outstanding electrocatalytic performance towards HER, especially in acidic media. Nevertheless, its industrial-scale production and application have been significantly hampered by its scarce availability and high price. In the last few decades, several elements (such as Cu, Pd, Fe, Mo, Ni, Ru, Co, etc.) (Pentland et al., 1957; Badawy et al., 2013; Tran et al.,

2016; S. Cobo et al., 2012) have been investigated with the aim of finding high-performance, yet more cost-effective and earth-abundant substitutes for Pt as efficient HER nano-structured catalysts. For instance, the HER can efficiently occur in an aqueous buffer solution with neutral pH by using the cobalt-oxo/hydroxo-phosphate catalyst developed by Cobo et al. (2012). Other research studies focused on the use of no-platinum-based metal alloys in alkaline solutions, such as CoMo (Spasojevic et al., 1984), FeMo (Elezovic et al., 2005), Ni–P reinforced with co-deposited graphite (Shervedani et al., 2008), NiFeMo or NiMo (Arul Raj et al., 1990), which showed both good corrosion resistance, hence significant durability and high HER activity in virtue of synergistic effects between metals. For instance, Arul Raj et al. (1990) proposed the synthesis of NiFeMo- and NiMo-based catalysts which guaranteed an overpotential of −0.187 V over 1500 hours of continuous electrolysis in a 6 M KOH solution under typical industrial conditions. However, in alkaline solutions, as mentioned above, HER performance is not very remarkable and water electrolysis was necessarily conducted at 353 K to reach those values. With the aim of gaining a broader insight into the topic, KMcCrory et al. (2015) have recently compared the performance of 18 HER electro-catalysts in both acidic (1 M H_2SO_4) and basic conditions (1 M NaOH). As shown in Figure 1 and 2, they tested several metal-based HER catalysts and evaluated their overpotential at −10 mA/cm^2 under different pH conditions. From this study, it is clear, however, that despite the good results obtained with the usage of some non-noble metals, especially of the NiMo and NiMoCo electrocatalysts (which, although exhibiting even lower overpotentials than Pt, show a very short-time resistance in corrosive acidic environments) the importance of the presence of Pt and other noble metals in the catalyst formulation for the overall activity and stability, as well as the necessity of adopting acid electrolyte solutions in the cell, is undeniable to achieve superior performance towards HER.

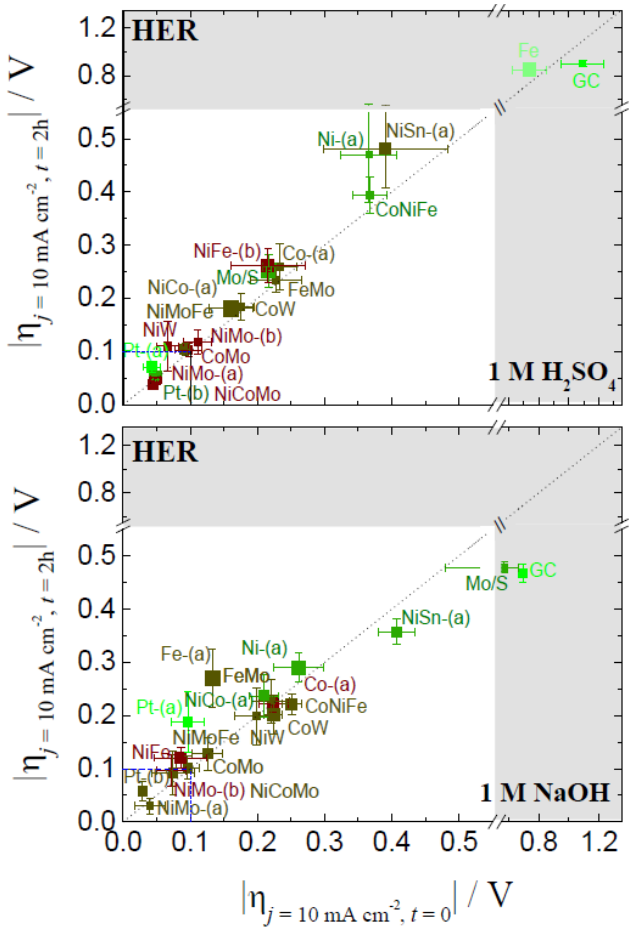

Figure 1. *Plots describing the catalytic activity and stability for HER of some electrocatalysts in acidic (top) and alkaline (bottom) solutions. On the x-axis and y-axis, the overpotential required to achieve a current density of 10 mA/cm^2 at time t = 0 and time = 2 hours is reported respectively. The diagonal dashed line is the expected response for a stable catalyst which does maintain its activity unchanged after 2 hours of constant polarization. Reprinted with permission from (McCrory C. C. L., S. Jung, I. M. Ferrer, S. M. Chatman, J. C. Peters and T. F. Jaramillo (2015) Benchmarking Hydrogen Evolving Reaction and Oxygen Evolving Reaction Electrocatalysts for Solar Water Splitting Devices. J. Am. Chem. Soc., **137**, 4347–4357). Copyright (2021) American Chemical Society*

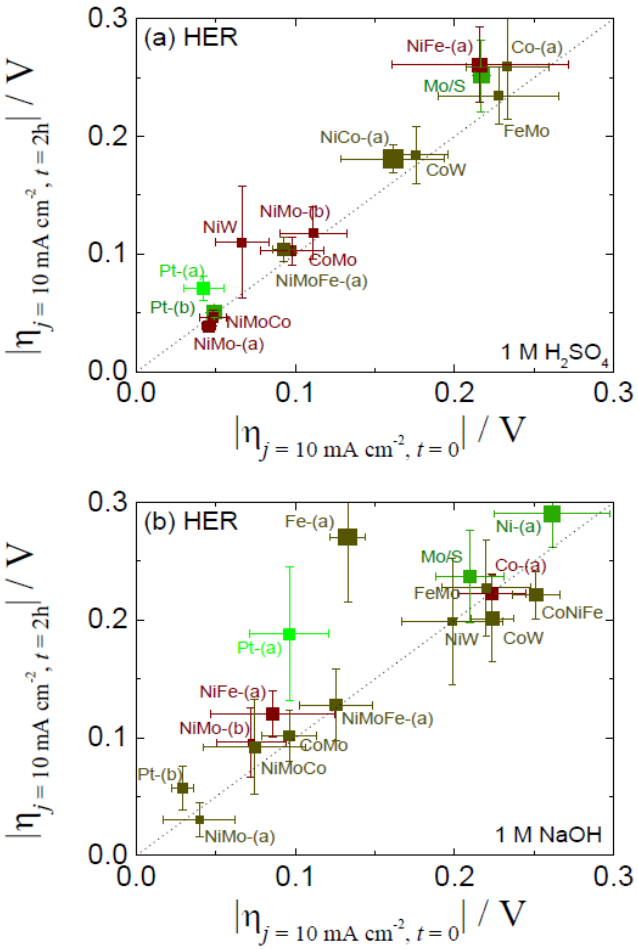

Figure 2. *Zoomed plots of the ones reported in Figure 1. Plots describing the catalytic activity and stability for HER of some electrocatalysts in acidic (top) and alkaline (bottom) solutions. On the x-axis and y-axis, the overpotential required to achieve a current density of 10 mA/cm^2 at time t = 0 and time = 2 hours is reported respectively. The diagonal dashed line is the expected response for a stable catalyst which does maintain its activity unchanged after 2 hours of constant polarization. Reprinted with permission from (McCrory C. C. L., S. Jung, I. M. Ferrer, S. M. Chatman, J. C. Peters and T. F. Jaramillo (2015) Benchmarking Hydrogen Evolving Reaction and Oxygen Evolving Reaction Electrocatalysts for Solar Water Splitting Devices. J. Am. Chem. Soc., **137**, 4347–4357). Copyright (2021) American Chemical Society*

The previously mentioned overpotential η of an electrochemical reaction is defined as the difference between the recorded reduction potential and the thermodynamic reduction potential of the reaction. The main causes for the overpotential are: (a) the high energy needed to activate the reaction, especially for the occurrence of reaction rate-limiting steps; (b) mass transport resistances; and (c) ohmic losses due to the electrolyte and the electrode conductivity. To evaluate the HER performance of a catalyst, another important parameter, apart from the overpotential, is the Tafel slope. The Tafel slope, i.e. the slope of the linearized portion of the Tafel plot, indicates the limiting step of the HER mechanism, therefore giving information about the reaction rate.

1.2 Design of novel PtRh and PtRh/MoS_2 nano-electrocatalysts for the hydrogen evolution reaction

1.2.1 Introduction: reasons behind the choice of the catalysts

In the second part of this first chapter, the catalysis of the hydrogen evolution reaction in acid electrolytes will be studied on novel Pt-based nano-structured catalysts. As mentioned above, in order to improve the electrocatalytic performance of Pt and minimize its usage, Pt-based bimetallic nanostructures have attracted increasing interest during the past decade as the best alternative to pure Pt for HER in virtue of a synergistic effects between metals which can lead to comparable or, sometimes, even better performance than the one of pure Pt (Weng et al., 2016; Raoof et al., 2010). For instance, Domínguez-Crespo et al. (2012) proposed the synthesis of bimetallic Ni_xPt (X=1,2,3) nanoparticles through hydrogenation of $Ni(cod)_2$ ad $Pt_2(dba)_3$ in presence of a hexadecylamine ligand. Electrochemical tests in a 0.5 M H_2SO_4 solution (see Figure 3) showed that Ni_2Pt records a lower overpotential and higher current density than pure Ni in virtue of a synergistic effect due to the addition of platinum, which, in that specific proportion, may guarantee a better dispersion of the metals in the nanostructure and therefore higher electrochemical surface area (ECSA).

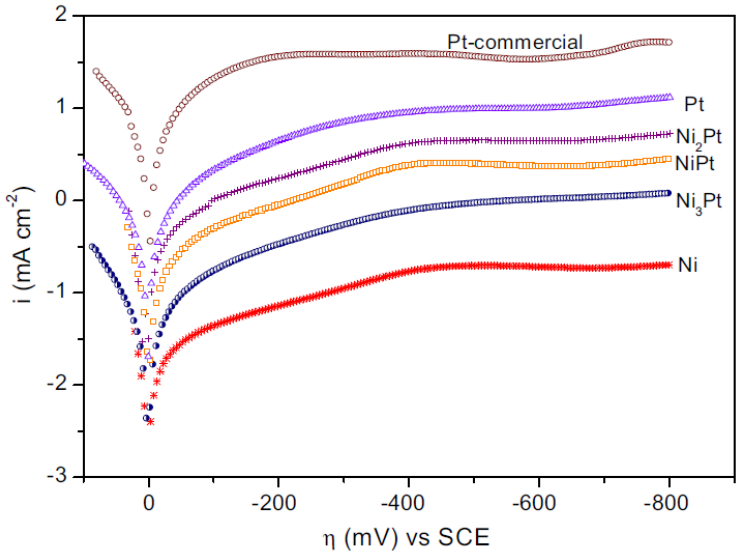

Figure 3. *Polarization curves for the HER on the nano-structured Ni_xPt electrodes, Pt, commercial-Pt and Ni in 0.5 M H_2SO_4 solution. Reprinted with permission from (Domínguez-Crespo M. A., E. Ramírez-Meneses, A. M. Torres-Huerta, V. Garibay-Febles and K. Philippot (2012) Kinetics of hydrogen evolution reaction on stabilized Ni, Pt and Ni–Pt nanoparticles obtained by an organometallic approach. Int. J. Hydrog. Energy, **37**, 4798-4811). Copyright (2021) Elsevier*

Weng et al. (2016) prepared AuPt nanodendrites obtained by a single-step seedless aqueous approach involving 5-Aminouracil-6-carboxylic acid as capping agent and weak stabilizer. In virtue of a synergy between the metals, the synthesized catalyst exhibits in a 0.5 M H_2SO_4 solution a very low Tafel slope of 34 mV/dec and an overpotential of around 0.01 V *vs.RHE*, which are values even lower than the ones of Pt nanospheres (Pt NSs) and comparable with the ones of commercial Pt on carbon (Pt/C), as shown in Figure 4.

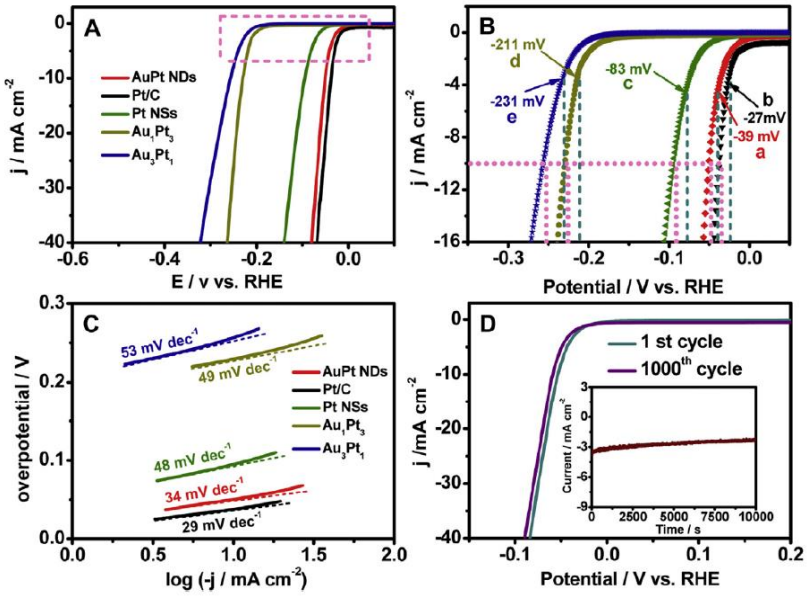

Figure 4. *(A,B) Linear sweep voltammetry (LSV) curves of AuPt NDs, commercial Pt/C, Pt NSs, Au_1Pt_3, Au_3Pt_1 (these latter two ones are nanocrystals in different metal proportions) catalysts in 0.5 M H_2SO_4 at a scan rate of 5 mV/sec. (B) and (C) The corresponding Tafel slopes and the corresponding Tafel plot. (D) HER activities of AuPt NDs before and after 1000 cycles at a scan rate of 50 mV/sec. The inset reports the chronoamperometric curve of AuPt NDs for 10000 s at 0.30 V. Reprinted with permission from (Weng X., Y. Liu, K. K. Wang, J. J. Feng, J. Yuan, A. J. Wang and Q. Q. Xu (2016) Single-step aqueous synthesis of AuPt alloy nanodendrites with superior electrocatalytic activity for oxygen reduction and hydrogen evolution reaction. Int. J. Hydrog. Energy, **41**, 18193-18202). Copyright (2021) Elsevier*

Qing et al. (2015) synthesized fully ordered face-centered tetragonal (fct) FePt nanoparticles (NPs) through thermal annealing of MgO-coated dumbbell-like FePt-Fe_3O_4 nanoparticles, followed by acid leaching to remove MgO. Unlike platinum, which despite being the top catalysts for HER in acid medium is very susceptible to acid etching after a long-time activity, the fully ordered fct structure of the synthesized FePt nanoparticles shows very robust chemical stability against Fe etching in acid solutions. That is why, apart from a HER activity almost comparable with the one of pure platinum due to a synergy between metals, the fct-FePt NPs structure is responsible for superior durability when compared with the one of pure Pt. Indeed, while for the Pt catalyst a potential shift of around 0.007 V at 10 mA/cm^2 is recorded after 10000 cycles of test, for the fct-FePt NPs, the two

HER polarization curves before and after the cycling test almost overlap (see Figure 5).

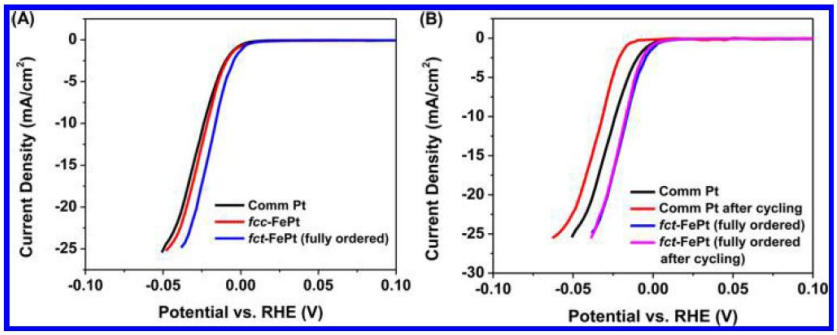

Figure 5. *(A) HER polarization curves for commercial Pt/C, fcc-FePt and fully ordered fct-FePt. (B) HER activity of the commercial Pt/C and fully ordered fct-FePt/C before and after 10000 cycles of test. Polarization curves were recorded in a 0.5M H_2SO_4 solution. Reprinted with permission from (Li, Q., L. Wu, G W., D. Su, H. Lv, S. Zhang, W. Zhu, A. Casimir, H. Zhu, A. Mendoza-Garcia, and S. Sun (2015) New Approach to Fully Ordered fct-FePt Nanoparticles for Much Enhanced Electrocatalysis in Acid. Nano Lett., **15**, 2468-2473). Copyright (2021) American Chemical Society*

Raoof et al. (2010) prepared Cu and Pt nanoparticles deposited on a poly(8-hydroxyquinoline)-modified glassy carbon electrode (p(8-HQ)/MGCE) through galvanic replacement. As can be noticed from the polarization curves in Figure 6, adding Pt NPs to Cu nanoparticles increases significantly the HER electrocatalytic activity, in virtue of the above-mentioned synergistic effect in bimetallic catalysts. On the Cu/Pt–p(8-HQ)MGCE surface, the reaction starts at about 0.23 V *vs.SCE*, as indicated by a steep increase in the cathodic current, even steeper than the current density evolution recorded on the bare Pt electrode.

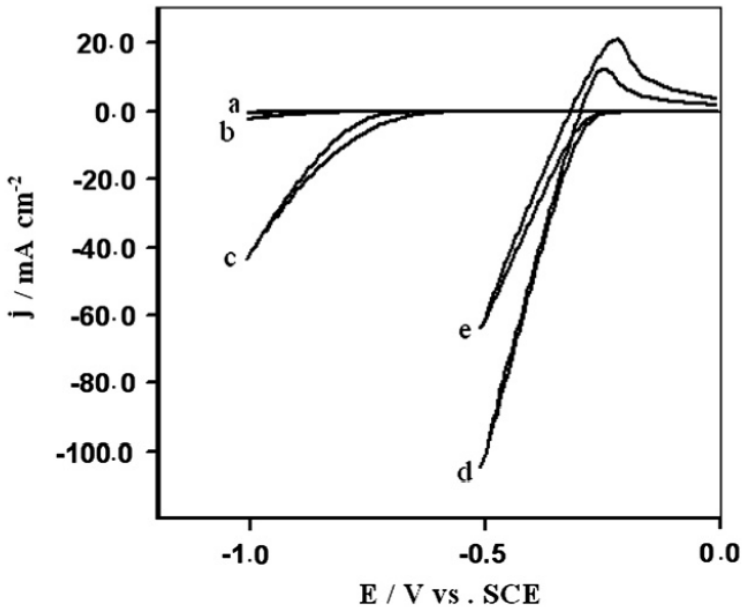

Figure 6. *Cyclic voltammograms of bare GCE (a), p(8-HQ)MGCE (b), Cu–p(8-HQ)MGCE (c), Cu/Pt–p(8-HQ)MGCE (d) and bare Pt electrode (e), in a 0.1 M H_2SO_4 solution at 50 mV/sec. Reprinted with permission from (Raoof J. B., R. Ojani, S. A. Esfeden and S. R. Nadimi (2010) Fabrication of bimetallic Cu/Pt nanoparticles modified glassy carbon electrode and its catalytic activity toward hydrogen evolution reaction. Int. J. Hydrog. Energy, **35**, 3937-3944). Copyright (2021) Elsevier*

Zhang et al. (2019) proposed a simple one-pot method for the synthesis of uniform bimetallic PtCo alloyed nanodendrites in oleylamine assisted by the usage of L-proline and cetyltrimethylammonium chloride. Polarization curves show that the overpotential of the synthesized material ($Pt_{75}Co_{25}$ NDAs) is equal to -11.3 mV, which is not only lower than Pt black (-23.3 mV) but also better than the ones of $Pt_{60}Co_{40}$ NPs (-15.3 mV), $Pt_{82}Co_{18}$ NPs (-16.3 mV), i.e. nanoparticles of the same elements with different proportions. What is more, the Tafel slope of the catalyst is of 30 mV/dec, which is the smallest compared to the ones of 47, 42 and 43 mV/dec (related to Pt black, $Pt_{60}Co_{40}$ NPs and $Pt_{82}Co_{18}$ NPs respectively) under the same conditions, which indicates the better HER reaction kinetic of the nanodendritic-shaped bimetallic alloy. These results (see Figure 7A and 7B), along with the proved long-term stability of the catalyst (see Figure 7C and 7D), not only allowed to realize the importance of the choice of the second element in the Pt-based alloy, but also of the control of the morphology of the nano-structured catalyst, as well as of the effects of different metals ratios in the alloy. In this particular study, the peculiar porous structure, the

high surface area and the small size of each dendrite became fundamental in determining the higher performance of the catalyst, along with the synergy between the metals in the alloy.

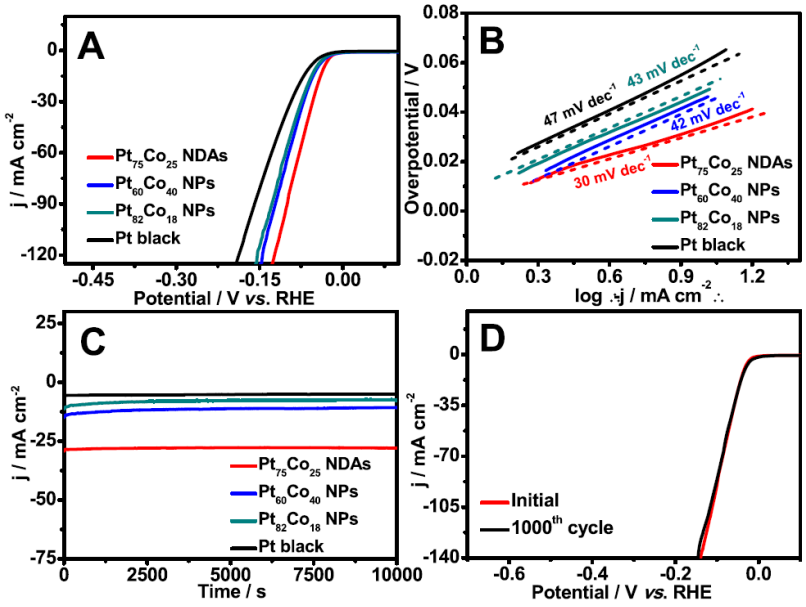

Figure 7. *Polarization curves (A) of the $Pt_{75}Co_{25}$ NDAs, $Pt_{60}Co_{40}$ NPs, $Pt_{82}Co_{18}$ NPs and Pt black catalysts at 5mV/sec in a nitrogen-saturated 0.5M H_2SO_4; (B) the corresponding Tafel plots ;(C) the chronoamperometric curves at -0.07 V vs.RHE; and (D) the polarization curves of $Pt_{75}Co_{25}$ NDAs before and after 1000 cycles under the same conditions of the one in (A). Reprinted with permission from (Zhang X. F., H. B. Meng, H. Y. Chen, J. J. Feng, K. M. Fang, and A. J. Wang (2019) Bimetallic PtCo alloyed nanodendritic assemblies as an advanced efficient and robust electrocatalyst for highly efficient hydrogen evolution and oxygen reduction. J. Alloys Compd., **786,** 232-239). Copyright (2021) Elsevier*

Another example of the effect of the morphology of the bimetallic nano-catalyst is proposed by Lim et al. (2019), who synthesized uniform popcorn-shaped $GaPt_3$ nanoparticles through a hot-solvent method in the presence of a mixture of oleylamine and hexamethyldisilazane under argon atmosphere at 280 °C. In virtue of the unique morphology and of the synergistic effect between metals, the as-prepared catalyst exhibits an overpotential lower than 0.08 V, a Tafel slope of 43.3 mV/dec, values comparable and even slightly better with than the ones of commercial Pt black and 20% Pt/C, as well as high stability over time (see Figure 8a, b and c).

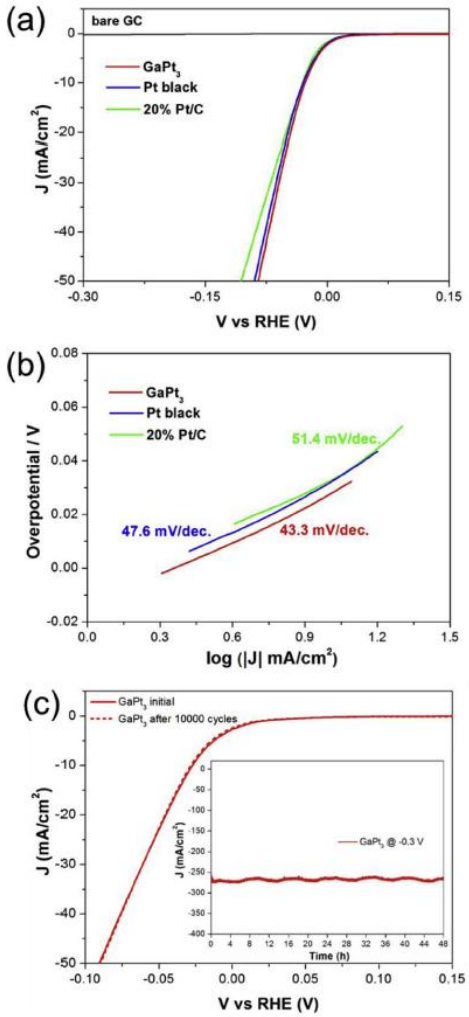

Figure 8. *Polarization curves for HER of $GaPt_3$, commercial Pt black and 20% Pt/C catalysts in a 0.5M H_2SO_4 solution at 5 mV/sec.(b)The corresponding Tafel slopes. (c) Polarization curves on $GaPt_3$ nanoparticles before and after 10000 cycles. In the inset, chronoamperometry result for $GaPt_3$ at a potential of 0.3V vs.RHE over 48 hours.Reprinted with permission from (Lim, S. C., C. Y. Chan, K. T. Chen, K and H. Y. Tuan (2019) Synthesis of popcorn-shaped gallium-platinum ($GaPt_3$) nanoparticles as highly efficient and stable electrocatalysts for hydrogen evolution reaction. Electrochim. Acta, **297**, 288-296). Copyright (2021) Elsevier*

In order to gain a deeper insight on the previously mentioned synergistic effects between metals, fundamental is the study carried out by Ojani et al. (2013), who prepared and characterized bicomponent PdPt microstructures

deposited on a copper electrode for catalysis of HER in acidic media. As can be seen in Figure 9, the polarization curve related to the Pd/Pt catalyst is steeper than pure Pt and the overpotential of the former catalyst at a current density of -0.13 A/cm^2 is around 45 mV lower than the one of pure Pt, proving the higher HER performance of the bimetallic catalyst.

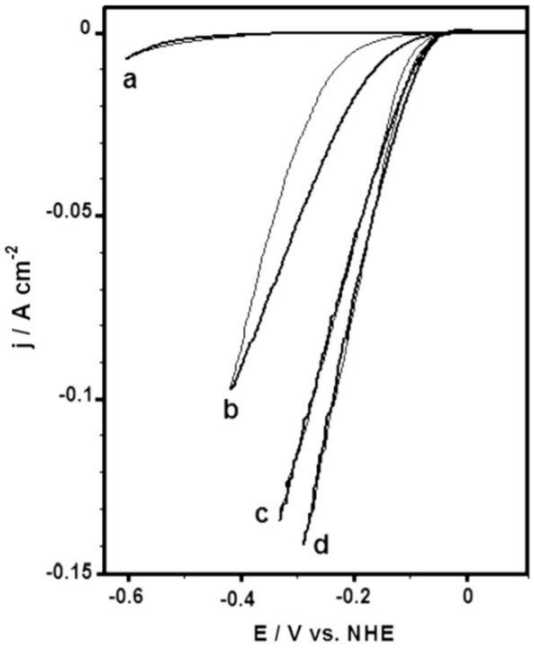

Figure 9. *Cyclic voltammograms of (a) Cu electrode (b) pure Pd (c)pure Pt and (d) PdPt microstructures modified in a 0.5 M H_2SO_4 solution at scan rate 5 mV/sec. Reprinted with permission from (Ojani R., J. B. Raoof and E. Hasheminejad (2013) One-step electroless deposition of Pd/Pt bimetallic microstructures by galvanic replacement on copper substrate and investigation of its performance for the hydrogen evolution reaction. Int. J. Hydrog. Energy, **38**, 92-99). Copyright (2021) Elsevier*

The authors clearly explained the improved HER performances of the PtPd catalyst as a result of a synergistic effect occurring between the two metals. A key to further understanding this phenomenon is provided by the "d-band center theory". According to this theory, the surface metal d-band is involved in the chemical bond with the adsorbate and the position of the d-band center compared to the Fermi level plays a governing role in determining the strength of the metal-adsorbate interaction. Alloying a metal M1 with another metal M2 modifies the surface bond lengths M1-M1 as a consequence of the introduction in the M1 lattice of M2 atoms with a different lattice constant (strain effect) and, at the same time, the presence of

M2 around metal M1 atoms changes its electronic environment (ligand effect). Both phenomena contribute to modify the d-band width of M1, therefore causing a shift of the d-band center which results in either a strengthening or a weakening of the M1-absorbate bond (Kitchin et al., 2004). Moreover, a bifunctional mechanism, i.e. faster water activation onto the surface of one of the metals, can also contribute to improve the catalyst performance (Ruban et al., 1997). It is clear, therefore, that nanostructures comprising Pt and a noble metal alloy can achieve enhanced HER performance.

Among noble metals, rhodium can be regarded as an excellent material, being at the top of Trasatti's volcano plot (Quaino et al., 2014). Furthermore, the presence of Rh, whose radius and electronegativity are higher than platinum, into the Pt lattice is expected to up-shift the d-band center of Pt, hence further increasing its affinity for H^+ adsorption and cathodic evolution (Van Santen et al., 1990).

PtRh as a nanocatalysts for HER has been little explored till now. This may be due to the fact that rhodium price has been very changeable over the last years. For instance, in 2003 its value was about $500/oz, but an increase in demand caused a sharp rise in price until 2008, when it almost reached $10,000/oz, whilst a new decrease was registered after that episode (Bloomberg, 2017). Nowadays, rhodium price is strictly connected to the automobile market, since more than 80% of the whole world supply is requested by the automotive catalyst industry. In fact, rhodium is fundamental in catalytic converters for both gasoline and, especially, diesel engines. Although the world rhodium market is still solid as a consequence of the still high demand of the noble metal by automobile industries, in the long run the rise of hybrid and electric vehicles is expected to heavily impact that market, causing, therefore, rhodium price to plummet, which will make this metal more affordable than platinum (ICA, 2017).

Moreover, considerable attention has been currently focused on 2D nanomaterials such as molybdenum disulfide (MoS_2), which has been found to be a highly efficient catalyst for HER due to its characteristic graphene-like two-dimensional structure (Yang L. et al., 2017; Huang et al., 2013). One of the main challenges regarding the usage of this material for the HER catalysis is that usually, for thermodynamic stability reasons, MoS_2 exposes its basal planes rather than its edges which would be, instead, more catalytically active towards HER.

As Kibsgaard et al. (2012) proved, by controlling the morphology of molybdenum disulfide at the nanoscale, it is possible to expose a large fraction of catalytically active edge sites, which are fundamental for the catalysis of the hydrogen evolution reaction. Based on this assumption, the authors managed to synthesize nano-structured MoS_2 with (i) a high surface curvature, which exposes a higher fraction of edge sites and (ii), to increase

diffusivity, and extended 3D mesoporous network structure. The resulting double-gyroid morphology (named as DG MoS_2) is schematically represented in Figure 10.

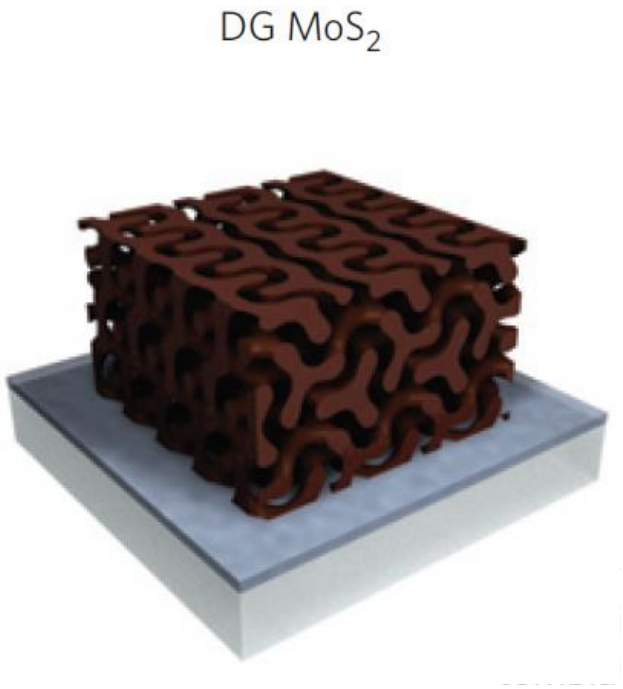

Figure 10. *Scheme of the double-gyroid morphology of the synthesized MoS_2. Reprinted with permission from (Kibsgaard, J., Z. Chen, B. N. Reinecke and T. F. Jaramillo (2012) Engineering the surface structure of MoS_2 to preferentially expose active edge sites for electrocatalysis. Nat. Mater., **11**, 963-969). Copyright (2021) Springer Nature*

These structure and morphology led to remarkable HER performance: a recorded Tafel slope of 50 mV/dec and, as can be seen in Figure 11, where the cyclic voltammetry data of the synthesized sample at three different Mo deposition time are reported, quite low overpotentials in the range of 150-200 mV.

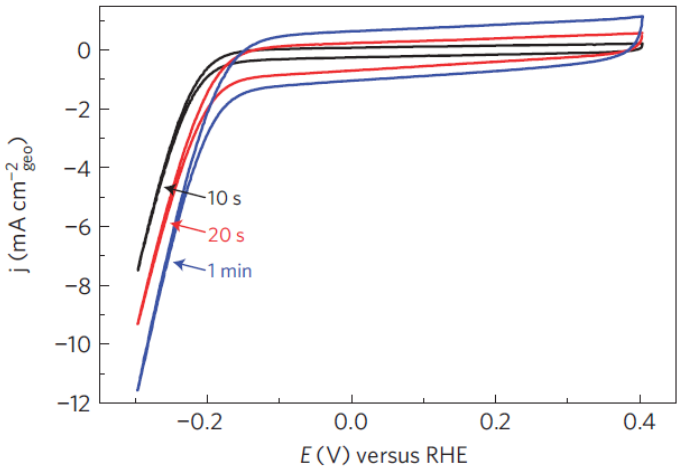

Figure 11. *Cyclic voltammograms of 10 s, 20 s and 1 min MoS_2 catalyst at 50mV/sec. Reprinted with permission from (Kibsgaard, J., Z. Chen, B. N. Reinecke and T. F. Jaramillo (2012) Engineering the surface structure of MoS_2 to preferentially expose active edge sites for electrocatalysis. Nat. Mater., **11**, 963-969). Copyright (2021) Springer Nature*

Similarly, Kong et al. (2013) prepared MoS_2 thin films through a kinetically controlled rapid sulfurization process, which enables the generation of vertically aligned layers with respect to the film. This morphology could guarantee a better exposure of the active edges on its surface, as schematized in Figure 12.

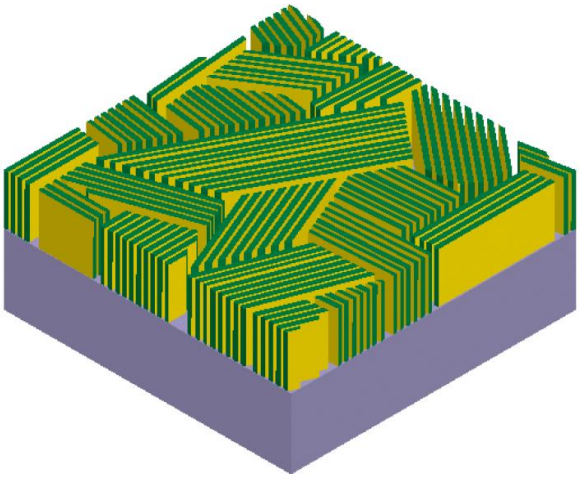

Figure 12. *Scheme of the structure of edge-terminated MoS_2 films with their layers aligned perpendicularly to the substrate, hence maximizing the exposure of the catalytically active edges. Reprinted with permission from (Kong, D., H. Wang, J. J. Cha, M. Pasta, K. J. Koski, J. Yao and Y. Cui (2013) Synthesis of MoS_2 and $MoSe_2$ films with vertically aligned layers. Nano Lett., **13**, 1341-1347). Copyright (2021) American Chemical Society*

As can be inferred from the polarization curves measured in a 0.5 H_2SO_4 solution (see Figure 13), the exchange current density of the catalyst is $2.2 \cdot 10^{-6}$ A/cm^2, i.e. a value 10 times higher than the one recorded for MoS_2 nanoparticles, even though Tafel slope is still high, being in the range of 105–120 mV/dec, which suggests that combining MoS_2 with other active phases could lead to even better performance.

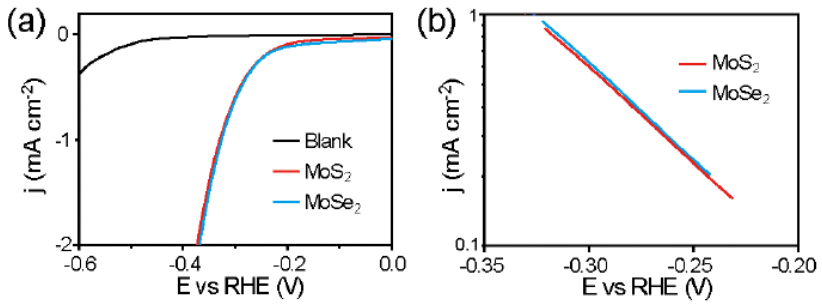

Figure 13. *(a) HER polarization curves of edge-terminated MoS_2 and $MoSe_2$ films and blank glassy carbon for comparison. (b) Corresponding Tafel plot for the three materials. Reprinted with permission from (Kong, D., H. Wang, J. J. Cha, M. Pasta, K. J. Koski, J. Yao and Y. Cui (2013) Synthesis of MoS_2 and $MoSe_2$ films with vertically aligned layers. Nano Lett., **13**, 1341-1347). Copyright (2021) American Chemical Society*

It is also clear, therefore, that morphology of the MoS_2 support can also contribute significantly to the total catalytic activity towards HER.

Based on these considerations, for the first time and by means of a scalable, economic, wet-chemistry approach, the synthesis of PtRh and PtRh covered with MoS_2 nano-electrocatalysts has been proposed. After being synthesized, the catalysts were characterized and tested towards HER, showing outstanding electrocatalytic performances and remarkable stability over time, likely due to the presence of a MoS_2 coating around the metals.

1.2.2 Materials and methods

1.2.2.1 PtRh nanostructures and Pt nanoparticles preparation

PtRh nanostructures, in the following named as PtRh, were obtained in 1-octadecene using 1-2 hexadecanediol as reducing agent and oleylamine and oleic acid as surfactants (Chen et al., 2004; Chen et al., 2006; Liu et al., 2009) by thermal decomposition of platinum(II) acetylacetonate and rhodium(III) nitrate hydrate under nitrogen flow. In particular, 0.61659 mmol of $Pt(C_5H_7O_2)_2$ and 0.43265 mmol of $Rh(NO_3)_3H_2O$ were mixed with 20 mL of 1-octadecene, 10 mmol of 1,2-hexadecanediol, 6 mmol of oleylamine and 6 mmol of oleic acid. Oleylamine was not only used as surfactant but also as stabilizer and mild reducing agent, being able to donate electrons at high temperatures (Mourdikoudis et al., 2013). Regarding the PtRh synthesis, the mixture was heated to 200 °C for 120 min and then further heated to reflux (~300 °C) for 60 min. Moreover, for comparison, Pt

nanoparticles, in the following named as Pt NPs, were prepared with the same procedure by using only platinum(II) acetylacetonate as precursor material.

1.2.2.2 PtRh-MoS_2 nanostructures preparation

PtRh-MoS_2 nanostructures, in the following named as PtRh-MoS_2, were prepared using the same method of the previously described samples. In detail, in order to perform this synthesis, the following chemicals were used: platinum(II) acetylacetonate (0.61659 mmol), rhodium(III) nitrate hydrate (0.43265 mmol), ammonium tetrathiomolybdate (0.57613 mmol), 1-octadecene (20 mL), 1,2-hexadecanediol (10 mmol), oleic acid (6 mmol) and oleylamine (6 mmol).

1.2.2.3 PtRh, Pt NPs and PtRh-MoS_2 post synthesis treatments

The organic chains covering the synthesized samples have the double function of stabilizing and preventing nanostructures aggregation, but, at the same time, exhibit a resistive behavior. Therefore, in order to reduce the number of chains, the PtRh, Pt and PtRh-MoS_2 nanostructures underwent a thermal treatment under air flow, from room temperature up to 150 °C at 10 K/min for 8 hours, which allowed the reduction of about 70 wt% of the number of organic chains (Sarno et al., 2016).

1.2.2.4 Methods

Several techniques have been adopted in order to characterize the synthesized samples. Transmission electron microscopy (TEM) was performed with a FEI Tecnai electron microscope operated at 200 KV with a LaB_6 filament as an electron source, while field emission scanning electron microscopy (FESEM) images were obtained by the use of a LEO 1525 electron microscope. Both the microscopes were equipped with an energy dispersive X-ray (EDX) probe. A Bruker D8 X-ray diffractometer with a monochromatic CuKα radiation was used for measurements of powder diffraction profiles.

By adopting an Autolab PGSTAT302N potentiostat, the electrochemical performance towards HER was evaluated by linear sweep voltammetry tests in a 1M H_2SO_4 solution.

Before the electrochemical measurements, 8 mg of synthesized sample were dispersed into 160 µl of a 5 wt% Nafion solution, 900 µl of 2-propanol and 100 µL of water to prepare a homogeneous suspension which, after a sonication treatment for 30 minutes and subsequent air-drying, was partly deposited dropwise onto a DRP-110 Screen Printed Electrode (SPE) consisting of a carbon working electrode, a platinum counter electrode and a silver reference electrode. Graphite SPEs were chosen owing to their

superior characteristics over common carbon electrodes (Rowley-Neale et al., 2015).

Furthermore, with a view to simulating a system as close as possible to the industrial one, an experimental configuration with a continuous electrolyte flow was adopted for the evaluation of the performance of the samples towards HER. As shown in Figure 14, the apparatus consists of an electrolytic cell containing the sample deposited on an SPE and connected to the potentiostat through a cable system. The inlet and outlet electrolyte flows are regulated by a variable-flow peristaltic pump. This new system allows to reduce the process energy consumption by lowering the mass transfer resistance due to the hydrogen bubbles, both released in solution and deposited onto the electrode. Lastly, to evaluate the hydrogen amount produced in the electrolytic cell, quantities at different times were withdrawn from the electrolytic solution and examined through gas chromatography-mass spectrometry analysis, by the means of a Thermo Scientific FOCUS GC-ISQ Single Quadrupole MS. After obtaining the calibration curve from the analysis of known quantities of hydrogen, the amount of produced gas was evaluated from the areas under the peaks of interest and compared with the theoretical amount in order to calculate the hydrogen production efficiency.

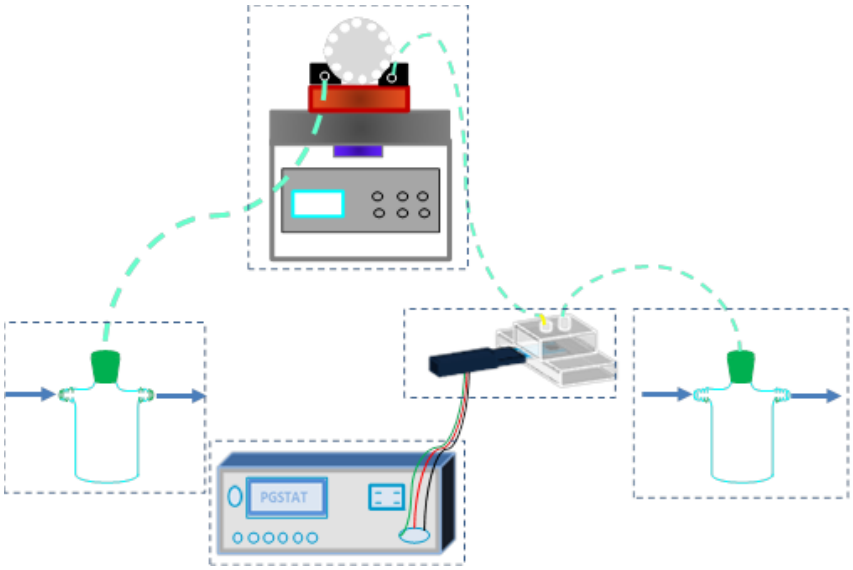

Figure 14. *Experimental apparatus for HER tests in a continuous electrolyte flow system*

1.2.3 Results and discussion

1.2.3.1 Morphological characterization

The morphological and structural characteristics of the samples were determined by transmission electron microscopy (TEM) and field emission scanning electron microscopy (FESEM) analysis. Both the microscopes were equipped with a EDX probe. With regard to the PtRh nanostructures, TEM images at different magnifications (scale bars: 200, 100 and 50 nm) showed the formation of nanoparticles with an average diameter of about 3 nm (Figures 15a, b and c) The result of the EDS analysis was also reported, displaying a Pt/Rh atomic ratio in line with the percentages of Pt and Rh in the precursors chosen for the synthesis, whilst the high-resolution TEM image showed an interplanar spacing of 2.610 Å, which did not match the ones of sole Pt and sole Rh, proving the presence of a PtRh alloy (Figures 15e, d and e).

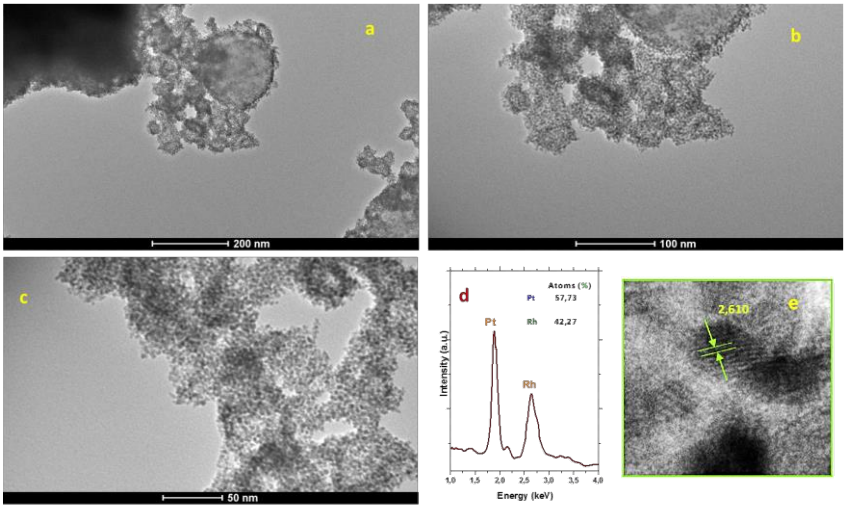

Figure 15. *TEM images of PtRh nanoparticles at different magnifications (a,b,c). In addition, EDS spectrum of PtRh is reported (d), along with a high-resolution TEM image showing a d spacing of 2.610 Å (e)*

In addition, in Figure 16, the high-resolution FESEM image and the corresponding EDX maps for each metal revealed, being superimposable on each other, that platinum and rhodium are homogeneously distributed in the sample, therefore confirming the formation of a binary alloy.

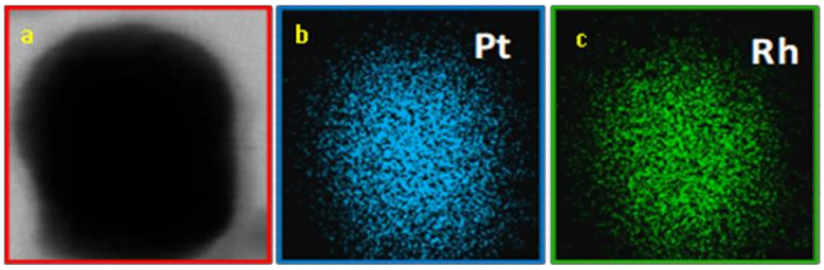

Figure 16. *FESEM image of PtRh (a) and EDX maps of platinum and rhodium (b,c)*

With reference to PtRh-MoS_2, TEM images at different magnifications (scale bars: 500, 200 and 100 nm) were also collected, showing that such nanocatalyst is constituted of nanostructures well separated from each other comprising PtRh nanoparticles covered with a few MoS_2 nanosheets (Figures 17a, b and c). Even in this case, the EDS analysis showed an atomic ratio in line with the percentages of the elements in the precursors (Figure 17d), proving the formation of a PtRh alloy, whose typical (111) crystalline

plane is distinctly highlighted in the high-resolution TEM image (Figure 17e), showing the corresponding interplanar distance of 2.610 Å, along with the MoS_2 nanosheets interplanar spacing of 6.210 Å (Rasamani et al., 2017).

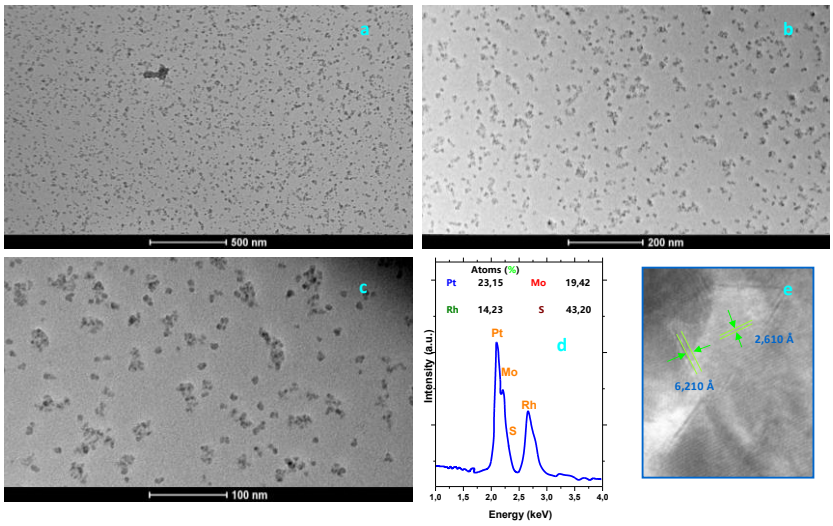

Figure 17. *TEM images of PtRh-MoS_2 nanostructures at different magnifications (a,b,c). Moreover, EDS spectrum of PtRh-MoS_2 is reported (d) together with a high-resolution TEM image showing the interplanar spacings of PtRh alloy and MoS_2 nanosheets (e)*

1.2.3.2 X-ray diffraction analysis

Figure 18 showed the X-ray patterns of Pt, PtRh and PtRh-MoS_2 nanostructures. As for the Pt nanoparticles, the diffraction peaks were coincident with the pure fcc Pt characteristic peaks (JCPDS: 04-0802) at 2θ: 39.79°, 46.24°, 67.45°, 81.29° and 85,70° (Shah et al., 2012). Regarding PtRh, the X-ray diffraction pattern clearly evidenced a slight up-shift of the peaks of pure Pt owing to the alloy formation. This phenomenon is due to the lattice contraction caused by the incorporation of Rh into the Pt lattice, which subsequently implies the purity of the formed PtRh alloy without undesired phases. Furthermore, the diffraction pattern of PtRh-MoS_2 also exhibits peaks slightly shifted to intermediate 2θ values with respect to the ones of pure metals, which proves again the existence of a PtRh alloy. These peaks cover the MoS_2 spectrum and lie between both of pure fcc Pt (JCPDS: 04-0802) and pure fcc Rh (JCPDS: 05-0685) at 2θ: 40.49°, 46.9°, 68.67° and 82.26°. Also, in the same pattern, an additional peak at 2θ ~ 60° can be recognized, which can be ascribed to the presence of MoS_2 nanosheets in the PtRh-MoS_2 nanostructure (Veeramalai et al., 2016).

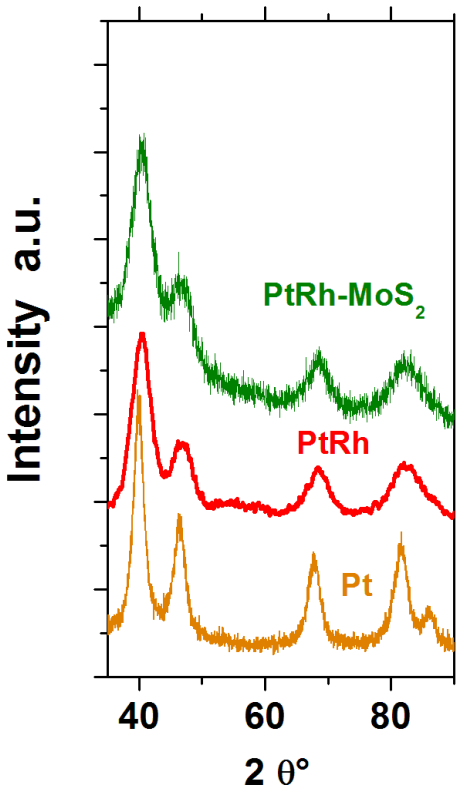

Figure 18. *X-ray diffraction patterns of Pt, PtRh and PtRh-MoS_2*

1.2.3.3 Electrochemical tests

The electrocatalytic activity towards HER of the synthesized nanomaterials deposited on a SPE was measured both by adopting a static 1 M H_2SO_4 solution and using the above-mentioned experimental configuration with a continuous electrolyte flow. Polarization curves for PtRh and PtRh-MoS_2 were reported in Figure 19, along with the polarization curve of Pt NPs for comparison. The samples exhibited, especially in the electrolyte flow configuration, negligible overpotentials, beyond which the cathodic current density (calculated as measured current divided by the geometric area of the electrode) increased very quickly under more negative working electrode potentials. In addition to that, these overpotential values were comparable to the ones of Pt NPs. Furthermore, starting from the polarization curves, the corresponding Tafel curves were built, and the linear

portions of these curves were fitted by the Tafel equation (Sarno et al., 2017a; Sarno et al., 2017b), leading to very low Tafel slopes.

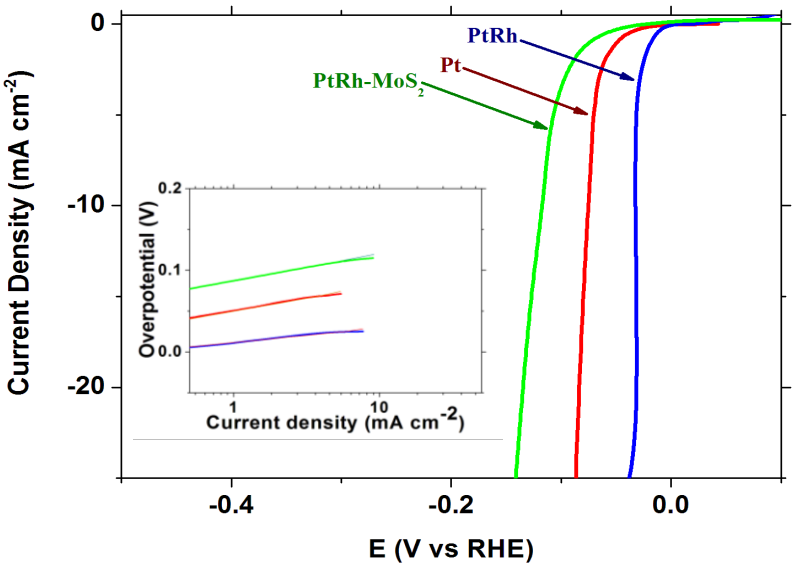

Figure 19. *Polarization curves at 20 mV/sec of Pt, PtRh and PtRh-MoS_2 nano-electrocatalysts obtained with a continuous electrolyte flow system. In the insert, Tafel plots for Pt, PtRh and PtRh-MoS_2 obtained with the same system*

More specifically, overpotentials and Tafel slopes for PtRh and PtRh-MoS_2 were reported in Table 1, rows eleven and twelve, respectively. Since polarization curves were iR corrected, Tafel slopes for the static and the electrolyte flow system were very similar. Therefore, only Tafel slopes obtained using the latter system were reported, each of them indicating a high reaction rate (18 and 32.7 mV/dec for PtRh and PtRh-MoS_2 respectively), whereas overpotentials measured on PtRh and PtRh-MoS_2 in the flow configuration were negligible. Values from scientific literature, chosen among the most performing nano-electrocatalysts thus far studied, were also reported in the same Table. The comparison evidenced that the samples are extremely promising in terms of electrocatalytic performances: both PtRh and PtRh-MoS_2 showed an excellent behavior towards HER, comparable with that of pure platinum and other performing materials. It is well established that Pt is the most performing electrocatalyst towards HER. After all, results showed that alloying it with Rh, which is placed close to Pt at the summit of Trasatti's volcano plot (Quaino et al., 2014), provided remarkable HER performance with a reduced Pt amount. In particular, the

Tafel slope observed for PtRh was lower than the typical value for a Volmer-Tafel mechanism, that is 30 mV/decade, suggesting a different catalytic mechanism in the presence of Rh. On the other hand, a spillover effect, a phenomenon in which an adsorbed H atom on Rh may easily migrate to other sites, could be the reason for this behavior (Zhu L. L. et al., 2016). Moreover, MoS_2, which probably worked as catalyst itself because of its abundant catalytically active exposed edges, acted as a noble metal electron enhancer as well as an additional surface for spillover, simultaneously exhibiting a stabilizing effect.

Table 1. *Comparison of HER performances between the synthesized samples and some of the most performing nano-electrocatalysts reported in the literature*

	Pt wt. %	**Tafel slope [mV/dec]**	**Overpotential [V *vs.RHE*]**	**Ref.**
NiPt-Ni_2Pt	77-62	146 - 134	--	Domínguez-Crespo et al., 2012
AuPt	50	34	<0.01	Weng et al., 2016
MoS_2/RGO	-	41	>0.1	Li et al., 2011
MoS_2	-	94	>0.2	Sarno et al., 2017a
NiSMoS_2G	-	~40	~0.08	Sarno et al., 2017a
fct-FePt	>63	--	>0	Li et al., 2015
Pd/Pt	~49	Volmer-Heyrovsky mechanism	0.05	Ojani et al., 2013
Cu/Pt	~35	Volmer-Heyrovsky mechanism	Negligible	Raoof et al., 2010
Pt@Te-rGO/polyimide	-	55	0.04	Zhang et al., 2015
Pt/PtO_2	-	31	Negligible	Sarno et al., 2017a
PtRh	73	18	Negligible	This work
PtRh-MoS_2	47	32.7	Negligible	This work

In fact, stability over time of the synthesized electrocatalysts was also tested (see Figure 20). The continuous cycling voltammogram evidenced high durability, especially for PtRh-MoS_2. The initial polarization curve was compared with the curve obtained after 2000 cycles and the two curves appeared almost overlapped, proving the high stability of the sample likely due to the MoS_2 coating.

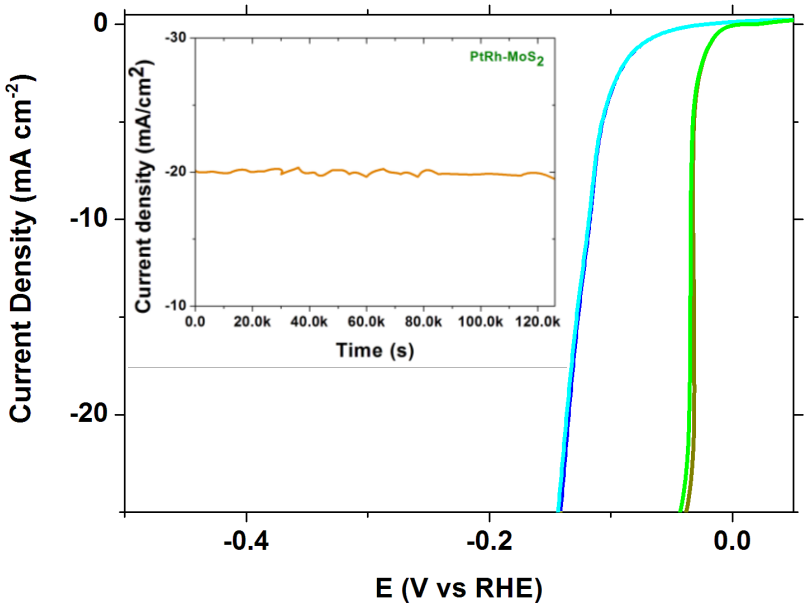

Figure 20. *Stability tests: cycling voltammetry before and after 2000 cycles for PtRh and PtRh-MoS_2. In the insert, current density-time curve for PtRh-MoS_2 at -0.13 V*

On the other hand, the X-ray diffraction analysis after cycles shows a well-conserved structure for both the nanocatalysts (Oliveira et al., 2008), as can be seen from Figure 21.

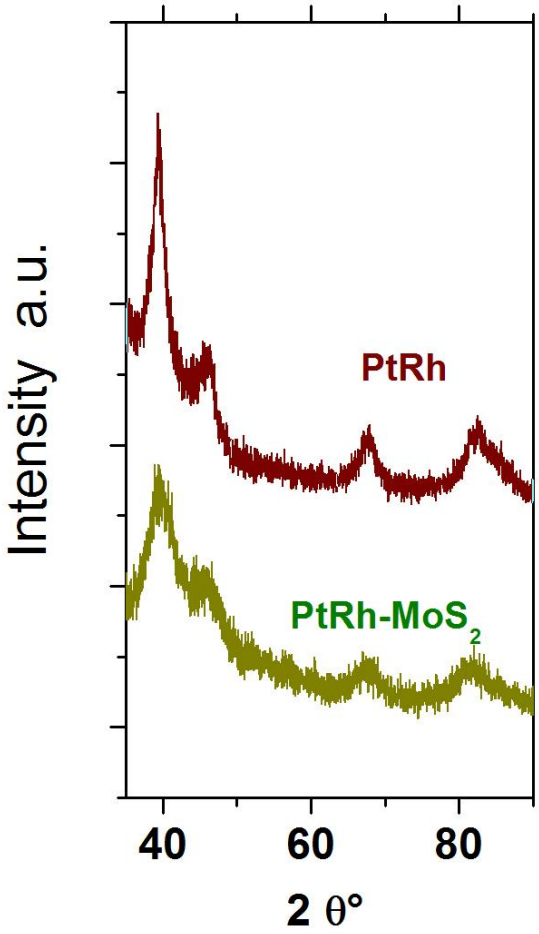

Figure 21. *X-ray diffraction patterns of PtRh and PtRh-MoS_2 after electrochemical tests*

Overall, the results indicated that PtRh-MoS_2 nanomaterial, constituted of Pt/Rh nanoparticles stabilized by the MoS_2 coating, can be a useful, stable and efficient alternative HER catalyst. Furthermore, the amount of hydrogen produced using PtRh-MoS_2 nanocatalysts was evaluated. The volumes of hydrogen produced at several times, evaluated from Faraday's laws of electrolysis at a voltage of -0.13 V, were plotted in Figure 22 (orange line). They were also analyzed through gas chromatography-mass spectrometry and the quantities of hydrogen detected (red points) were in good agreement with theoretical data obtained when considering the number of charges passing through the system, which proved a high hydrogen production efficiency.

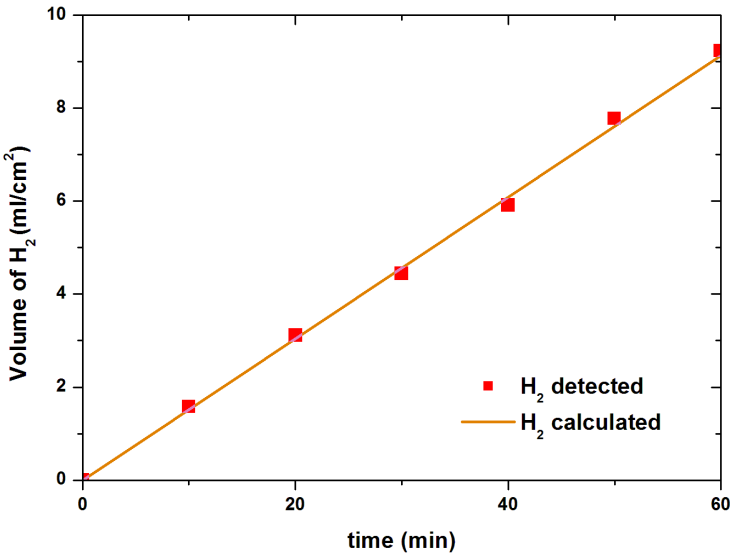

Figure 22. *Volume of hydrogen produced (in red) and theoretically evaluated (in orange). The volume of hydrogen was calculated and detected on PtRh-MoS_2 electrode in a 1M H_2SO_4 solution at -0.13 V.*

1.2.4 Conclusion

In summary, PtRh and PtRh-MoS_2 nano-electrocatalysts have been successfully prepared through a scalable, economic, one-step synthesis. Analyses of XRD results, SEM and TEM images and EDX maps revealed the formation of bimetallic PtRh alloy nanoparticles with average diameters up to 3-4 nm. In the PtRh-MoS_2 sample, the PtRh alloy nanoparticles are covered with a few MoS_2 nanosheets, which thanks to their reduced dimensions expose high edges surface.

PtRh shows excellent HER activity, comparable to the one of pure Pt, and this can be regarded as a consequence of the synergistic effect deriving from alloying the two metals, both of which located at the summit of the Trasatti's volcano plot. In particular, the PtRh Tafel slope value suggests a different catalytic mechanism in the presence of a small amount of Rh, i.e. hydrogen production takes advantage of a spillover effect. Indeed, According to DFT calculations, in acidic aqueous environment, the hydrogen ions quickly adsorb on the surface of Rh, as in eq. (1). During the HER, hydrogen atoms already adsorbed on the Rh surface can quickly migrate to Pt surface, as in eq. (2): H^+ are therefore more quickly available for the HER on the more

active Pt surface, hence increasing the reaction rate and the H_2 generation, as in eq. (3) (Zhu L. L. et al., 2016).

$$Rh{-}Pt + H^+ + e^- \rightarrow H{-}Rh{-}Pt \quad (1)$$

$$H{-}Rh{-}Pt \rightarrow Rh{-}Pt{-} H \ \text{(spillover)} \quad (2)$$

$$Rh{-}Pt{-} H + H^+ + e^- \rightarrow H_2 + Rh{-}Pt \quad (3)$$

Moreover, MoS_2, probably working as catalyst itself with its abundant exposed edges, acts as a noble metal electron enhancer, as an additional surface for spillover and possesses a stabilizing effect.

Chapter 2:
New nano-structured catalysts for the hydrogen evolution reaction in seawater

2.1 Nano-structured catalysts for the hydrogen evolution reaction (HER) in seawater: State of the Art

In this second chapter, novel nano-structured catalysts were prepared and tested for the catalysis of the HER in real seawater. As previously mentioned, water electrolysis as a promising technique to produce highly pure and clean hydrogen at room temperature and pressure is on the rise. The search for new cost-effective electrocatalysts capable of ensuring high activity towards the hydrogen evolution at the cathode and good stability in the electrolysis environment is the most crucial step for the industrial-scale development of this technology (Sarno et al., 2015). To date, most of the current literature focuses on the HER characterization in a mixture of distilled water and acid or alkaline electrolytes. However, an interesting and attractive alternative would be the electrochemical generation of H_2 from seawater, which can bring several advantages over the "traditional" water splitting. Indeed, about 97% of the water present in nature originates from seas and oceans; hence, it is easily, abundantly and freely available as seawater (Kalogirou et al., 2005). In addition, by directly feeding seawater to an electrolyzer, the expensive and energy-consuming purification and desalination processes, such as reverse osmosis, vacuum distillation, multistage flash distillation, freeze-thaw, and electrodialysis, are not required (Lin et al., 2021; Kim et al., 2019). Rather, seawater salts are crucial, acting

as charge carriers themselves during electrolysis. Consequently, since these carriers are highly present in seawater, further addition of acid or basic electrolytes cannot be needed. Therefore, production costs are reduced, i.e. no costs for water distillation and for disposal of electrolytes and removed residual salts. On the other hand, the high presence and variety of salts can generate a corrosive environment for the catalysts. Moreover, in the not purified seawater, there are hundreds of different impurities, which might lead to catalyst poisoning.

However, to date, there are a few studies dealing with the production of hydrogen from seawater, with results that are still far from being satisfactory, especially with respect to the use of a catalyst consisting predominantly of inexpensive materials.

For instance, Golgovici et al. (2018) prepared several Ni–Mo alloy nanostructures through electrochemical deposition from aqueous (NiMo1) and choline chloride-based ionic liquid (NiMo(ILC))-based electrolytes. Among the synthesized catalysts, Ni–Mo alloys electrodeposited on Ni foams showed a better behavior towards HER in natural seawater, probably due to the combination of a porous structure and alloying elements, with an overpotential of around 0.152 *vs.Ag/AgCl* and Tafel slopes in the range of 105–120 mV/dec (see Figure 23).

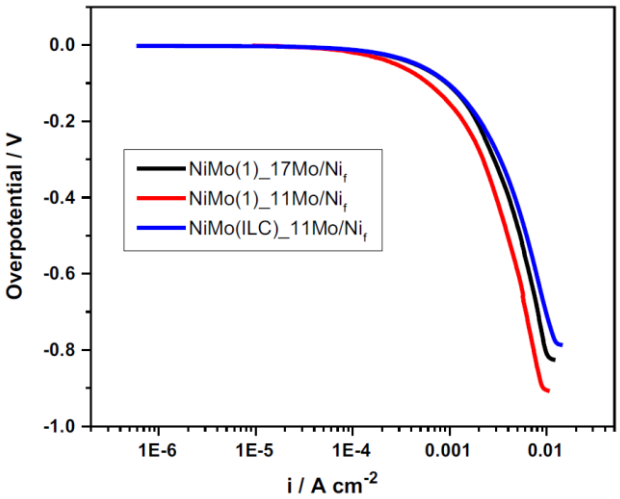

Figure 23. *Tafel plots for HER in seawater for Ni–Mo alloys with different Mo loading electrodeposited from NiMo(1) and NiMo(ILC) electrolytes on Ni foam (Ni$_f$). Reprinted with permission from (Golgovici F., A. Pumnea, A. Petica, A. C. Manea, O. Brincoveanu, M. Enachescu and L. Anicai (2018) Chem. Pap. Ni–Mo alloy nanostructures as cathodic materials for hydrogen evolution reaction during seawater electrolysis. Chem. Pap.* ***72****, 1889-1903). Copyright (2021) Springer Nature*

Gao et al. (2015) prepared nitrogen-doped, cobalt-encased carbon nanotubes starting through cost-effective reactants such as cobalt chloride hexahydrate ($CoCl_2 \cdot 6H_2O$) and urea. In particular, the sample synthesized at 900 °C (named U-CNT-900) exhibited the best HER catalytic performance among the other samples prepared in the same study (see Figure 24). However, since activity in real seawater was weak, the authors tested U-CNT-900 in a more conductive neutral buffer (phosphate buffer with pH=7) seawater, obtaining a lower overpotential of around 0.5 V *vs.RHE* and good stability without significant current losses for 7 hours at a potential of 0.27 V *vs.RHE*. The authors attributed the good activity of the catalyst to a synergistic effect between carbon-coated Co NPs and N dopants, and its high durability to the high tolerance of nanocarbon-based materials towards seawater impurities.

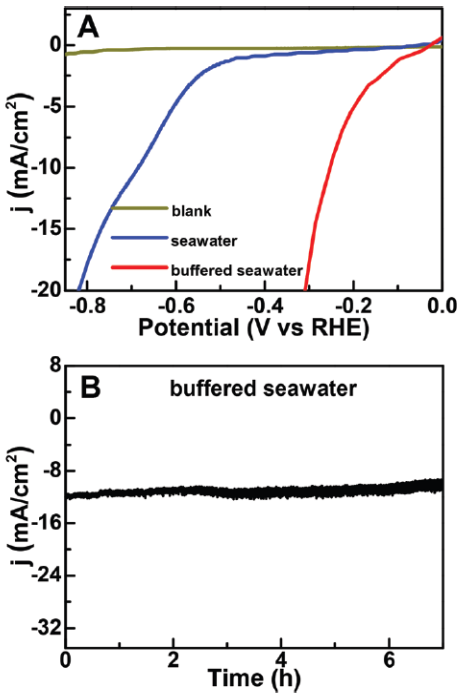

Figure 24. *HER polarization curves without catalyst (yellow line, blank experiment) in buffered seawater (pH 7), with U-CNT-900 in natural seawater (blue line) and in buffered seawater (red line, pH 7); (B) Chronoamperometry test for U-CNT-900 at 0.27 V vs.RHE. Reprinted with permission from (Gao S., G. D. Li, Y. Liu, H. Chen, L. L. Feng, Y. Wang, M. Yang, D. Wang, S. Wang and X. Zou (2015) Electrocatalytic H_2 production from seawater over Co, N-codoped nanocarbons. Nanoscale, 7, 2306-2316). Copyright (2021) Royal Society of Chemistry*

Ma et al. (2017) prepared cobalt-, molybdenum-, phosphide-based nanocrystals coated by few-layer N-doped carbon shell (named as CoMoP@C) through a one-step pyrolysis method. The HER performance of the catalyst was tested both in real and simulated seawater, comparing it with the ones of commercial 20% and 40% Pt on carbon.

As can be seen from Figures 25a and b, in simulated seawater, CoMoP@C maintained its catalytic activity unaltered for 10 cycles, while the activities of 20% and 40% Pt/C declined significantly between the 5^{th} and the 10^{th} cycle. Similarly, in real seawater (see Figure 25c), the activity of CoMoP@C reduced only by 5% within 20 cycles of tests, while a sharp plummet in the activities of 20% and 40% Pt/C could be observed under the same conditions. This trend is confirmed by the chronoamperometry test reported in Figure 26, which shows that CoMoP@C recorded no significant current losses for 10 hours, while current densities of 20% and 40% Pt/C decreased remarkably during this time period. According to the authors, these results can be ascribed to several reasons such as: the lower H^+ adsorption on the central CoMoP crystalline core, the strong H^+ adsorption capacity of N-doped carbon shell, increasing the proton concentration around the CoMoP cores, as well as the protection from the impurities of seawater received by the same N-doped graphitic carbon shell.

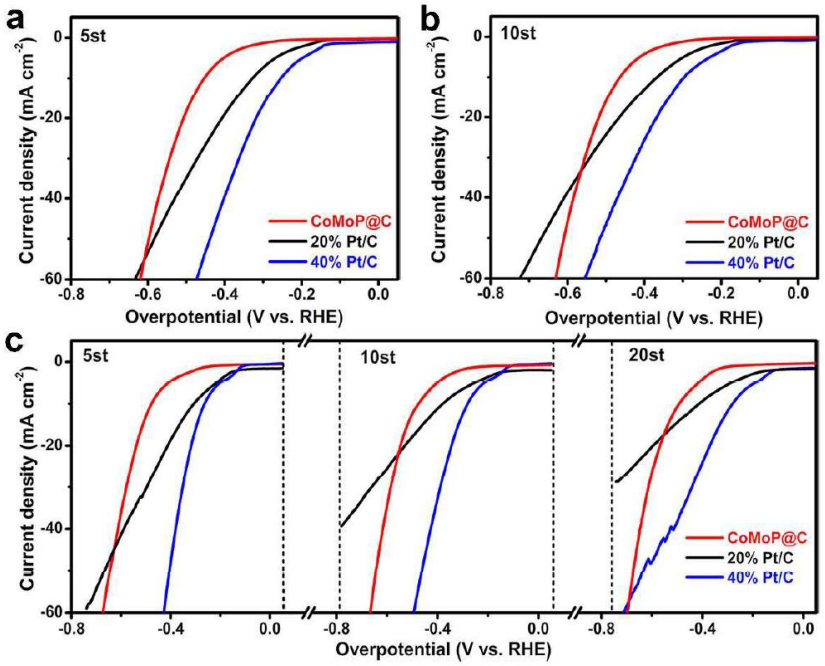

Figure 25. *(a-b) HER Polarization curves of CoMoP@C, 20% and 40% Pt/C in simulated seawater at scan rate of 5 mV/sec after the 5th and 10th cycles. (c) HER polarization plots of CoMoP@C, 20% and 40% Pt/C catalysts in real seawater at scan rate of 5 mV/sec after the 5th,10th and 20th cycles. Reprinted with permission from (Ma Y. Y., C. X. Wu, X. J. Feng, H. Q. Tan, L. K. Yan, Y. Liu, Z. H. Kang, E. B. Wang and Y. G. Li (2017) Highly efficient hydrogen evolution from seawater by a low-cost and stable CoMoP@C electrocatalyst superior to Pt/C. Energy Environ. Sci., **10**, 788-798). Copyright (2021) Royal Society of Chemistry*

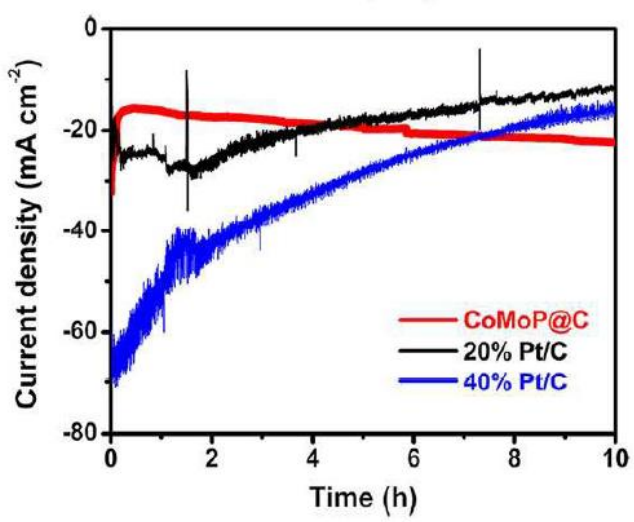

Figure 26. *Chronoamperometry tests for CoMoP@C, 20% and 40% Pt/C in seawater at 0.5 V for 10 hours. Reprinted with permission from (Ma Y. Y., C. X. Wu, X. J. Feng, H. Q. Tan, L. K. Yan, Y. Liu, Z. H. Kang, E. B. Wang and Y. G. Li (2017) Highly efficient hydrogen evolution from seawater by a low-cost and stable CoMoP@C electrocatalyst superior to Pt/C. Energy Environ. Sci., **10**, 788-798). Copyright (2021) Royal Society of Chemistry*

Song et al. (2010) studied the HER electrochemical activity in simulated seawater (3.5% NaCl, 90 °C and pH=12) of a Ni-Fe alloy on carbon (Ni-Fe-C) electrodes electrodeposited at current densities ranging from 100 to 300 A/m^2. As can be seen from Figure 27, at a current density of 0.12 A/cm^2, Ni-Fe-C electrodes electrodeposited at a current density of 200 A/m^2 showed the lowest overpotential of 0.7 V *vs.Hg/HgO*.

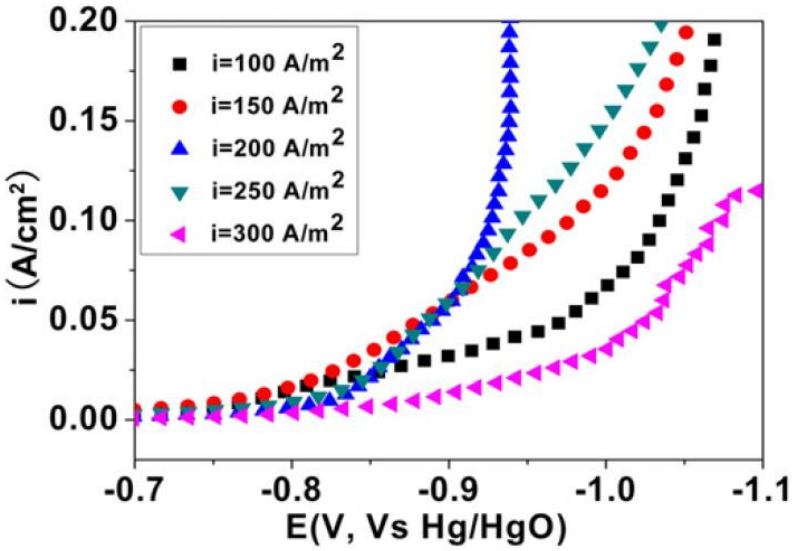

Figure 27. *HER polarization curves in seawater of Ni-Fe-C electrodes electrodeposited at different current densities. Reprinted with permission from (Song L. J. and H. M. Meng (2010) Effect of carbon content on Ni–Fe–C electrodes for hydrogen evolution reaction in seawater. Int. J. Hydrog. Energy, **35**, 10060-10066) Copyright (2021) Elsevier*

Niu et al. (2016) proposed the synthesis of robust electrodes for seawater splitting obtained through electrodeposition of RuCo and $RuCoMo_x$ alloys on titanium foil. The HER polarization curves and corresponding Tafel plots in Figure 28 show that: (1) the overpotential of the binary RuCo-based electrode was of -0.25 V *vs.RHE*, while the Ti foil supported $RuCoMo_x$-based electrode showed more negative overpotentials in the range 0.35-0.37 V *vs.RHE* and; (2) The Tafel slope of the RuCo/Ti was the smallest (107 mV/dec), suggesting a faster proton discharge kinetics on the bimetallic electrode compared to the trimetallic one. According to the authors, this can be due mainly to: (i) the higher percentage of Ru in the bimetallic RuCo alloy rather than in the trimetallic $RuCoMo_x$ alloy, suggesting the importance of Ru in the HER catalysis; (ii) the presence in the $RuCoMo_x$ electrode of some Ru atoms in their oxidized form (RuO_2), which has a higher potential for HER activation; (iii) the rougher surface of the RuCo-based electrode, which means higher surface area available for catalysis; (iv) the stronger hydrogen atoms adsorption energy on Mo atoms, which acts as a blockage to the reaction.

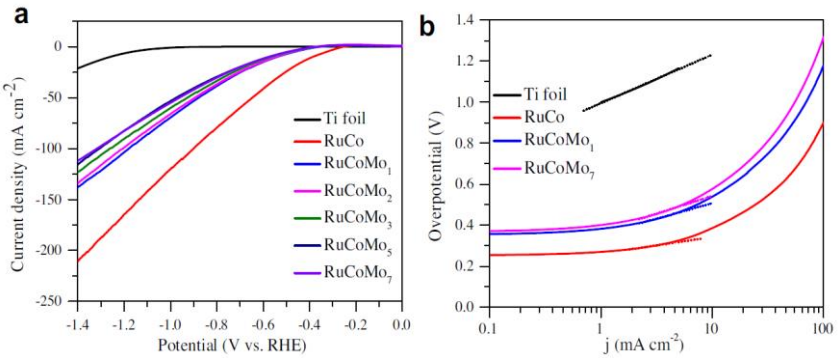

Figure 28. *(a) HER polarization curves in sewater of Ti foil and Ti foil supported RuCo, RuCoMo$_x$ electrodes. (b) Corresponding Tafel polarization plots. Reprinted with permission from (Niu X., Q. Tang, B. He and P. Yang (2016) Robust and stable ruthenium alloy electrocatalysts for hydrogen evolution by seawater splitting. Electrochim. Acta,* ***208****, 180-187). Copyright (2021) Elsevier*

Furthermore, the authors evaluated the long-term stability of the samples during 12 hours of activity. As shown in Figure 29, current density for the binary alloy-based electrode retained 70% of its original value, whereas, for the RuCoMo$_x$-based electrodes, there were no obvious current losses over 12 hours of test, suggesting higher stability in seawater. This can be ascribed, according to the authors, to the fact that the Ru-3d core level peaks of RuO_2 are not modified during catalysis, therefore protecting Ru, the most active metal in the trimetallic alloy, from corrosion.

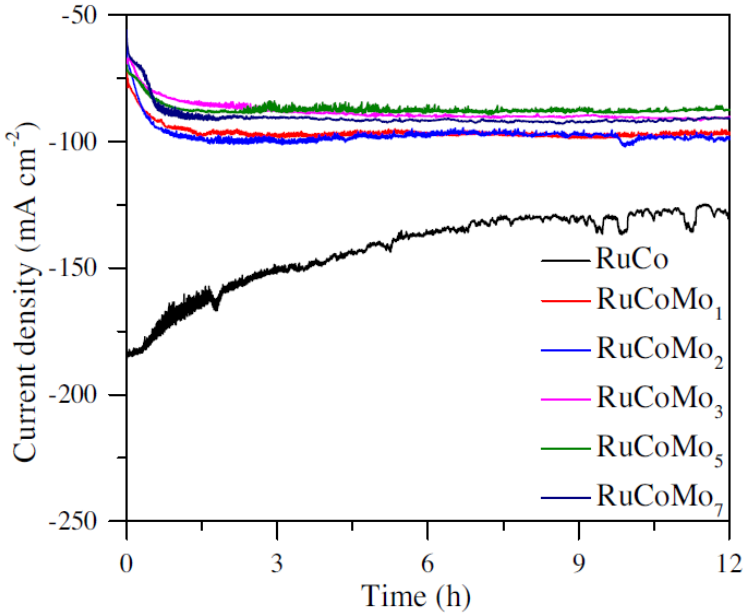

Figure 29. *Chronoamperometry tests for Ti foil supported RuCo and $RuCoMo_x$ in seawater at -1.2 V vs.RHE for 12 hours. Reprinted with permission from (Niu X., Q. Tang, B. He and P. Yang (2016) Robust and stable ruthenium alloy electrocatalysts for hydrogen evolution by seawater splitting. Electrochim. Acta, **208**, 180-187). Copyright (2021) Elsevier*

Li H. et al. (2016) tested the efficiency of platinum in seawater by comparing the pure metal with alloyed Pt-Ru-M (M = Cr, Fe, Co, Ni, Mo) decorated titanium mesh, synthesized by a simple electrodeposition approach. In Figure 30, HER polarization curves in seawater of the trimetallic alloys are reported, along with the ones of pure Ti, pure Pt, and bimetallic PtRu for comparison. It can be clearly observed that trimetallic alloys showed the highest performance, with Pt-Ru-Mo as the most performing one. For instance, current densities Pt-Ru-Cr, Pt-Ru-Fe, Pt-Ru-Co, Pt-Ru-Ni, Pt-Ru-Mo at -0.8 V were -45.04, -50.48, -55.02, -60.77, -65.00, and -69.54 mA/cm^2, respectively, while Pt-Ru and pure Pt exhibited the lower values of -45.04 and -39.61 mA/cm^2, respectively.

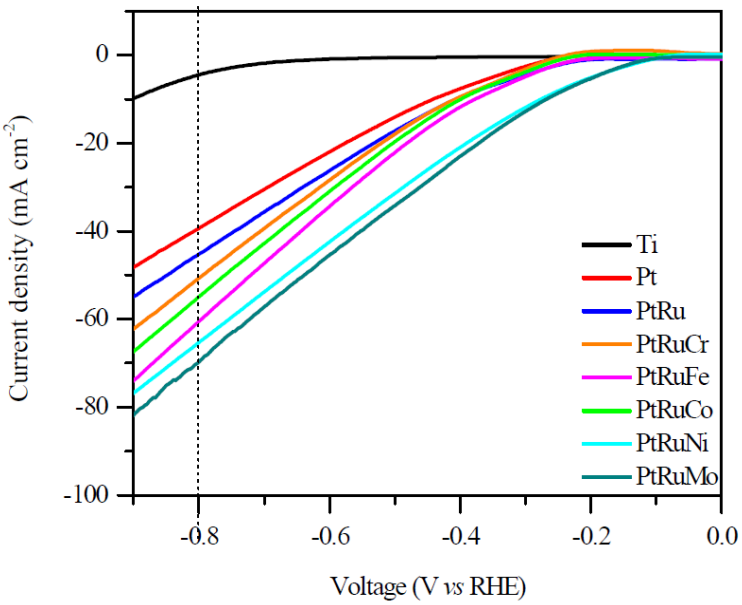

Figure 30. *HER polarization curves in seawater of pure Ti, pure Pt, bimetallic PtRu and trimetallic PtRuCr, PtRuFe, PtRuCo, PtRuNi and PtRuMo. Reprinted with permission from (Li H., Q. Tang, B. He and P. Yang (2016) Robust electrocatalysts from an alloyed Pt–Ru–M (M = Cr, Fe, Co, Ni, Mo)-decorated Ti mesh for hydrogen evolution by seawater splitting. J. Mater. Chem. A,* ***4,*** *6513-6520). Copyright (2021) Royal Society of Chemistry*

According to the authors, the superior HER performance of the trimetallic alloys is due to synergistic effects between metals such as nanoporous structure, higher catalytically active surface and enrichment of the electron density on the Pt surface caused by the presence of the other metals. In particular, molybdenum is the optimum third metal of the alloy, since it has the highest H^+ adsorption energy when compared with Fe, Co, Cr and Ni. Indeed, since Pt has a moderate H^+ adsorption energy, alloying with a metal, such as Mo, which possesses higher energy would be desirable for increasing Pt catalytic performance towards the reaction. This is clear when looking at the volcano plot in Figure 31.

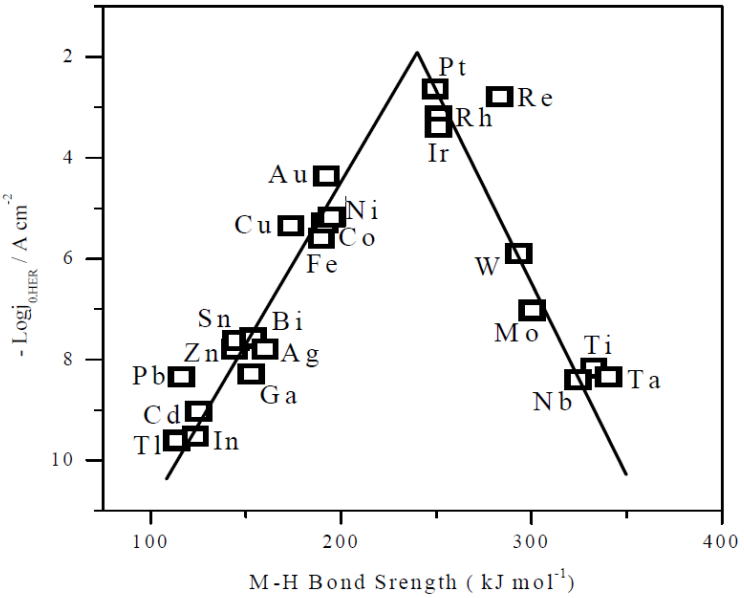

Figure 31. *Volcano plot showing the relationship between logj_0 values for the hydrogen evolution reaction and metal- H^+ proton bond energy. Reprinted with permission from (Li H., Q. Tang, B. He and P. Yang (2016) Robust electrocatalysts from an alloyed Pt–Ru–M (M = Cr, Fe, Co, Ni, Mo)-decorated Ti mesh for hydrogen evolution by seawater splitting. J. Mater. Chem. A,* ***4,*** *6513-6520). Copyright (2021) Royal Society of Chemistry*

Moreover, chronoamperometry tests at -0.8 V *vs.RHE* in seawater (see Figures 32a and b proved (i) the good long-term stability of the synthesized alloys for 50000 sec and (ii) the superiority of the Pt-Ru-Mo alloy over the other catalysts, since it retained its original current density value for over 172 hours of test, with only a 2.1% current loss. The enhanced anticorrosion of the Pt-Ru-M catalysts, and, above all, of the Pt-Ru-Mo alloy can be explained with the competitive dissolution reactions between the different components of the alloy with gaseous Cl_2 dispersed in seawater after being produced from the reduction of Cl^- ions at the anode. Indeed, dissolution of the three metals in presence of Cl^- is thermodynamically spontaneous (i.e. ΔG is strongly negative), but for Pt the absolute value of ΔG is much smaller.

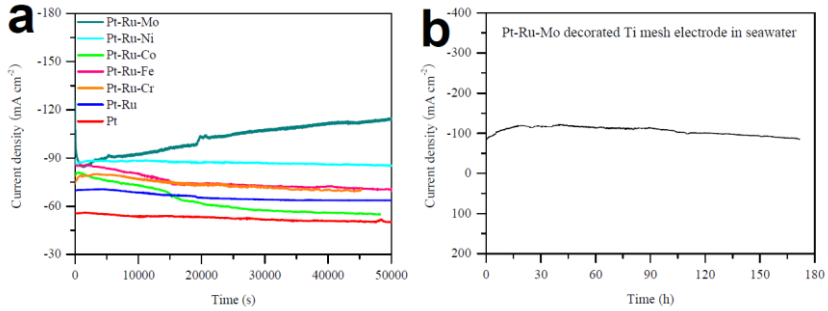

Figure 32. *(a) Chronoamperometry tests for Pt, Pt-Ru, Pt-Ru-Cr, Pt-Ru-Fe, Pt-Ru-Co, Pt-Ru-Ni and Pt-Ru-Mo recorded at -0.8 V vs RHE in seawater for 50000 sec. (b) Chronoamperometry test for Pt-Ru-Mo decorated Ti mesh electrode -0.8 V vs RHE in seawater for 172 hours. Reprinted with permission from (Li H., Q. Tang, B. He and P. Yang (2016) Robust electrocatalysts from an alloyed Pt–Ru–M (M = Cr, Fe, Co, Ni, Mo)-decorated Ti mesh for hydrogen evolution by seawater splitting. J. Mater. Chem. A,* ***4,*** *6513-6520). Copyright (2021) Royal Society of Chemistry*

From the analysis of the reported literature, it emerged that trimetallic alloys can behave better in a seawater environment, especially from the point of view of stability. Usually, they comprise a more active metal, which can be protected from the environment by the other two ones.

Furthermore, materials such as graphene-based one and transition metal dichalcogenides (TMDs) can be also considered as valid and more economic catalysts and/or supports for the hydrogen evolution in seawater. For instance, Chen I. W. P. et al. (2019) synthesized, through a simple one-pot hydrothermal approach, three-dimensional (3D) MoS_2 quantum dots aerogel (named as MoS_2QD-aerogel). It is worth noticing that, as can be seen from Figure 33, this material tested in real seawater exhibited much better stability to deactivation and corrosion than commercial Pt, remaining stable for 150 scanning cycles, whereas Pt performance significantly decreases after 50 cycles. Moreover, the MoS_2-based catalyst remained at an almost identical potential for 150 cycles at a current density of 80 mA/g, whereas commercial Pt showed a decreasing potential throughout the various cycles. This can be attributed to the porous morphology of MoS_2 which is believed to favor ions adsorption and/or the subsequent water dissociation onto its surface. On the other hand, it is also clear that platinum, top catalyst for the HER in acid media, is not as valid in a seawater environment, where it can be more easily deactivated due to the presence of many impurities.

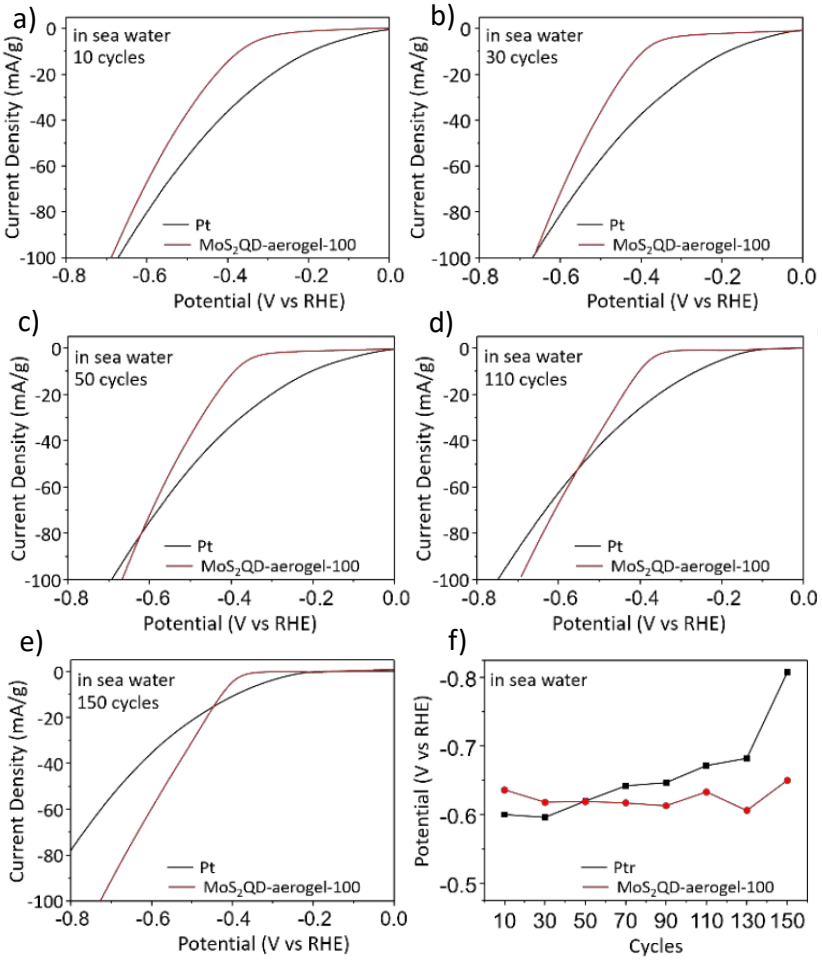

Figure 33. *(a-e) HER polarization curves at 10,30,50,110,150 cycles of MoS_2QD-aerogel-100 catalyst and commercial Pt in real seawater. (f) Potential vs. test cycles of MoS_2QD-aerogel-100 and commercial Pt in real seawater. Reprinted with permission from (Chen I. W. P., C. H. Hsiao, J. Y. Huang, Y. H. Peng and C. Y. Chang (2019) Highly Efficient Hydrogen Evolution from Seawater by Biofunctionalized Exfoliated MoS_2 Quantum Dot Aerogel Electrocatalysts That Is Superior to Pt. ACS Appl. Mater. Interfaces, **11**, 14159-14165) Copyright (2021) American Chemical Society*

2.2 Design of novel nano-structured electrocatalysts for electrochemical seawater splitting at the cathode

2.2.1 Introduction: reasons behind the choice of the catalysts

As could be inferred from the analysis of the current (and few) literature data available on the topic, it is fundamental to design new, economic and efficient nano-structured catalysts for HER catalysis in seawater, not only capable of ensuring low overpotential and low Tafel slopes but also, and above all, high tolerance towards impurities and high stability and resistance to corrosive environments. Therefore, much more effort must be done in order to improve activity and stability in seawater. In this scenario, the adoption of ternary metallic alloy-based nanostructures and even quaternary nano-structured catalysts enables wider possibilities regarding the choice of components and the exploitation of new alloy properties and functionalities, with the aim of optimizing activity, costs and resistance to corrosion. As mentioned also in the previous chapter, pure platinum has been accurately explored in virtue of its remarkably high electrocatalytic activity towards a considerable number of reactions. Nonetheless, the industrial-scale adoption of Pt has been significantly hindered by its scarce availability, high cost and, as pointed out in the previous section, low tolerance to poisoning as well, leading to the need for better alternatives (Liu D. et al., 2017). Therefore, in the following part of the PhD project, novel ternary alloy and quaternary compound-based nanostructures have been explored without including platinum. In detail, the following electrocatalysts have been prepared:

1) Ni-Ru-Ir alloy nanoparticles supported on few-layer graphene, named as NiRuIr_G in the following text.

Indeed, Iridium is a Pt-group metal which shows the highest corrosion resistance among metals, high stability towards dissolution and oxidation, as well as a good activity towards HER with a wide range of oxidation states (Štrbac et al., 2018). On the other hand, among the platinum-group metals yet less expensive than Pt, ruthenium has attracted increasing interest for the HER catalysis in alkaline media since it efficiently favors H_2O dissociation (Chen C. H. et al., 2019). Furthermore, its hcp structure makes Ru highly resistant to chemical attack during electrocatalytic processes (Zhang Q. et al., 2018). Nickel is the commercial catalyst for HER and is considered a good catalyst for HER in alkaline solutions owing to its high activity and low cost (Yu et al., 2014). Furthermore, it has been proved that the presence

of carbonaceous materials as support can help stabilize metals by favoring water dissociation on them, hence increasing their HER activity (Gao et al., 2015). Among carbon materials, graphene is very promising (Sarno et al., 2012) as effective catalyst support in virtue of its high stability and electron mobility as well as of its high tolerance towards impurities.

2) Ru-Os-RuO_2-OsO_2-based nanostructures supported on few-layer graphene, named as RuOs_G in the following text.

In this catalyst, ruthenium and graphene have been also chosen for the above-mentioned reasons. Furthermore, osmium has been introduced, which has never been done in the literature so far. The chemistries of ruthenium and osmium are similar (Li H. et al., 2016) and both are among Pt-group metals, yet less expensive than platinum. In addition, Os has a wide range of oxidation states and is the only other element known to have an oxidation state of 8. It is a very stable and strong material, with electronegativity at the different oxidation states higher than that of Ru. Moreover, the presence of RuO_2 and OsO_2 is fundamental since the oxides favor the accumulation of charges on Os and Ru catalytic sites.

2.2.2 Materials and methods

2.2.2.1 NiRuIr_G preparation

As for the synthesis, a surfactant-free approach was chosen (Sarno et al., 2019a) and designed here for the specific new nanocatalyst. For NiRuIr_G catalyst: ruthenium(III) chloride hydrate (0.5 mmol), nickel(II) chloride (0.5 mmol) and sodium hydroxide (0.288 g) were added to a solution of ethylene glycol (66 mL) and water (6 mL); the mixture was stirred for 30 min at 25 °C and then heated up till 130 °C for an hour; 3 mL of solution was withdrawn from the system; iridium(III) chloride (0.5 mmol) was added to the withdrawn solution, which was then re-injected into the reactor and maintained at 130 °C for 2 additional hours under nitrogen flow. Afterward, the solution was cooled down to room temperature, few-layer graphene (0.5 g) was added, and the mixture was further stirred for 24 hours without increasing its temperature. Finally, it was treated with acetone in order to remove ethylene glycol. Finally, the sample underwent a post-synthesis treatment in an autoclave under the following conditions: the reaction proceeded for 3 hours at 205 °C and at 10 bar under a 5 vol.% hydrogen/nitrogen flow (5 vol.% H_2).

2.2.2.2 RuOs_G preparation

RuOs_G nanostructures were produced using the following chemicals: ruthenium acetylacetonate (0.15 mmol), osmium(III) chloride (0.15 mmol), physical exfoliation of graphite (3 mmol), benzyl ether (20 mL) as reaction solvent, 1,2-hexadecanediol (10 mmol) as reducing agent, oleic acid (6 mmol) and oleylamine (6 mmol) as surfactants. Physical exfoliation of graphite (G) consisting of a few layers of graphene, largely monolayer, was obtained by sonication of graphite powder (microcrystalline,−300 mesh) in N-methylpyrrolidone (Guadagno et al., 2015). Oleylamine here acts also as a stabilizer and mild reducing agent, in virtue of its ability to give electrons as temperature increases (Mourdikoudis et al., 2013).

Precursors underwent thermal reduction under N_2 flow, carried out by heating the mixture till 200 °C for 2 hours and further heating it till 285 °C for 1 hour. After the synthesis, the sample underwent an additional treatment in order to remove most of the organic chains covering the nanostructures, which otherwise would hinder the charge transfer process. The treatment consists in heating up the sample under airflow, from room temperature up to 150 °C at 10 K/min for 8 hours (Sarno et al. 2019b).

2.2.2.3 Methods

A FEI Tecnai electron microscope was used to obtain transmission electron microscopy (TEM) images, whereas field emission scanning electron microscopy (FESEM) images were acquired through a LEO 1525 electron microscope, equipped with an energy dispersive X-ray (EDX) probe. Moreover, a Bruker D8 X-ray diffractometer (CuKα) was used for XRD measurements.

To perform electrochemical tests, 4 mg of each sample were dispersed in 80 µl of a 5 wt% Nafion solution to form a homogeneous ink. Afterward, the catalyst ink was loaded onto a DRP-110 Screen Printed Electrode (SPE) consisting of a carbon working electrode, a platinum counter electrode and a silver reference electrode. As mentioned in the previous chapter, also in this case, graphite SPEs were chosen owing to their better performance over common carbon electrodes (Rowley-Neale et al., 2015). Electrochemical experiments were carried out by means of an Autolab PGSTAT302N potentiostat equipped with a FRA32M frequency response analyzer module.

Lastly, the output gas was examined through a gas chromatography-mass spectrometry analysis, through a Thermo Scientific FOCUS GC-ISQ Single Quadrupole MS and the H_2 production efficiency was calculated (Sarno et al., 2019b).

2.2.3 Results and discussion for NiRuIr_G

2.2.3.1 Morphological characterization

TEM images, in Figure 34, show the existence of nanoparticles with a uniform size anchored on few-layer graphene. The nanoparticles have an average diameter of 8 nm with a standard deviation of 1.8 nm. Energy dispersive spectroscopy (EDS) was also carried out, showing an Ir/Ru/Ni atomic ratio of 3.2:3.0:3.1, which is in good agreement with the percentages of metal precursors adopted for the synthesis. Furthermore, the EDX maps of the metals are reported. The maps of Ir, Ru and Ni are superimposable, which suggests a homogeneous distribution of the three metals in the nanostructure and, therefore, the trimetallic alloy nature of the sample.

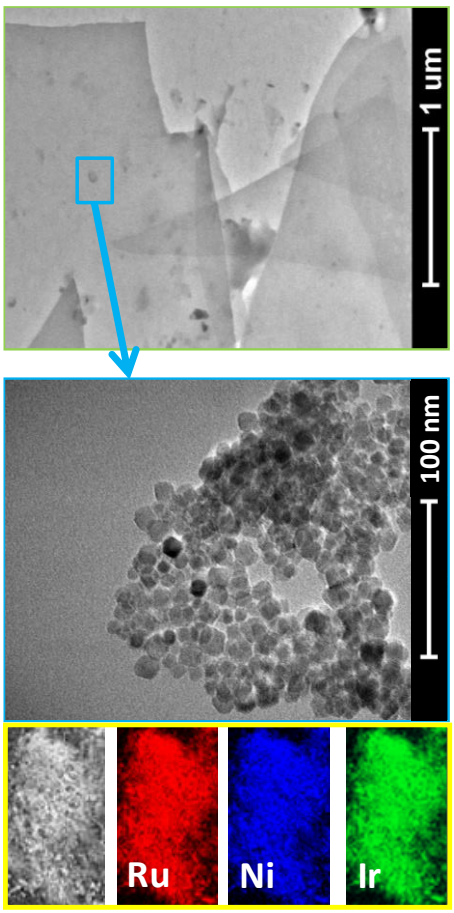

Figure 34. *TEM images of the NiRuIr_G nanocomposite and corresponding EDX map*

In addition, FESEM images of the synthesized sample are reported in Figure 35, showing the existence of a three-dimensional network of graphene flakes strictly connected to each other.

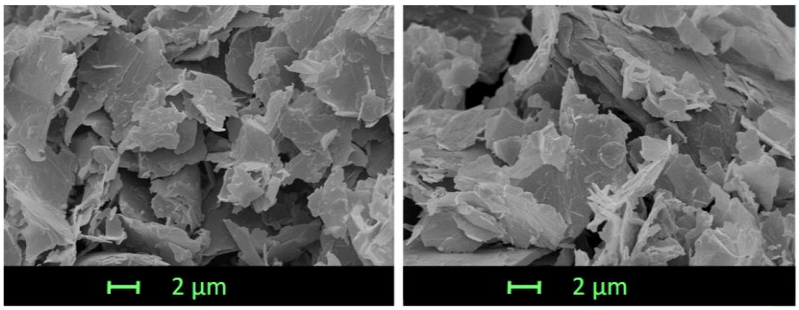

Figure 35. *SEM images of the NiRuIr_G nanocomposite*

2.2.3.2 X-ray diffraction analysis

Figure 36 shows that the diffraction peaks in the Ir-Ru-Ni nanoparticles match the (111), (200) and (220) typical planes of the fcc structure of iridium, even though they are slightly shifted to higher 2θ values. The absence of peaks related to the hcp structure of pure ruthenium and of the fcc structure of pure nickel, as well as the above-mentioned angle shift, likely due to a modification of the lattice constant caused by the incorporation of Ru and Ni atoms, suggests the existence of a trimetallic alloy (Park et al., 2002). Moreover, in the same pattern, the diffraction peak related to the (002) reflection of few-layer graphene can be detected at 2θ = 26.0°, suggesting the existence of a highly ordered crystal structure with an interlayer distance equals to 3.4 Å. More details regarding the nanosheets distribution have been previously reported (Guadagno et al., 2015; Lee et al., 2008).

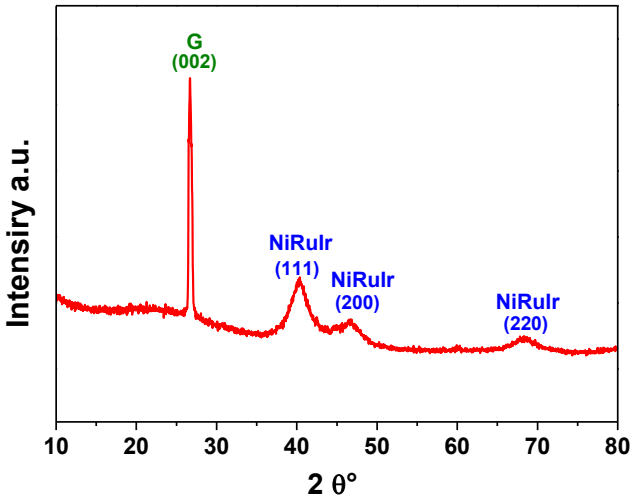

Figure 36. *XRD spectrum of the NiRuIr_G nanocomposite*

2.2.3.3 Electrochemical tests

Firstly, the HER activity of NiRuIr_G was tested in a 0.5 M H_2SO_4 solution before and after 11000 cycles per test (Figure 37a). As can be seen from the polarization curves at 20 mV/s, the sample exhibits a low overpotential whose value remains approximately the same one (0.06 V), even after 11000 cycles per test, hence suggesting the high stability of the synthesized material in the acidic medium. In Figure 37b, the corresponding Tafel plot is reported and a very low Tafel slope of 28 mV/dec was recorded, suggesting that the reaction proceeds through the Volmer-Tafel mechanism (Li et al., 2011).

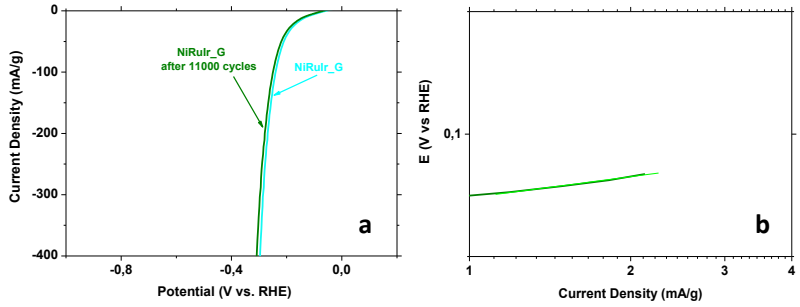

Figure 37. (*a) Polarization curves before and after 11000 cycles and (b) Tafel plot for NiRuIr_G recorded at 20 mV/sec in a 0.5 M H_2SO_4 electrolyte*

In the view of a development towards a more sustainable process, as also previously cited, acid electrolyte-based solutions must be replaced with a seawater solution. Therefore, the electro-catalytic behavior towards HER of NiRuIr_G in a neutral KCl aqueous solution was tested, as the first step towards this transition. Polarization curves, before and even after 11000 cycles in a single test, and the corresponding Tafel plot in Figures 38a and b show an overpotential of 0.10 V, almost comparable with the one obtained with an H_2SO_4-based electrolyte, a Tafel slope of 72 mV/dec, which suggests that the electrochemical hydrogen production proceeds fast also under these conditions, and remarkable stability. HER onset potential in alkaline solutions was also evaluated and it resulted higher than the one recorded in acid medium, proving the higher efficiency of the cell in the latter environment and, at the same time, the necessity to substitute also alkaline electrolyte-based solutions (Figure 38a, inset).

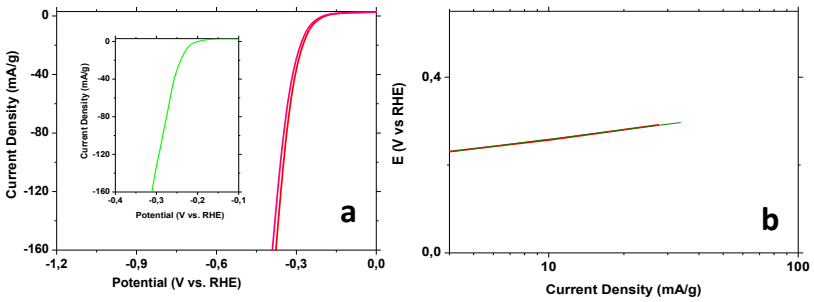

Figure 38. *(a) Polarization curves for NiRuIr_G before and after 11000 cycles recorded at 20 mV/sec in a KCl aqueous electrolyte. In the inset, polarization curve for NiRuIr_G recorded at 20 mV/sec in a KOH aqueous electrolyte. (b) Tafel plot of NiRuIr_G n recorded at 20 mV/s in a KCl aqueous electrolyte*

However, since a neutral solution of a single salt cannot be found in a real environment, the HER behavior of the synthesized sample was also tested adopting a real seawater solution as an electrolyte. Figures 39a and b show the polarization curve and the corresponding Tafel plot for the NiRuIr_G catalyst, evidencing an increased performance, likely due to the higher number of dispersed electrolytes.

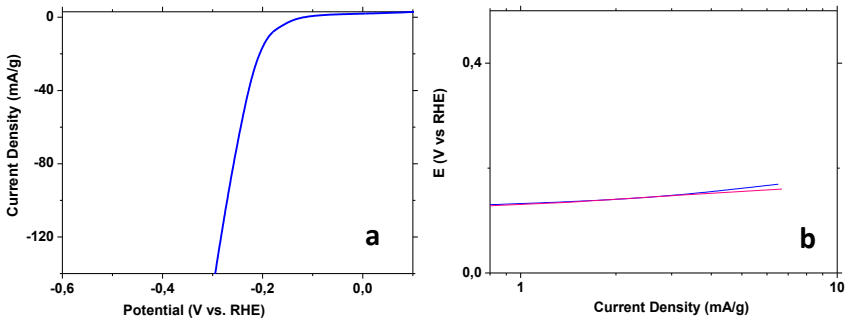

Figure 39. *(a) Polarization curve and (b) Tafel plot for NiRuIr_G recorded at 20 mV/sec in real seawater*

Figure 40 shows that NiRuIr_G roughly remains at an identical overpotential level at different sweep voltammetry cycles from the first one till the 250th one, which indicates the high stability of the sample in real seawater as well.

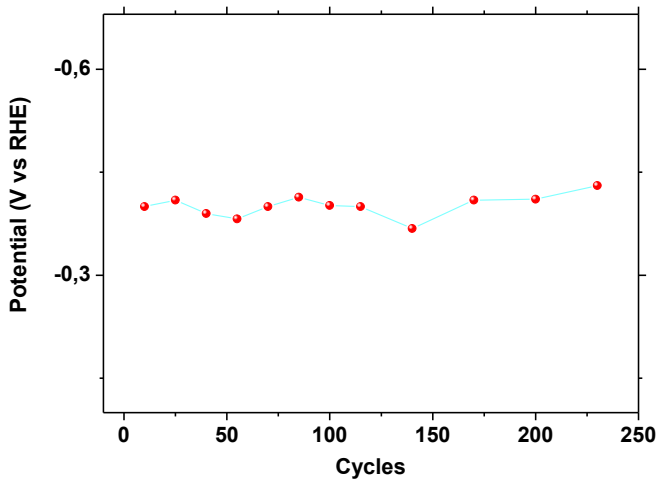

Figure 40. *Potential of NiRuIr_G nanohybrid in real seawater as a function of different cycles*

The stability of the sample in real seawater is confirmed also by the chronoamperometric measurement reported in Figure 41a. At a constant potential of 0.23 V, the corresponding current density of 40 mA/g was recorded and only a 10% current loss was recorded within 200 hours of test. The small decline can be attributed to slight corrosion of the alloy due to the Cl_2 released in seawater from the reduction of Cl^- ions at the anode, which, however, does not involve iridium, since the latter one is the less prone to be corroded by Cl_2 when compared with Ni and Ru.

Moreover, the inset shows the X-ray diffraction profile of the catalyst after 200 hours of usage: only a small shift of the relevant peaks was observed as a result of the relative enrichment of iridium in the alloy due to the slight corrosion of the other two metals by the generated Cl_2. In Figure 41b, the hydrogen production and the HER efficiency under potentiostatic electrolysis of NiRuIr_G are reported, highlighting the effectiveness of the catalyst. In particular, the amount of hydrogen produced using the nanohybrid in the real seawater solution was evaluated. The micromoles of hydrogen generated during the catalytic process were detected through gas chromatography-mass spectrometry and reported in dots. The theoretical data were, instead, obtained when considering the number of charges passing through the system (reported in the straight line) and these data are in good agreement with the experimental ones, which proves a remarkable H_2 production efficiency. Furthermore, it can be stated that the registered H_2 concentration after 120 min is comparable and, rather, even slightly higher when compared with the literature (Gao et al., 2015).

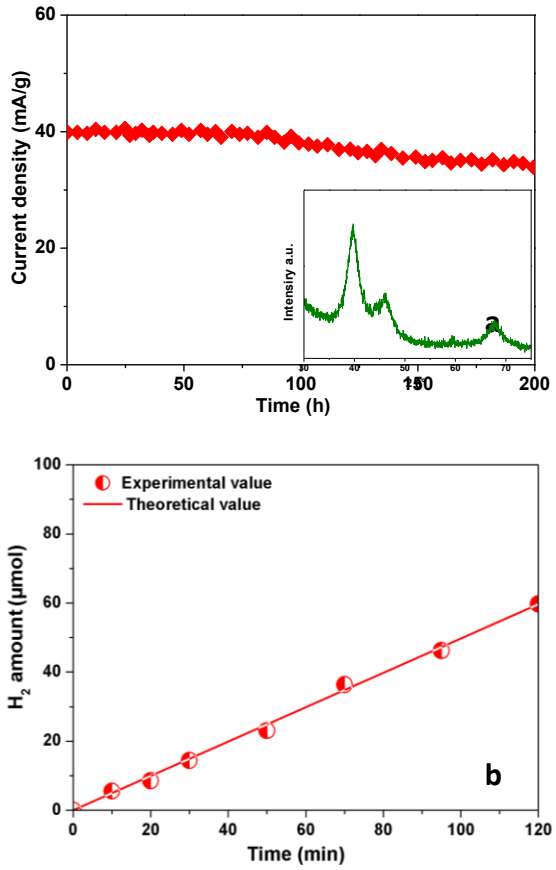

Figure 41. *(a) Current-time curve for the NiRuIr_G nanohybrid in real seawater. In the inset, the XRD profile of NiRuIr_G after 200 h of electrolysis; (b) hydrogen production efficiency for HER under potentiostatic electrolysis*

To summarize, the excellent performance of the NiRuIr_G nanocatalyst can be ascribed to intrinsic characteristics of its components, to synergistic alloying effects and, eventually, to the role of the graphene support. In particular, the main reasons for the improved performance are:

1. The choice of iridium, which is at the top of Trasatti's volcano plot, guarantees a high activity towards hydrogen evolution and gives the major contribution to the stability of the alloy both in acid and seawater environment, along with ruthenium.
2. The different work functions between metals, which induce the accumulation of electrons on the Ir surface, hence further increasing

(i) the catalyst activity, through strong interactions with H^+ ions (Li H. et al., 2016; Kuang et al., 2019), and (ii) the catalyst stability, due to the repulsion of Cl^- ions caused by the highly negatively charged iridium surface.

3. The increased anti-corrosion properties, which can be ascribed to competitive dissolution reactions between the different components of the alloy with Cl_2 dispersed in seawater, as previously observed in (Kuang et al., 2019). In particular, dissolution of the three metals in presence of Cl^- is thermodynamically spontaneous (which means ΔG values are strongly negative), but for Ir the absolute value of ΔG is much smaller.
4. The stability of the trimetallic alloy-based nanoparticles induced by the highly conductive graphene carpet, decreasing charge-transfer resistance at the catalyst/electrolyte interface and increasing electrochemical conductivity. It can be also imagined the role of graphene in helping catalysis, due to enhanced H^+ adsorption, and in protecting the catalyst from poisoning (Ma et al., 2017).

2.2.4 Results and discussion for RuOs_G

2.2.4.1 Morphological characterization

In Figure 42a, a SEM image of the physical exfoliated graphite (G), consisting of a few layers of graphene, is reported. SEM images of the prepared sample are instead reported in Figures 42b, c and d, which show the presence of a three-dimensional network of microflakes strictly connected to each other, which are even more fragmented after the synthesis. Furthermore, a hierarchical structure due to the co-presence of pores of different sizes can be also detected. In particular, the mesopores, crucial for providing ion diffusion channels and charges transfer, are more visible in the sample images after synthesis. Additional macropores for electrode wettability can be also seen.

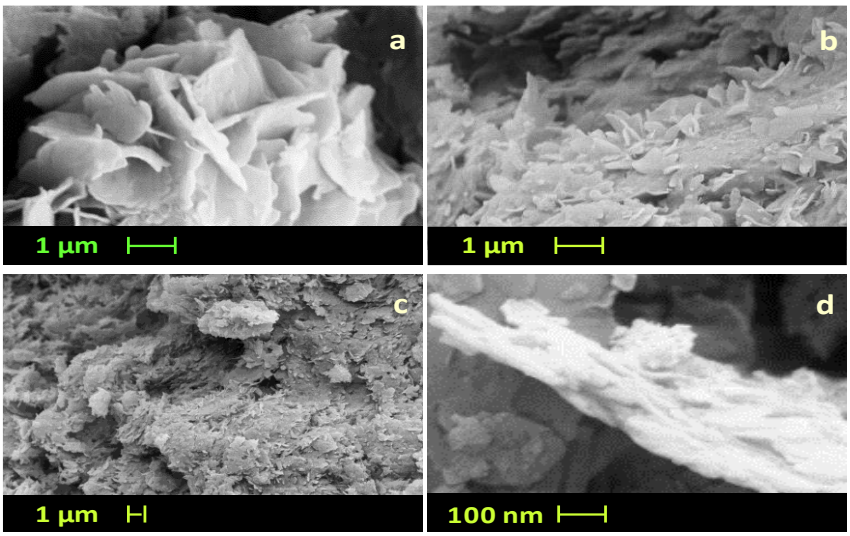

Figure 42. *SEM images of: (a) few-layer graphene (G); and (b), (c) and (d), of RuOs-G*

Figure 43 reports the TEM analysis of the synthesized sample. In Figures 43a and b, TEM images at low magnification (scale bars: 50 and 10 nm respectively) show that the rough areas of the graphene flakes are covered with nanoparticles having an average diameter of 10 nm, although smaller nanoparticles can also be observed, with a diameter up to 2-3 nm. Graphene flakes have a size of a few micrometers. The TEM image at high magnification in Figure 43c confirmed the formation of nanoparticles consisting of Ru and Os dioxides with metallic inclusions, in fact:

I. the yellow parallel lines show the typical interplanar distance of dioxides crystal lattices equal to about 0.259 nm.
II. the green parallel lines show the typical interplanar spacing of Ru crystal lattice equal to 0.247 nm.

Energy dispersive spectroscopy (EDS) was performed to analyze the composition of the nanostructure. The following atomic ratios were evaluated: 1.02:1.10 for Ru /Os and 10.09:1.13 for G /(Ru + Os).

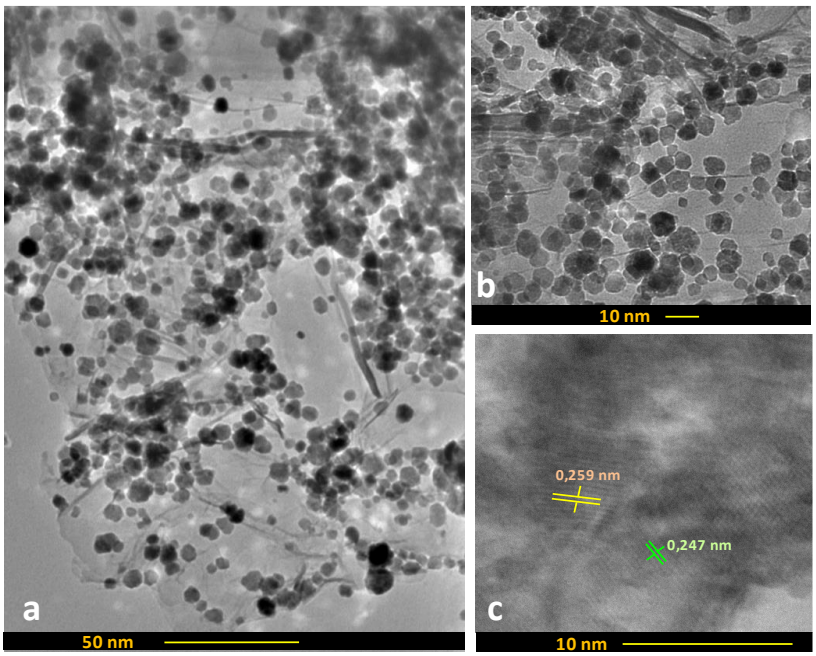

Figure 43. *TEM images of RuOs-G with scale bars of (a) 50 nm and (b) 10 nm. In (c) high-resolution TEM images of the same sample, evidencing interplanar distances of dioxide and Ru lattices*

2.2.4.2 X-ray diffraction analysis

The X-ray diffraction pattern of the synthesized sample is shown in Figure 44, evidencing the existence of a quaternary nanostructure comprising ruthenium and osmium and the corresponding oxides. The peaks broadness is likely due to the low temperatures of synthesis and the nano-size of the product. The highest detectable diffraction peaks can be attributed to the presence of the tetragonal lattice of both ruthenium and osmium oxide, with the (101) planes at ~34.46° 2θ, the (200) planes at ~41.91° 2θ and the (211) planes at ~54.11° 2θ (JCPDS 43-1027 and JCPDS 43-1044) (Yen et al., 2004). The presence of metallic Ru is evidenced by three diffraction peaks (indicated in magenta in the patter) corresponding to the major planes of the metal hexagonal lattice (JCPDS 06-0663). Furthermore, metallic Os shows also detectable peaks corresponding to the crystalline planes of its hexagonal lattice (JCPDS 06-0662) (Ede et al., 2014).

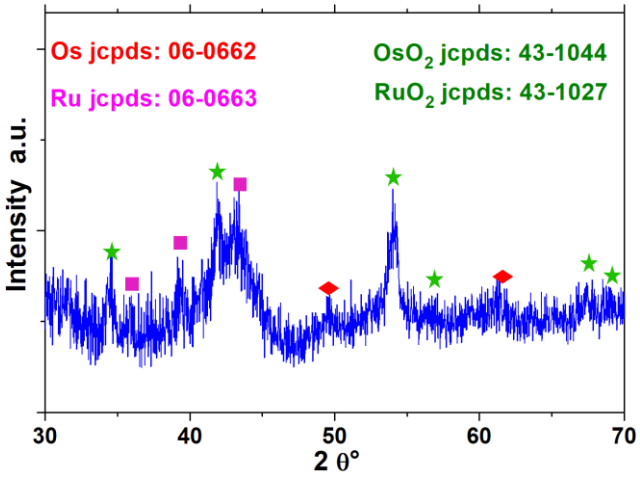

Figure 44. *XRD spectrum of RuOs_G*

2.2.4.3 Electrochemical tests

In order to investigate the electrocatalytic activity towards HER of the synthesized nanomaterial, the polarization curves of RuOs_G deposited on a SPE were firstly obtained in a 0.5 M H_2SO_4 solution (Figure 45). The RuOs_G electrocatalytic behavior proved to be excellent, also when compared with Pt nanoparticles. In particular, RuOs_G showed a negligible overpotential for HER (0.02 V *vs.RHE*) with fast current growth at decreasing voltages.

Moreover, RuOs_G recorded a nearly 100% Faradaic yield during HER in 0.5 M H_2SO_4, as revealed by the fact that the experimentally detected H_2 amount is very close to the theoretical H_2 amount (which was calculated based on a quantitative Faradaic yield from current density).

As mentioned above, oceans are huge reservoirs of hydrogen atoms. Extracting the hydrogen atoms from the ocean and converting them directly into a form of H_2 fuel requires many technological advances, one of which is the development of efficient water splitting catalysts operating well in seawater. However, it is challenging to find such catalysts because there are hundreds of different impurities in the unpurified seawater, which might lead to catalyst poisoning (Gao et al., 2015; Zou et al., 2012). In view of the high efficiency and excellent stability of RuOs_G recorded in acid medium, its catalytic performance was directly investigated using real seawater as an electrolyte as well. As shown in the same Figure 45, RuOs_G still

maintained high catalytic activity towards HER in real seawater. Rather, the performance of the synthesized nanostructure is even better than the one of Pt. Indeed, the catalytic current density reached 5 mA/ cm^2 at an overpotential of less than 500 mV, which is much less than the value required for Pt NPs-based electrodes. What is more, the overpotential of RuOs_G in seawater is 0.06 V *vs.RHE*, while Pt recorded an overpotential of 0.16 V *vs.RHE* in the same electrolyte environment.

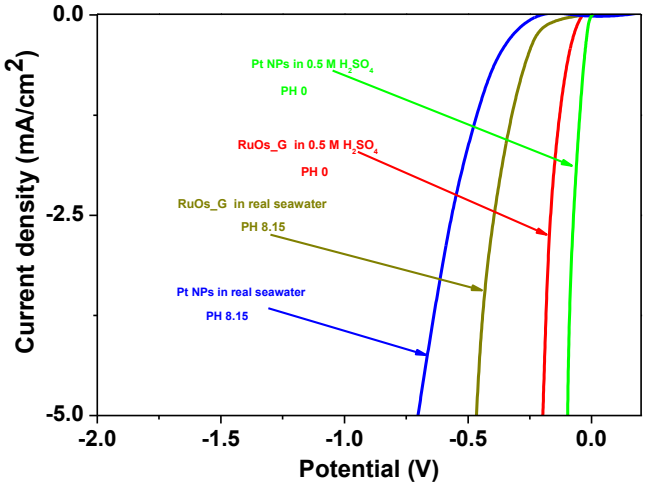

Figure 45. *Polarization curves of RuOs_G deposited on a DRP-110 SPE in 0.5 M H_2SO_4 solution and real seawater at a scan rate of 20 mV/sec*

Figure 46 shows the Tafel plots for RuOs_G recorded at pH 0 (0.5 M H_2SO_4) and pH 8.15 (real seawater). Because the linear portions of the Tafel plots are fitted through the Tafel equation, the corresponding Tafel slopes in 0.5 M H_2SO_4 are calculated to be 30 and around 28 mV/decade (iR-corrected) for Pt NPs and RuOs_G, respectively. This result implies that the HER mechanisms are similar on both catalysts, onto which HER proceeds through the faster Volmer-Tafel reaction pathway (Li et al., 2012).

Moreover, the larger Tafel slopes recorded in real seawater (i.e. 79 and 100 mV/dec for RuOs-G and PtNPs respectively) suggest that the electrochemical adsorption of hydrogen atoms would possibly be the prominent rate-limiting step for the HER.

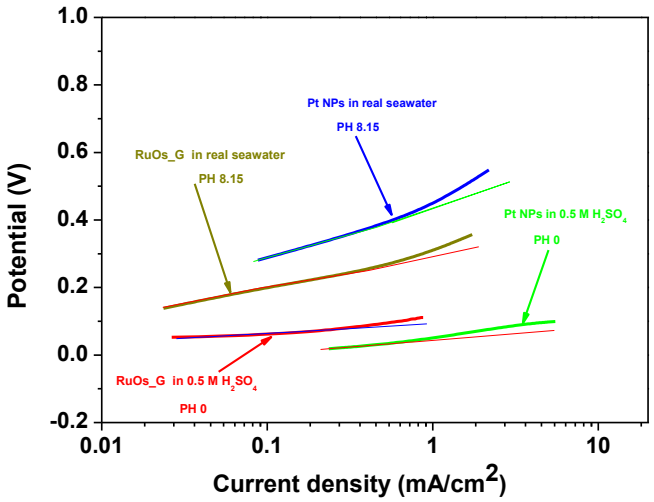

Figure 46. *Tafel plot for Pt NPs and RuOs_G in 0.5 M H_2SO_4 and real seawater*

The stability of RuOs_G in HER was examined by continuously monitoring the cathodic current at η = 420 mV for several hours (Figure 47), and the result showed that there is no loss of electrocatalytic activity after 24 hours. The high durability of RuOs_G can be attributed to the excellent tolerance of nanocarbon materials toward the impurities in seawater and the use of very stable and strong metals. In view of the excellent results, RuOs_G is very promising to be directly used in seawater for generating H_2, avoiding the cost of seawater desalination and purification.

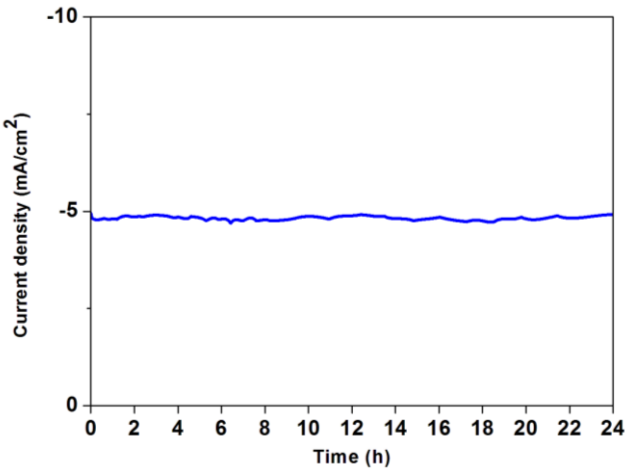

Figure 47. *Current-time curve for the RuOs_G catalyst in real seawater*

The strong proton absorption capacity of the graphene support effectively promoted the HER performance and, simultaneously, protected the catalyst from etching, agglomeration and poisoning in seawater. Moreover, the Ru and Os performance was improved by junctions and interactions with oxides, opening new perspectives for the development of innovative, durable and high-performance electrodes for the usage of seawater in H_2 generation

2.2.5 Conclusion: comparison with literature

Eventually, for comparison, the HER activity parameters, Tafel slopes and overpotentials, as well as the stability behavior of the most performing electrocatalysts in real seawater were reported in Table 2, along with the two synthesized catalysts. It is worth noticing that platinum performance is not remarkable in this type of electrolytic environment. Indeed, although being a benchmark catalyst in acid electrolytes, it can be easily poisoned due to the high presence of seawater impurities. On the other hand, both the synthesized catalysts clearly exhibited onset potentials of an order of magnitude lower than the other catalysts, as well as enhanced long-term stability in the seawater environment. In particular, the catalysts are capable to avoid prompt deactivation during HER in seawater owing to the presence of robust metals in their formulation, the choice of adopting graphene as support as well as the synergy between metals in protecting the more catalytically active portion from corrosion.

Table 2. *Comparison of the HER performance in real seawater between RuOs_G, NiRuIr_G and the most performing electrocatalysts reported in the literature*

Catalyst	Tafel slope [mV/dec]	Overpotential [V]	Stability	Ref.
Ni-Mo(1)_11 Mo/Nif	105	~0.152 (*vs. Ag/AgC*l)	-	Golgovici et al., 2018
Co,N-codoped CNT	~159 (buffer solution ph7)	~0.5 (*vs. RHE*)	No significant current losses within 10h	Gao et al., 2015
CoMoP@C	~140 (buffer solution ph7)	~0.3 (*vs. RHE*)	No significant current losses within 10h	Ma et al., 2017
RuCo/Ti	107	0.253 (*vs. RHE*)	30% of current loss over 12 h	Niu et al, 2016
RuCoMo/Ti	140	0.354 (*vs. RHE*)	No significant current losses within 12 h	Niu et al, 2016

Ni-Fe-C	-	~0.76 (*vs. Hg/HgO*)	-	Song et al., 2010
MoS_2 QD areogel	-	~0.25 (*vs. RHE)*	At 80 mA/g, potential level is constant for 150 cycles	Chen et al. 2019
Commercial Pt	-	Negligible (*vs. RHE*)	At 80 mA/g, potential increases from 0.6 V to over 0.8 V within 150 cycles	Chen et al. 2019
Pt NPs	45.8	~0.23 (*vs. RHE*)	~8% of current loss over 13.9 h	Li H. et al., 2016
PtRuMo/Ti	44	~0.1 (*vs. RHE*)	~15% of current loss over 172 h	Li H. et al., 2016
RuOs_G	79	~0.06 (*v.s RHE*)	No current loss over 24 h	**This work**
NiRuIr_G	48	~0.08 (*vs. RHE*)	Potential level is constant for 250 cycles; ~10% of current loss over 200 h	**This work**

Chapter 3:
State of the art on single atom catalysts (SACs) for the electro-reduction of CO_2 to both CO and syngas

3.1 Introduction

Since the last century, the global average atmospheric concentration of CO_2 has been dramatically increasing at an exponential rate, reaching, at present, over 417 ppm, which is about 50 % higher than the level at the beginning of the Industrial Revolution. The dramatic increase of CO_2 in the atmosphere is the major consequence of the growth in the consumption of fossil resources. Among the emitted gases, CO_2 is one of the most dangerous, being the main responsible for the greenhouse effect and amounting to over 80% of the whole emissions (Basu et al., 2020; Davis et al., 2010a; Dincer et al., 2015; Davis et al., 2010b). Since the dependence on non-renewable sources is still indispensable, it is essential to overcome the problem related to the high amount of CO_2 in the atmosphere. Currently, two are the major approaches to overcome it (Li et al., 2013). The first one consists of the capture and geological storage of CO_2 in underground reservoirs. However, the feasibility of this approach is highly hampered by safety, space, and cost reasons. The second technology is related to the valorization of CO_2 into low-molecular-weight chemicals or fuels (Najafabadi et al., 2013; Hod et al.; 2015). The main methods for the chemical conversion of CO_2 are four: thermochemical, electrochemical, photoelectrochemical, and photocatalytic. Among them, the electrochemical reduction of carbon dioxide can bring some advantages over the other

methods (Centi et al., 2009; Benson et al., 2009). Firstly, unlike the thermochemical method, the electro-reduction of CO_2 (defined in the literature as CO_2RR) can occur under mild conditions such as atmospheric pressure and room temperature. Secondly, unlike the photocatalytic method, which also represents a very promising process since it can be carried out under mild conditions and with sunlight as radiation source, the electrochemical method does not require direct exploitation of solar energy (which is often limited by the semiconductor band-gap) and does not suffer from the low efficiency due to the high recombination rate of the photogenerated charges. Furthermore, this process is the most sustainable since the electricity needed can be supplied through a renewable resource, without generating further CO_2, and because the co-reactant is water, which is an abundantly, economically and easily available natural resource. In addition, the process can be accurately controlled by varying, for instance, the electrode potential, hence higher conversion efficiencies can be more easily obtained. Moreover, the electrochemical system is modular, compact and can be easily scaled up. It is clear, therefore, that being able to efficiently turn CO_2 into value-added molecules is by far one of the most valuable, effective and feasible methods (Lu et al., 2016). A scheme of the circular economy involving CO_2 capture and CO_2 electro-reduction to chemicals is represented in Figure 48. As a consequence of the above-mentioned facts, the electro-reduction of carbon dioxide to value-added molecules has been extensively explored in many studies. Although this route is highly promising, several challenges have still to be faced before its large-scale applicability becomes a certainty. Apart from the high stability of the CO_2 molecule at ambient conditions (Najafabadi et al., 2013). The major limitation of the process still persisting is the low performance of the electrocatalysts so far adopted, in particular their low catalytic activity, selectivity and stability over time (Garg et al., 2020).

As shown in Table 3, carbon dioxide can be reduced in an aqueous solution to produce carbon monoxide, formic acid, methane or the other listed chemicals by applying a certain theoretical thermodynamic cell potential (Tripkovic et al., 2013; Szkaradek et al., 2018). Among all the chemicals obtained from the CO_2 electro-reduction, carbon monoxide is the most likely and easiest to be produced from the thermodynamic point of view, since only two electrons are involved in the reaction, even though an additional potential for its formation is always required and it mainly depends on the type of catalyst chosen for the reaction. As shown in eq. (4), the rate-limiting step of the reaction is the formation of the CO_2^{-*} radical. After its formation, on metals such as Au and Ag, an H^+ proton attacks the oxygen-end of the radical to form a COOH* intermediate (* indicates the adsorption site) which adsorbs on the catalyst surface through its C atom, in eq. (5). The addition of another proton and electron to COOH* leads to CO* intermediate, as shown in eq. (6), which can desorb (see eq. (7)) unless its

binding strength to the catalyst surface is too high (Qiao et al., 2014; Zhu D. D. et al., 2016).

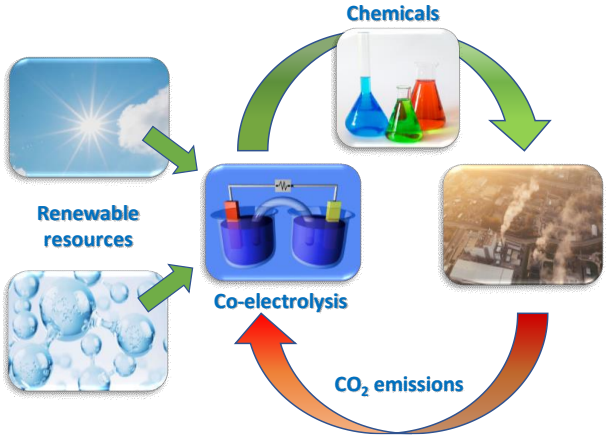

Figure 48. *Scheme of the electrochemical CO_2 capture and conversion to chemicals as a carbon neutral process*

Table 3. *Standard reduction potential (E°) at 25 °C, 1 bar and pH=7 for the CO_2 reaction reductions to several chemicals*

Chemical Reaction	**E° (*V vs.RHE*)**
$CO_2 + 2H^+ + 2e^- \rightarrow CO + H_2O$	-0.11
$CO_2 + 2H^+ + 2e^- \rightarrow HCOOH$	-0.25
$CO_2 + 4H^+ + 4e^- \rightarrow H_2CO + H_2O$	-0.07
$CO_2 + 6H^+ + 6e^- \rightarrow CH_3OH + H_2O$	0.02
$CO_2 + 8H^+ + 8e^- \rightarrow CH_4 + 2H_2O$	0.17
$CO_2 + 12H^+ + 12e^- \rightarrow C_2H_4 + 4H_2O$	0.06

$$CO_2 + e^- \rightarrow CO_2^{-*} \quad (4)$$

$$CO_2^{-*} + H^+ \rightarrow COOH^* \quad (5)$$

$$COOH^* + H^+ + e^- \rightarrow CO^* \quad (6)$$

$$CO^* \rightarrow CO \quad (7)$$

On the other hand, occurring at approximately the same theoretical reduction potential, the hydrogen evolution reaction (HER) is in inevitable competition with the CO_2RR, hence lowering the selectivity to CO and other chemical products. Many past studies have, indeed, considered the HER as a parasitic reaction to be suppressed. However, an interesting alternative consists of not suppressing the HER but favoring the electrochemical co-production of CO and H_2 by obtaining syngas. Indeed, around 1.7×10^8 tons of syngas are globally produced every year primarily through steam methane reforming and coal gasification, with a global market that is expected to grow till 72.4 billion US dollars by 2022 at a compound annual growth rate of 9.1% (Jouny et al., 2018; BCC Publishing, 2018). Depending on its CO/H_2 ratio, a synthesis gas could be used as important feedstock to several industrial processes, such as methanol synthesis (when the CO/H_2 ratio is 0.5) and Fischer–Tropsch synthesis (for instance, when the CO/H_2 ratio is equal or even less than 0.5) (Sheng et al., 2017; Ross et al., 2017). Although being cost-effective, it is worth noticing that current industrial processes for syngas generation are fossil-fuels dependent, hence not "optimized" from an environmental point of view. In addition, the electrochemical co-production of CO and H_2 can lead to syngas with a tunable CO/H_2 ratio, hence ensuring the integration of a sustainable process into production lines of different chemicals. In order to produce syngas, the CO_2RR must be selective towards CO. Nanostructured catalysts consisting of noble metals, such as Au and Ag nanoparticles (NPs), have proved to be highly active and selective towards the CO production from the co-electrolysis of CO_2 and H_2O, leading to syngas with a high CO/H_2 ratio (Verma et al., 2016; Chen et al., 2012; Zhu et al., 2013). However, the high costs and/or the low natural availability of these noble metals significantly hinder their application on an industrial scale. Gold-based catalysts are clearly highly expensive (gold cost is around 48 US dollars per gram). As for silver, although being less expensive than Au (its current price is about 0.41 US dollars per gram), it is a finite resource whose availability is expected to decrease in the years to come. In addition, high electrocatalytic activity on these metals corresponds to still high overpotentials, since both Au and Ag show a low COOH* intermediate bond strength along with a low CO adsorption strength in virtue of the linear relationship between the adsorption energies of the CO_2 intermediates on transition metal surfaces (Hansen et al., 2013). What is more, both Au-and Ag-based electrocatalysts are extremely selective for CO generation at low overpotentials (instead, at extremely high overpotentials, HER become more favored than CO_2RR on these metals). This high CO selectivity at low overpotential can become a drawback when aiming at producing syngas with a more tunable CO/H_2 ratio, for instance, with a CO/H_2 ratio lower than 70-60 %.

In order to overcome these issues, i.e. improved CO_2 reduction and/or co-electrolysis of CO_2 and H_2O, an effective alternative to these noble metal-based nanoparticles is represented by metal-based single atom catalysts (SACs). Recently, it has been demonstrated that by further reducing the size of nanoparticles to the sub-nanometer range, nanocluster catalysts can be obtained (Doherty et al., 2020). In virtue of the strong quantum confinement effects at this size, these catalysts exhibit unique properties such as several valence states and discrete electronic configurations, which strongly depend on the number of atoms constituting the cluster. These properties, along with the increased number of under-coordinated metal atoms, i.e. the increased amount of active catalytic sites, make nanocluster catalysts highly active towards a wide range of chemical reactions such as CO_2RR and HER (Wang A. et al., 2018; Kwak et al., 2009; Zhu et al., 2017; Qiao et al., 2011). The ideal case, corresponding to the minimum size and the maximum metal utilization of the nanocluster is represented by the metal single atom: at this size, individual metal atoms become accessible and, therefore, active for catalysis (Yang et al., 2013; Speck et al., 2021). More in general, in order to guarantee high dispersion and to avoid agglomeration, nanoparticle catalysts are typically dispersed on a support surface. Furthermore, the interaction between nanoparticles and support can lead to a modification of the electronic environment of the metal particles, hence increasing the interactions between catalyst surface and reaction intermediates and changing the catalytic activity of the former (Cordón et al., 2017). It has been observed that when the size of the nanoparticles has been reduced till the atomic range, these metal-support interactions will be maximized, which means the formation of novel catalytic active sites, creation of new reaction pathways and, eventually, raise of the catalytic performance can occur (Li et al., 2003; Valden et al., 1998). Consequently, the catalytic activity, selectivity, and stability of nanostructured catalysts and, above all, of SACs can be controlled by choosing the right supports and by tuning the coordination environment.

The synthesis of stable platinum single atoms efficiently supported on the surfaces of iron oxide nanocrystallites has been successfully performed by Qiao et al. (2011). Since then, SACs have drawn increasing attention due to their high catalytic performance with a high reduction in metal loading compared with their nanoparticle counterparts. SACs have been adopted for hydrogen evolution reaction (HER), oxygen reduction reaction (ORR), CO oxidation and organic synthesis (Lecuyer et al., 1991; Han et al., 2017). However, it is only recently, with the development of more specific characterization techniques such as high-angle annular dark-field scanning transmission electron microscopy (HAADF-STEM), enabling to obtain images with atomic resolution, and X-ray absorption fine structure spectroscopy (XAFS), providing local atomic structural information

(oxidation state, coordination number, bond length, atomic species etc.), that SACs have been started to be considered for the CO_2RR catalysis and, above all, for the production of syngas. Therefore, the following chapter will aim to answer the necessity of an extended and exhaustive analysis of the metal single atom catalysts thus far adopted for the electro-reduction of carbon dioxide in aqueous solutions to allow CO_2RR reactions. Moreover, particular attention will be paid to the objective to form syngas with a highly tunable CO/H_2 ratio. Furthermore, the advantages of SACs over their noble metal-based NPs counterparts will be identified, along with future perspectives also in the view of rapid scale-up. In Figure 49 the structure of the chapter is reported.

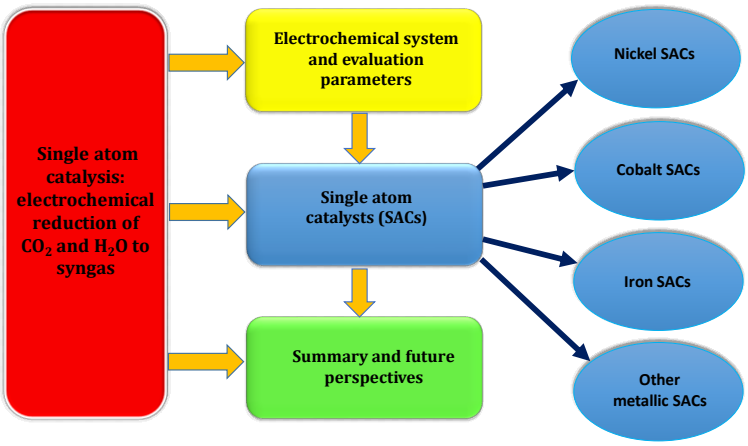

Figure 49. *The outline of Chapter 3*

3.2 Electrochemical system and evaluation parameters

3.2.1 Electrochemical measurement system

A typical electrochemical measurement system for evaluating the catalyst performance towards HER and CO_2RR to CO can be considered as made up of three main components:

1) An electrochemical workstation, which provides electric power to the cell and records the corresponding electrochemical parameters such as onset potential and current density.

2) An electrochemical reaction cell, where the reduction of CO_2 and H_2O occurs. The most widely adopted electrochemical system is the so-called

batch-type, H-type cell (Tan et al., 2019), whose anodic and cathodic compartments are separated by an ionic membrane and in which the gas-phase chemicals diffuse to the electrode surface through an aqueous electrolyte (as shown in Figure 50). It is worth noticing that, when it comes to liquid electrolyte systems, the selectivity either towards CO or H_2 can also be achieved by changing the type of electrolyte. As can be seen from the majority of studies, the most adopted electrolyte for obtaining a high CO selectivity is $KHCO_3$, since CO_2 replenishment at the electrode is favored by it (Asset et al., 2019). On the other hand, the main limitation of an H-type configuration is that the mass transportation of gas species is rather low (Li Y. C. et al., 2016; Endrődi et al., 2017). In order to enhance mass transportation, continuous-flow reactors have recently been demonstrated as an effective solution. These flow cells can deliver reactants to the electrodes and remove products from them continuously, hence increasing the mass transport, and are typically divided into two main types: membrane reactors and microfluidic reactors (see Figure 51). The main feature of membrane reactors is an ion-exchange membrane separating the anodic and cathodic compartments, hence enabling an easier separation of the products and avoiding their re-oxidation. On the other hand, in microfluidic reactors, separation of the electrodes is guaranteed by a flowing electrolyte within a millimetric channel, which enables a better electrode wettability (Weekes et. al., 2018).

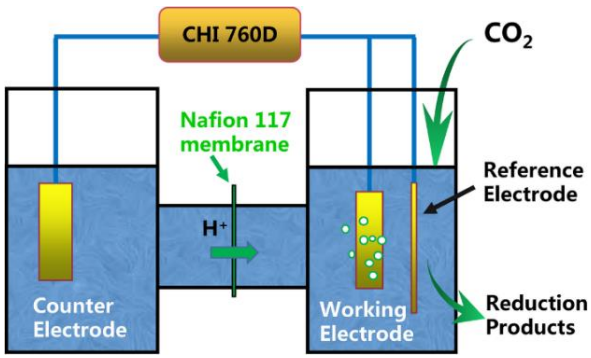

Figure 50. *A schematic representation of a typical H-cell for testing CO_2RR. Reprinted with permission from (Tan W., B. Cao, W. Xiao, M. Zhang, S. Wang, S. Xie, D. Xie, F. Cheng, Q. Guo and P. Liu (2019) Electrochemical Reduction of CO_2 on Hollow Cubic Cu_2O@Au Nanocomposites. Nanoscale Res. Lett., **14,** 63). Copyright (2021) Springer Nature*

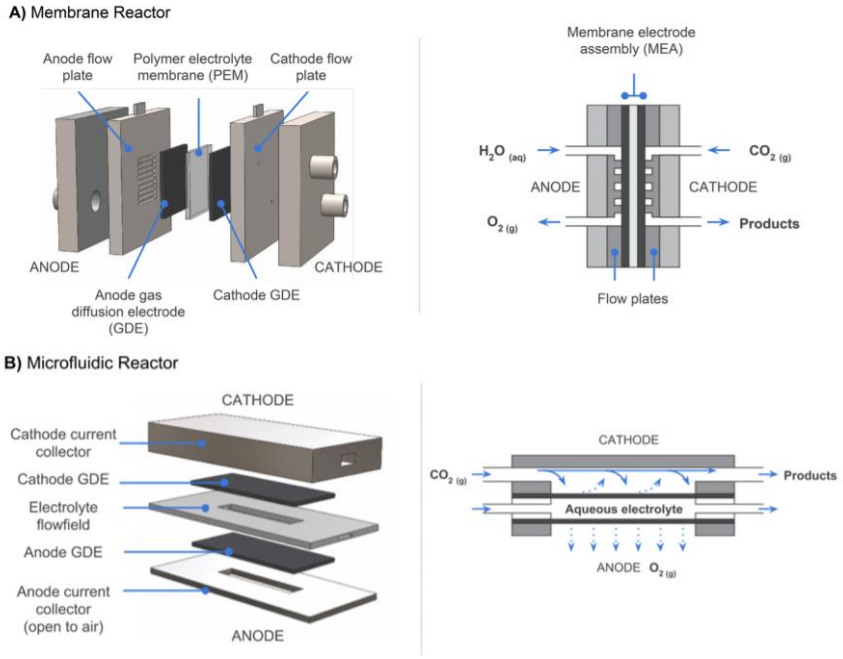

Figure 51. *Schematic representation of continuous-flow reactors for testing CO_2 electro-reduction. In detail, a) membrane-based reactor and b) microfluidic reactor. Reprinted with permission from (Weekes D. M., D. A. Salvatore, A. Reyes, A. Huang and C. P. Berlinguette (2018) Electrolytic CO_2 Reduction in a Flow Cell. Acc. Chem. Res., **4**, 910-918). Copyright (2021) American Chemical Society*

3) Online/outline gas chromatography (GC), which provides a quantitative analysis of the gaseous products, and nuclear magnetic resonance (NMR), typically used to analyze possible liquid products.

3.2.2 Evaluation parameters

Herein, a list of the most common parameters adopted for the evaluation of the catalyst performance towards CO_2RR and syngas production is reported:

1) Onset potential: defined as the applied potential at which electrochemical reaction begins to occur on the surface of the electrode. From this parameter derives the definition of overpotential of an electrochemical reaction, which is defined as the difference between the onset potential and the thermodynamic reduction potential of the reaction. The main causes for the overpotential are: (a) the high energy needed to activate the reaction, especially for the occurrence of reaction rate-limiting steps. For the CO production, they are represented by the electron transfer to

the CO_2 molecule in order to form the CO_2^{-*} radical; (b) mass transport resistances and; (c) ohmic losses due to the electrolyte and the electrode conductivity.

2) Current density: defined as the electric current per unit of surface or geometric area of the electrode. The higher the current density measured at a certain potential, the higher the reaction rate of the electrochemical reaction. Obviously, the most performing electrocatalyst must be able to generate a high current density (most precisely, a high partial current density related to the formation of the desired product, in this case, either CO or H_2) at a potential as close as possible to the standard reduction potential, which corresponds to an overpotential equals to zero.

3) Faradaic efficiency (FE): the parameter adopted to quantify the yield of a chemical produced through the electrochemical route with respect to all the produced species, and therefore the catalyst selectivity. FE is the ratio of the number of charges required to form a certain amount of desired product to the total charge over a specific time interval. The Faradaic efficiency for a specific product can be calculated as in eq. (8):

$$FE = \frac{F \cdot e \cdot mol}{j \cdot A \cdot t} \cdot 100\% \quad (8)$$

where F is the Faraday constant (96485.33 s·A/mol); e is the number of electrons involved in the reaction; mol is the number of moles of desired product; j is the current density (A/m^2); A is the active area of the electrode (m^2); and t is the reaction time (s). Ideally, the sum of the Faradaic efficiencies of all the generated species should be equal to 100%, to guarantee a Faradaic balance.

3.3 Single atom catalysis M-N-C catalysts for CO_2RR to CO and electrochemical production of syngas

In the following paragraphs, the SACs reported in the literature in the last few years were summarized with a particular focus on nickel, cobalt and iron-based SACs, as they are the most typically adopted metals. In particular, most of them were studied for the CO_2RR to CO, since only recently attention has been placed on taking advantage of both HER and CO_2RR to CO for producing syngas. All the catalysts were tested at ambient temperature and pressure, and in most of the studies, a $KHCO_3$ aqueous solution was adopted as the electrolyte. Table 4 summarizes the main electrochemical parameters and results from these SACs.

Table 4. *Evaluation parameters of the most recent metal SACs for the CO and syngas electro-production from CO_2 in aqueous electrolyte solution at ambient pressure and temperature*

Catalyst	Metal load. [wt% or at%]	Onset potential (*vs. RHE*) [V]	Cathodic potential (*vs. RHE*) [V]	Corr. max FE_{CO} [%]	Corr. total current density and max total current density [mA/cm^2]	Durability	CO/H_2	Ref.
N-C	-	~-0.50	-0.52	~91	0.47	-	-	Hu et al., 2018
Ni-N-C	Ni: 0.24-0.46 wt%	~-0.40	-0.67	93	3.90	No significant current loss within 12 hours of test at -0.67 V	-	Hu et al., 2018
Ni-N-C	Ni: 2.83 wt%	~-0.45	-0.75	~96	~10 (maximum ~25 at –0.95 V)	No significant current loss within 9,5 hours of test at −0.75 V	-	Pan F. et al., 2018b
Ni-N-Gr	Ni: 2.20 wt%	-0.50	-0.70	~90	~0.50 (maximum ~4 at -2.20 V)	No significant current loss within 5 hours of test at -0.65 V	-	Su et al., 2016
NiN-GS	-	-0.35	-0.82	93.20	~35 (maximum ~65 at -0.95 V) [values in mA/mg]	No significant current loss within ~20 hours of test at -0.70 V	-	Jiang et al., 2017
Ni-NG	Ni: 0.44 at%	-0.31	-0.62	95	11 (maximum ~28 at -0.90 V)	No significant current loss within~20 hours of test at -0.64 V (overpotential)	-	Jiang et al., 2018
SA-Ni/N-CS	Ni: ~1.08 wt%	~-0.40	-0.80	95.10	~9 (maximum ~32 at -1.20 V)	No significant current loss within~25 hours of test at -0.80 V	-	Yuan et al., 2020
Ni-N_4-C	Ni: 1.41 wt%	-0.40	-0.81	99	28.60 (maximum 36.20 at −0.91 V)	About 25% current loss within 30 hours of test at -0.81 V	-	Li et al., 2017

Ni SACs/N-C	Ni: 1.53 wt%	-0.57	-0.90	72	~10 (maximum 20 at -1.20 V)	No significant current loss within 60 hours of test at -1 V	-	Zhao et al., 2017
Ni-N-MEGO	Ni: 6.90 wt%	-0.29	-0.70	92.10	~17.50 (maximum ~25 at -0.76 V)	29.1% current loss within 21 hours of test at -0.55 V	-	Cheng et al., 2018a
NiSA-N-CNT	Ni: 20.7 wt%	-0.27	-0.70	91	- (maximum ~36 at –0.65 V)	12 % current loss within 12 hours of test	-	Cheng et al., 2018b
NiCoSA-N-CNT	Ni+Co: 13,20 wt%	-0.27	-0.70	~30	-	-	-	Yang H. B. et al., 2018
NiPtSA-N-CNT	-	-0.27	-0.70	~5	-	-	-	Yang H. B. et al., 2018
A-Ni-NSG	Ni: 2.80 wt%	~-0.15	-0.50	97	~1.40 (maximum ~110 at -1.10 V)	No significant current loss within 100 hours of test at -0.61 V	-	Yang H. B. et al., 2018
Ni-CTF	Ni: 0.14-0.17 at%	−0.48	-0.90	~95	~1 (maximum 4.50 at -1.20 V)	About 50% current loss within 3 hours of test at −0.65 V	-	Su et al., 2018
NiSAC/ NiNP CNRs	Ni: ~20 wt%	-0.40	-0.60÷-0.80	95.2/10	~13 ÷~27.5 in the range -0.60 V÷-0.80 V	No significant current loss within 8 hours of test	0.11÷19 by varying the Ni-N sites/ Ni NPs ratio from 0.20 to 1	Zhu W. et al., 2020
Ni/NCNTs-50	-	-0.32	-0.6÷-1	~100	~5÷~35 (maximum ~50 at -1.20 V)	No significant current loss within 20 hours of test	-	Hou et al., 2020
NiSA/PCFM (GDE cell, electrolyte flow cell)	Ni: 0.85 wt%	~-0.20	-1	~88	~180 (maximum ~360 at -1.35 V)	No significant current loss within 120 hours of test	-	Yang et al., 2020

NI-N-C (GDE, electrolyte flow cell)	Ni: 10.20 wt%	-	-0.70	~90	- (maximum ~700 at -2.20 V)	No significant CO FE loss within 20 hours of test at a J_{CO} of 200 mA/cm_2	-	Möller et al., 2019
Co-N_2	Co: 0.25 wt%	~-0.20	-0.68	95	~22.5 (maximum ~45 at -0.90 V)	No significant current loss within 60 hours at -0.63 V	-	Wang X. et al., 2018
Co-HNC	Co: 3.40 wt%	~-0.25	Above -0.80	~35	Above 10 (maximum ~25 at -1.40 V)	No significant current loss within 24 hours at -0.80 V and -1.40 V	It remains stable at 0.5 in the potential range -0.7 ÷ -1 V.	Song et al., 2018
Co-N_5/HNPCSs	Co: 3.54 wt%	-0.30	-0.79	99.40	~5 (maximum ~18 at -0.90 V)	No significant current loss within 10 hours of test	-	Pan Y. et al., 2018
Co-N-C	Co: 2.52 wt%	~-0.40	-0.67	~46	~6 (maximum ~ 18 at -0.88 V)	-	-	Pan F. et al., 2018b
Co@CoNC-900	Co: ~2 wt%	~-0.40	-0.80	~47	(maximum ~8 at -0.80 V)	No significant current loss within 12 hours of test at -0.05 V	4÷1 by varying potential range -0.3 V÷ -0.8 V at 900 °C anneal. T	Daiyan et al., 2020
CoNi-NC	Co: 1.2 wt%; Ni:1.2 wt%	-	-0.60	~55	~12 (maximum ~74 at -1 V)	No significant current loss within 20 minutes of test at -0.60 V	0.23÷ ~3.30 by varying potential in the range -1 V÷-0.5 V and Co/Ni precurs. ratio in the range 0.2÷5	He et al., 2020
CoSA-N-CNT	Co: 7.6 wt%	-0.27	-0.70	~20	-	-	-	Cheng et al., 2018b
CoFeSA-N-CNT	Co+Fe: 11.50	-0.27	-0.30	~30	-	-	-	Cheng et al.,

	wt%							2018b
Fe-N-G/bC	Fe: 7.67 wt%	~-0.40	-0.66	~95.80	~7 (maximum ~33 at -1.20 V)	No significant current loss within 12 hours of test at -0.66 V	-	Zhang C. et al., 2018
Fe/NG-750	Fe: 1.25 wt%	~-0.30	-0.57	~-80	~1 (maximum ~7.30 at -0.80 V)	No significant current loss within 10 hours of test at -0.60 V	-	Zhang H. et al., 2018
Fe–N/CNF-2	Fe: 0.33 wt%	~-0.27	-0.53	~95	~7 (maximum ~18 at -0.80 V)	No significant current loss within 24 hours of test at -0.53 V	-	Cheng et al., 2018c
Fe-N-C	Fe: 0.1 at%	-0.29	-0.58	93	~4.50 (maximum ~15 at -0.90 V)	No significant current loss within 20 hours of tests at -0.58 V	-	Pan F. et al., 2018a
C-AFC©ZIF-8	Fe: 1.47 wt%	-0.33	-0.43	93	~5 (maximum ~23 at -0.85 V)	The half-wave potential decreases by 20 mV after 10,000 cycles	-	Ye et al., 2017
Fe–N–C-0.5	Fe: 2.91 at%	~-0.30	-0.68	~98	~7 (maximum ~20 at -0.90 V)	No significant current loss within 55 minutes of test at -0.58 V, -0.63 V and -0.68 V	-	Wu et al., 2020
Fe-SA/NCS-700	Fe: 0.89 at%	-0.22	-0.45	87	~3 (maximum ~35 at -1.35 V)	No significant current loss within 10 hours of test at -0.45 V	-	Zhu Y. et al., 2020
Fe-N-C	Fe: 3 %wt	~-0.40	-0.60	74	~1.5 (maximum ~11 at -1.20 V)	No significant current loss within 12 hours of test at -0.60 V	0.25÷ ~3 by varying potential in the range -0.6 V÷-1.0 V at 950 °C carboniz. T	Zhao et al., 2020

Fe-N-C	Fe: 2.14 wt%	~-0.30	-0.49	~87	~ 0.2 (maximum ~18 at -0.88 V)	-	-	Pan F. et al., 2018b
$Fe_{0.5}$d	Fe: 1.50 wt%	-0.30	-0.60	91	4.5 (maximum ~19 at -0.90 V)	No significant current loss within 6 hours of test at -0.60 V	0.2÷4 by varying the Fe-N_4 active centers perc. from 0 to 100%	Huan et al.,2017
AD-Sn/N-C1000	Sn: 1 wt%	~-0.40	-0.60	91	~ 2.50 (maximum ~17.60 at -1 V)	No significant current loss within 25 minutes of test at -0.60 V	-	Zhao et al., 2018
ZnN_x/C	Zn: 0.10 wt %	−0.13	-0.43	95	~ 3 (maximum ~37.50 at -1.10 V)	No significant current loss within 75 hours of test at −0.43 V	-	Yang F. et al., 2018
Pd-NC	Pd: 2.95 wt%	-	-0.50	55	-	No significant current loss within 3.5 hours of test at −0.60 V	-	He et al., 2020b
Ag_2-G	-	-0.25	-0.70	93.40	11.87 (maximum 44.30 at -1 V)	No significant current loss within 36 hours of test at −0.70 V	--	Li et al**.,** 2020
Cr-N-C	Cr: 2.22 wt%	~-0.50	-0.85	~72	~5 (maximum ~ 13 at -1 V)	-	-	Pan F. et al., 2018b
Mn-N-C	Mn: 2.74 wt%	~-0.55	-0.59	~70	~0.20 (maximum ~7.50 at -0.95 V)	-	-	Pan F. et al., 2018b
Mn-C_3N_4/CNT	Mn: 0.17 wt%	~-0.30	-0.55	98.8	~15 (maximum ~38 at –0.90 V)	No significant current loss within 20 hours of test at −0.55 V	-	Feng et al., 2020
Ni/Fe-N-C	Ni: 0.97 %; Fe: 0.34 %	~-0.45	-0.70	98	9.50 (maximum 23.70 at -1 V)	No significant current loss within 33 hours of test at −0.70 V	-	Ren et al., 2019
Cu–N_4–NG	Cu: 4.7 wt%	~-0.40	-1.00	80.6	~5.40 (maximum	No significant	-	Xu et al.,

					~9 at -1.30 V)	current loss in the first hour of test at −1.00 V		2020
Cu-N-C (H-type cell)	Cu: 0.61 wt%	~-0.40	-0.67	98	~4 (maximum ~22 at -1.10 V)	No significant current loss within 20 hours of test at −0.67 V	-	Chen et al., 2021
Cu-N-C (electrolyte flow cell)	Cu: 0.61 wt%	~-0.10	-0.67	99	~75 (maximum ~130 at -1.13 V)	-	-	Chen et al., 2021
Cu-N_4-C/1100	Cu: 1.98 wt%	~-0.50	-0.90	98	~7 (maximum ~15 at -1.20 V)	No significant current loss within 40 hours of test at −0.80 V	-	Cheng et al., 2021

3.3.1 Nickel-based Single Atom Catalysts

Because of the very strong adsorption energy of carbon monoxide on it, the Ni (111) bulk surface can be easily poisoned by adsorbed CO. Therefore, instead of showing high CO_2RR activity towards CO production, Ni nanoparticles consisting of Ni metals/metal oxides/hydroxides are really active towards HER in aqueous solutions (Hall et al., 2013; Gong et al., 2014; Schneider et al., 2012). On the other hand, Ni SACs can show one of the highest activities towards CO_2RR to CO. As far as Ni SACs is concerned, Su et al. (2016), in alternative to organometallic electrocatalysts, synthesized Ni single atoms dispersed on N-doped graphene (named as Ni–N–Gr) by means of rapid heat treatment (900 °C, 1 min) of Ni-pentaethylenehexamine and graphene oxide (GO) under an inert atmosphere. This synthesis approach led to robust Ni-N bonds, where Ni atoms coordinated with N atoms in carbon-based materials (as shown in Figure 52) are expected to serve as catalyst centers for CO_2 reduction, while proton adsorption behavior on Ni was found to be a key co-factor inducing the high activity of the catalyst. The X-ray photoelectron spectroscopy (XPS) and extended X-ray absorption fine structure (EXAFS) results confirmed the existence of isolated Ni atoms coordinated with N with a loading of about 2.2 wt% embedded in the carbon matrix. This Ni SAC turned out to be highly selective towards CO with a CO Faradaic efficiency of over 90 % at -0.70 V *vs.RHE*.

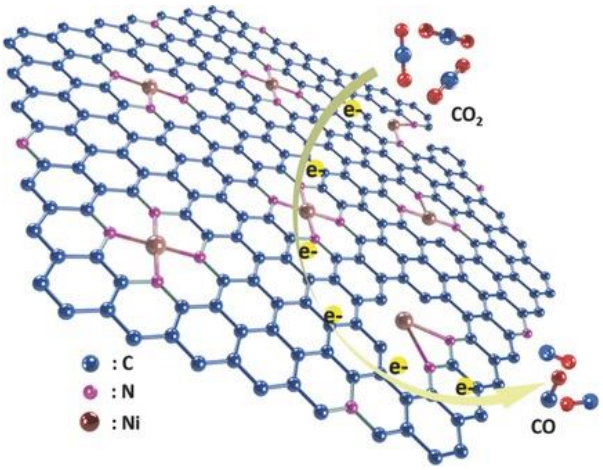

Figure 52. *Scheme of the CO_2RR to CO on the Ni-Nx active centers of the Ni–N–Gr catalyst. Reprinted with permission from (Su P., K. Iwase, T. Harada, K. Kamiya and S. Nakanishi (2018) Covalent triazine framework modified with coordinatively-unsaturated Co or Ni atoms for CO electrochemical reduction. Chem. Sci., **9**, 3941-3947). Copyright (2021) John Wiley and Sons*

Yang H. B. et al. (2018) synthesized Ni single atoms dispersed on N-doped graphene with and without being co-doped with S (defined as A-Ni-NG and A-Ni-NSG respectively), by pyrolysis of l-cystein, melamine and nickel acetate in argon. The as-obtained catalyst reached a CO Faradaic efficiency of 97 % at around -0.5 V, a specific current of 350 A per $g_{catalyst}$ at a 0.61 V overpotential, a low onset potential, and good stability, with only 2% of current loss after 100 hours of the test. The dispersion of Ni atoms on the graphene was confirmed by HAADF-STEM, which showed Ni atoms as bright spots with a size of about 0.2 nm within the carbon matrix (see Figure 53). In both A-Ni-NG and A-Ni-NSG. X-ray absorption spectroscopy and density functional theory (DFT) calculations allowed to discover that the geometry of the catalyst around Ni(I) centers was highly distorted because of a non-centrosymmetric ligand strength, which increased the adsorption strength of CO_2 and CO_2 reaction intermediates on A-Ni-NSG. Results demonstrated the existence of delocalization of the unpaired electron in the Ni 3d orbital and of a spontaneous charge transfer from Ni(i) to the 2p orbital of the carbon in carbon dioxide molecule to form intermediate adsorbed species.

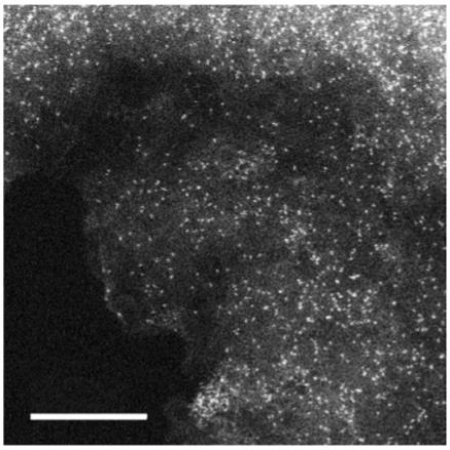

Figure 53. *HAADF-STEM image of the A-Ni-NG catalyst (scale bar: 5 nm). Reprinted with permission from (Yang H. B., S. F. Hung, S. Liu, K. D. Yuan, S. Miao, L. P. Zhang, X. Huang, H. Y. Wang, W. Z. Cai, R. Chen, J. J. Gao, X. F. Yang, W. Chen, W, Y. Q. Huang, H. M. Chen, C. M. Li, T. Zhang and B. Liu (2018) Atomically dispersed Ni(i) as the active site for electrochemical CO_2 reduction. Nat. Energy, **3**, 140-147). Copyright (2021) Springer Nature*

One of the major issues in the synthesis of SACs is the high surface energy of the metal sites causing their uncontrolled aggregation, which is favored either by the growth of synthesis temperatures generally over 700 °C or by the increase of the metal loading, consequently leading to a reduction of the catalytic performance. On the other hand, in nanomaterials many defects can be found, such as vacancies, step edges, caves, doped and lattice defects, which can alter the electronic structure and improve the catalytic performance of the catalysts (Fang et al., 2015; Ling et al., 2016; Yan et al., 2017). These defects can act as anchor sites for the stabilization of metal atoms, therefore combining single metal atoms and support defects can guarantee both high stability and high catalytic activities due to synergistic effects (Zhang L. et al., 2018). For instance, Qiao et al. (2015) prepared a Au/FeO_x-type catalyst and discovered that the isolated Au atoms anchored at Fe vacancy sites exhibit very high binding energies, being highly positively charged. This leads to the formation of strong covalent bonds between the Au atoms and the lattice oxygen atoms of FeO_x, hence stabilizing the atoms on the support surface. Therefore, the strong metal–support interactions can be seen as a consequence of the presence of defects created on the surfaces of the oxides.

Going back to talk about the M-N-C-based SACs (with M as generic transition metal), which are the most frequently adopted for the CO_2RR

catalysis, Jiang et al. (2017) synthesized Ni single atoms anchored to a graphene shell for the CO_2RR to CO, leading to a maximum CO Faradaic efficiency of 93.2 % at -0.82 V *vs.RHE* with a CO partial current density of 20 mA/mg. The above-mentioned catalyst (NiN-GS) was obtained through electrospinning of polymer nanofibers with Ni and N precursors homogeneously distributed. Transmission electron microscopy (TEM) images confirmed that HER-active Ni NPs are formed within the carbon shell, which covers them, by impeding the core from participating in the CO_2 reduction. Three-dimensional atom probe tomography (APT) confirmed the existence of atomically dispersed Ni sites anchored on the graphene vacancies (see Figure 54). In particular, among all the Ni single atomic sites, only 0.2% were directly anchored to N, while 98% of them were embedded within the carbon defects in the graphene vacancies. As a consequence of DFT calculation results, the authors proposed that the most active sites towards the CO production are the Ni atoms embedded within the carbon defects in the graphene vacancies, whereas N atoms promoted the entrapment of Ni atoms by generating defects in the graphene structure.

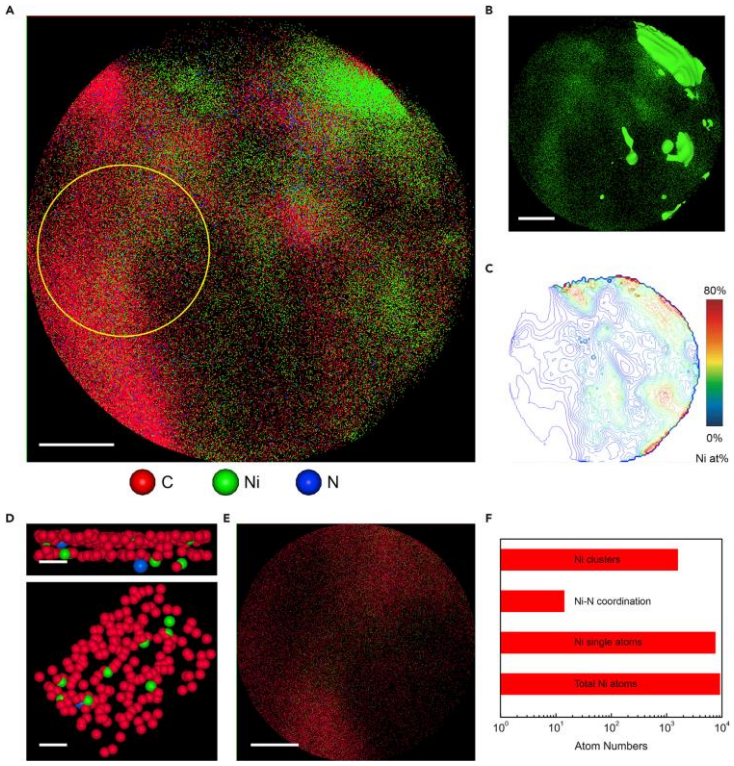

Figure 54. *Three-dimensional atom probe tomography (APT) of the NiN-GS catalyst. (A) The two-dimensional atomic map of NiN-GS. The yellow circle represents the selected area for statistical studies in (E) and (F). Scale bar, 10 nm. (B) The two-dimensional projected view of Ni atoms. The green areas represent Ni-rich areas (>50 at %). Away from the Ni sources, there are still a significant number of Ni atoms dispersed in the carbon area. Scale bar, 10 nm. (C) The contour map of Ni concentration with an interval of 2 at %. (D) Zoomed in side view (upper) and top view (lower) of graphene layers with Ni single atoms coordinated in vacancies. Only one Ni atom is directly coordinated with one N atom. Scale bars, 1 nm. (E) Atom map of the selected area in (A) as indicated by the yellow circle. Scale bar, 5 nm. (F) The statistics of the selected area in (E). Most of the Ni atoms are in single-atom morphology, and 0.2% of them are coordinated with N atoms. Reprinted with permission from (Jiang K., S. Siahrostami, A. J. Akey, Y. B. Li, Z. Y. Lu, J. Lattimer, Y. F. Hu, C. Stokes, M. Gangishetty, G. X. Chen, Y. W. Zhou, W. Hill, W. B. Cai, D. Bell, K. R. Chan, J. K. Nørskov, Y. Cui and H. T. Wang (2017) Transition-Metal Single Atoms in a Graphene Shell as Active Centers for Highly Efficient Artificial Photosynthesis. Chem, **3**, 950-960). Copyright (2021) Elsevier*

Furthermore, Jiang et al. (2018) synthesized Ni single atoms coordinated on graphene nanosheets through its vacancies (Ni-NG), obtaining a catalyst with high electrochemical performance. The authors explained that layered GO nanosheets were selected as support material for Ni SACs because of the high density of defects on GO, the high surface and negatively charged area as well as the presence of a two-dimensional structure allowing clear characterization of the atomic sites. They firstly incorporated Ni ions into GO nanosheets and, afterward, annealed them at 750 °C using ammonia as a reducing reagent and source of N dopants. The result is a catalyst that exhibited a CO FE of over 95% at -0.62 V *vs.RHE*, mainly due to its Ni-N atomic sites.

Yuan et al. (2020) prepared Ni single atoms anchored to nitrogen-doped hollow carbon spheres (SA-Ni/N-CS) by means of a semi-sacrificial template-assisted synthesis approach. SiO_2/polydopamine spheres were chosen because they can efficiently adsorb Ni^{2+} ions coming from a $Ni(NO_3)_2 \cdot 6H_2O$ precursor on their cavities. After pyrolysis, they were transformed into N–C hollow spheres and the adsorbed Ni^{2+} ions were embedded into the N-rich carbon matrix. Eventually, etching of the SiO_2 core and Ni nanoparticles was carried out through a diluted hydrofluoric acid solution. The as-prepared SA-Ni/N-CS catalyst exhibited an excellent CO faradaic efficiency of 95.1% at −0.8 V *vs.RHE* and 24-hours stability without any current loss.

Another important parameter which influences catalytic activity and selectivity is the coordination number of the metallic atoms with N. In particular, Ni single atom-based catalysts are reported to be highly active towards CO_2RR when each Ni atom is coordinated with four N atoms. Li et al. (2017) synthesized a catalyst with exclusive $Ni–N_4$ active moieties through a topo-chemical transformation method. According to this strategy, a Ni-doped graphitic carbon nitride (g-C_3N_4) was synthesized starting from a mixture in water of dicyandiamide, NH_4Cl and $NiCl_2$. Afterward, it was dispersed in a glucose solution, heated at 180 °C for 10 hours and, eventually, annealed at 1000 °C for 1 hour in order to coat Ni-doped g-C_3N_4 on a carbon layer, hence preventing Ni atoms from aggregation. Because of the high presence of Ni-N_4 active sites, the Ni-N_4-C catalyst exhibits a maximum CO FE of 99% at −0.81 V *vs.RHE* with a total current density of 28.6 mA/cm^2. The high contribution of Ni-N_4 sites for the CO_2RR to CO was confirmed since the poisoning of the Ni atoms through thiocyanate significantly reduced catalytic activity (see Figure 55).

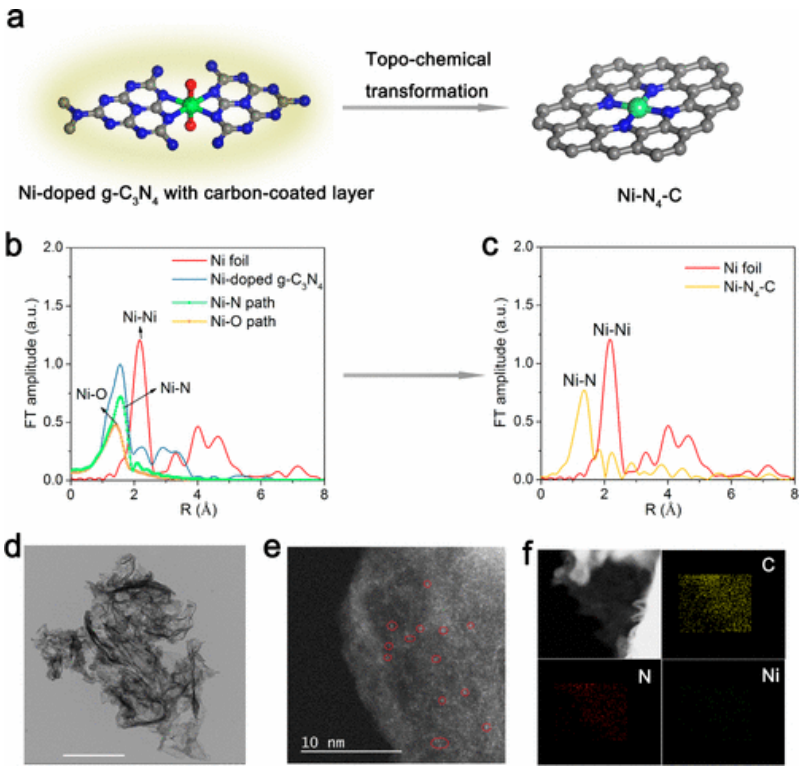

Figure 55. *Ni-N_4 as effective active sites for the CO_2RR to CO. (a) Scheme of the synthesis of the Ni-N_4-C catalyst (Ni atoms in green; N atoms in blue; C atoms in gray; O atoms in red); (b) Fourier transform of the Ni K-edge EXAFS oscillations of Ni-doped g-C_3N_4 with carbon-coated layer; (c) Fourier transform of the Ni K-edge EXAFS oscillations of the Ni–N_4–C catalyst; (d) TEM image of the Ni–N_4–C catalyst (scale bar: 500 nm); (e) HAADF-STEM result for of the Ni–N_4–C catalyst; (e) Element mapping images of the Ni–N_4–C catalyst. Reprinted with permission from (Li X., W. Bi, M. Chen, Y. Sun, H. Ju, W. Yan, J. Zhu, X. Wu, W. Chu, C. Wu and Y. Xie (2017) Exclusive Ni−N_4 Sites Realize Near-Unity CO Selectivity for Electrochemical CO_2 Reduction. J. Am. Chem. Soc., **139**, 14889-14892). Copyright (2021) American Chemical Society*

Su et al. (2018) proposed the synthesis of Ni single atoms on a covalent triazine framework (CTF), a conjugated polymer with 1,3,5-triazine linker units. The catalyst, named as Ni-CTF achieved good electrocatalytic performance and a high CO selectivity (CO FE of about 95% at -0.90 V *vs.RHE*). The authors demonstrated that the lower coordination number of Ni atoms on CTF can increase the binding strength of reaction intermediates during CO_2RR, being such single atoms more reactive. Indeed, the

coordination number of the metal species in the catalyst can be used as an additional control parameter to improve the performance towards CO_2RR.

Another strategy to synthesize SACs is to adopt a highly porous metal-organic framework (MOF) as template, such as ZIF-8 [Zn(MeIm)2], a zeolitic imidazolate framework obtained from Zn^{2+} nodes and 2-methylimidazole. Zhao et al. (2017) prepared Ni atoms dispersed on a N-doped carbon matrix (named as NiSACs/N-C) for CO_2RR by a ZIF-assisted method based on an ionic exchange between Ni ions and Zn nodes within the ultrafine pores of ZIF-8 (as summarized in Figure 56). During the pyrolysis step, the low-boiling-point Zn nodes evaporated, leaving the N-rich defects to be occupied by the neighboring Ni^{2+} ions, hence preventing them from agglomeration. As a result, Ni single atoms were formed, each of them coordinated with 3 N atoms homogeneously distributed on carbon matrix. The presence of Ni–N_3 active centers guaranteed good CO_2RR catalytic activity with a selectivity towards CO of over 71.9% at a 0.89 V overpotential as well as high stability.

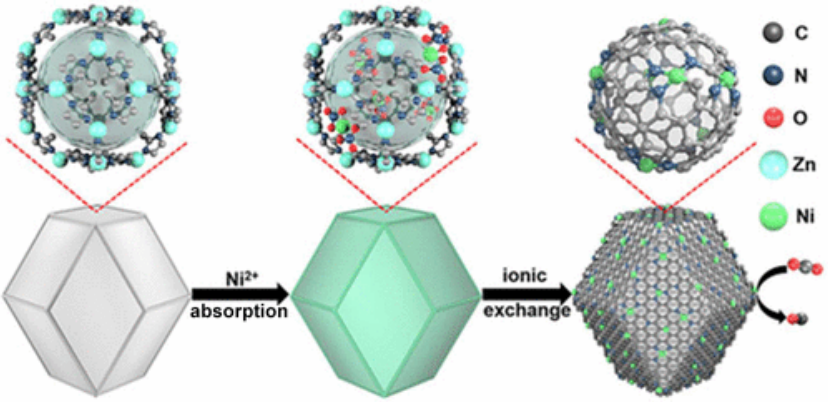

Figure 56. *Schematic illustration of the synthesis of Ni SAs/N-C through a ZIF-assisted method. Reprinted with permission from (Zhao C., X. Dai, T. Yao, W. Chen, X. Wang, J. Wang, J. Yang, S. Wei, Y. Wu and Y. Li (2017) Ionic Exchange of Metal–Organic Frameworks to Access Single Nickel Sites for Efficient Electroreduction of CO_2. J. Am. Chem. Soc.,* ***139****, 8078-8081). Copyright (2021) American Chemical Society*

Hou et al. (2020) successfully synthesized Ni single atoms stabilized on N-doped carbon nanotubes (Ni/NCTs) through a self-sacrifice template method carried out by pyrolyzing ZnO/ZIF-NiZn core/shell nanorods and by subsequently removing Zn species via acid etching. Compared with the Ni single atoms supported on porous bulk carbons prepared with a similar approach, the Ni/NCTs catalyst showed much better performance towards CO_2RR to CO with a more positive onset potential of -0.323 V, a much larger CO current density of 34.3 mA/cm^2 at -1.0 V *vs.RHE* and a CO FE of

almost 100% in the potential range -0.6 V ÷ -1 V. According to the authors, this is mainly due to the hierarchically porous structure and high surface area of the nanotubes as well as to the Ni-N active centers. HAADF-STEM, *S*EM, TEM images with corresponding EDS maps of the catalyst are reported in Figure 57.

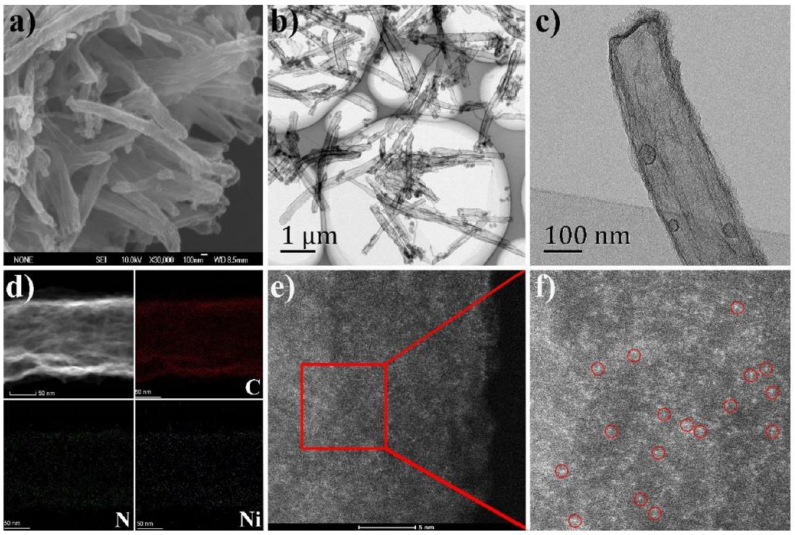

Figure 57. *(a) SEM image, (b-c) TEM images of Ni/NCTs, and (d) its corresponding EDS mapping reveals the homogeneous distribution of Ni, C, and N elements. (e-f) Aberration-corrected HAADF-STEM image with scale bars 5 nm and enlarged image of Ni/NCTs. Partial of single Ni atoms are highlighted by red circles. Reprinted with permission from (Hou Y., Y. L. Liang, P. C. Shi, Y. B. Huang and R. Cao (2020) Atomically dispersed Ni species on N-doped carbon nanotubes for electroreduction of CO_2 with nearly 100% CO selectivity. Appl. Catal. B Environ., **271**, 11892). Copyright (2021) Elsevier*

Another challenge to overcome in the development of SACs is the necessity to increase the atomic loading, which is typically less than 2 wt% because of the insufficient number of anchoring sites on the support, as well as because the higher the metal loading is, the more likely the agglomeration of atoms during synthesis would be. Recently, Cheng et al. (2018a) synthesized Ni SACs on an extremely porous and high surface defect-rich microwave exfoliated graphene oxide (Ni–N–MEGO), reaching a Ni SACs loading of 6.9 wt%. The support is endowed with a highly porous surface area (2649 m^2/g), which provides a high number of anchor sites for single Ni atoms, as shown in Figure 58. The large amount of nanopores, whose average size is less than 6 nm, contributes to reducing aggregation and

stabilizing the SA Ni-N centers during high-temperature annealing. The catalyst showed a high CO FE of 92.1% at -0.70 V *vs.RHE* as well as a low onset potential of 0.29 V.

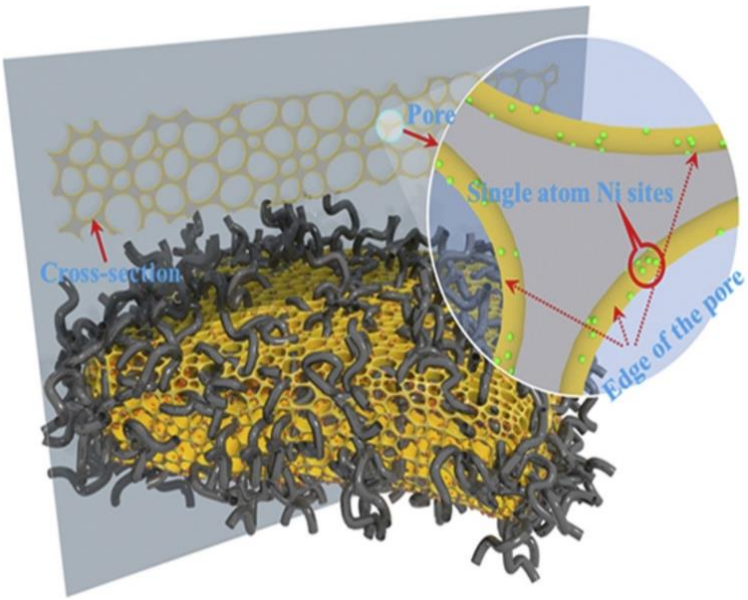

Figure 58. *Schematic illustration of the highly-porous Ni–N–MEGO catalyst. Reprinted with permission from (Cheng Y., S. Zhao, H. Li, S. He, J. P. Veder, B. Johannessen, J. Xiao, S. Lu, J. Pan, M. F. Chisholm, S. Z. Yang, C. Liu, J. G. Chen and S. P. Jiang (2018a) Unsaturated edge-anchored Ni single atoms on porous microwave exfoliated graphene oxide for electrochemical CO_2.* Appl. Catal. B Environ.*, **243**, 294-303). Copyright (2021) Elsevier*

In a later study, the authors managed to synthesize a Ni SACs with the highest atomic loading of 20 wt% (Cheng et al., 2018b). The catalyst was obtained by means of a multistep pyrolysis process, starting from a mixture of dicyanamide and Ni acetylacetonate, and the 20 wt% loading was obtained when the annealing temperature reached 800 °C. The result is Ni single atoms dispersed on the walls of bamboo-like carbon nanotubes (NiSA-N-CNT), with an estimated coordination number for Ni–N of 3.8 ± 0.7, suggesting that Ni–N_4 active sites were formed during synthesis. Other metals such as Co, Fe and Pt have also been adopted in the same catalyst formulation instead of Ni, but their catalytic performance is lower. This suggests the superiority in terms of catalytic activity of the previously synthesized Ni-based catalyst owing to the presence of the more active Ni–N_4 centers.

As previously mentioned, the typical electrochemical system adopted in all the above-mentioned studies is the H-type cell. One main limitation of such a configuration, in which CO_2 molecules must diffuse through the liquid electrolyte to reach the electrode surface, is that the equilibrium concentration of CO_2 in an aqueous solution at 1 bar and 25 °C is about 30 mM, which corresponds, considering the occurring of CO evolution reaction, to a maximum achievable current density of 60 mA/cm^2, a figure which is one order of magnitude below typical industrial current densities (Weekes et al., 2018; Martín et al., 2015). A solution to achieve higher current density values consists in continuous-flow reactors where CO_2 is directly supplied from the gas phase through gas diffusion electrodes (GDEs), which integrate a catalyst layer with a porous substrate, allowing to both increase the mass transport phenomena and enhance the electrochemically active surface area. Yang et al. (2020) synthesized Ni single atoms on a porous carbon fiber membrane (NiSA/PCFM) through the electrospinning method. In virtue of its high porosity, excellent mechanical strength and good flexibility, NiSA/PCFM could combine gas-diffusion and catalyst layers into a single architecture and work as a gas diffusion electrode. Loaded on the cathode compartment of a flow electrolyte cell, the catalyst generated a maximum total current density of about 360 mA/cm^{2,} comparable with industrial applications, with a CO selectivity of around 88% at −1.0 V *vs.RHE* and long-term stability without any significant current losses for 120 hours (see Figure 59). Möller et al. (2019), tested their Ni-N-C electrocatalyst, synthesized by pyrolysis of a mixture of polyaniline, carbon- and Ni-precursors, in an industrial-like flow electrolytic cell and by spry-coating the catalyst ink on a gas diffusion electrode in order to overcome the limitation of the CO_2 solubility in water at ambient temperature and pressure. The Ni–N–C catalyst exhibited a maximum CO FE of almost 90% between CO current densities of 100 and 200 mA/cm^2 and maintained the 200 mA/cm^2 for 20 hours of tests.

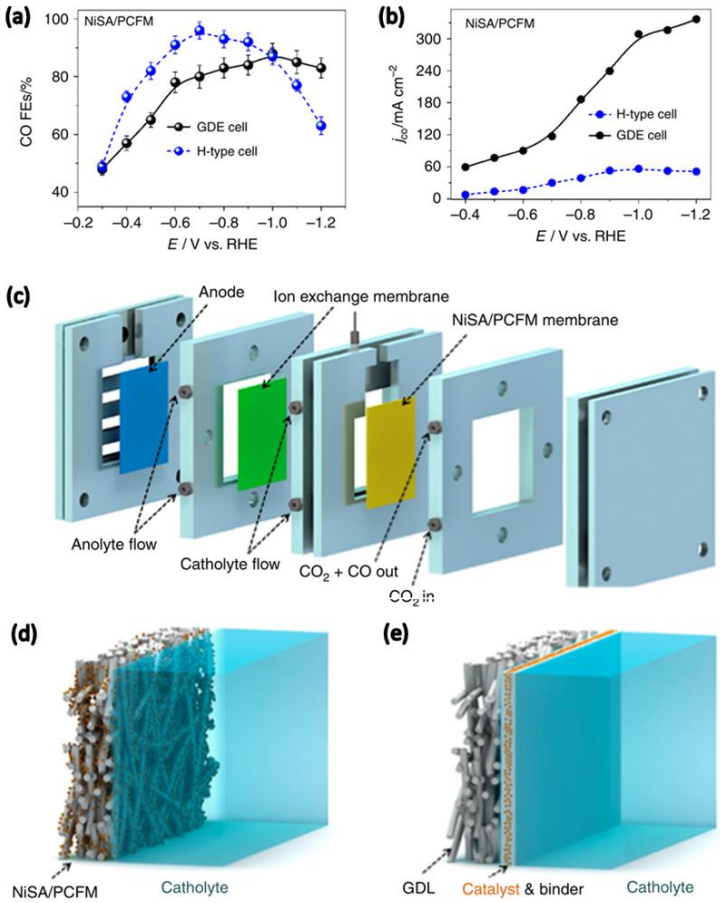

Figure 59. *Example of application of Ni-N-C type catalyst as GDE for a flow-electrolyte cell. (a) CO faradaic efficiencies and (b) partial current densities as functions of the applied potential vs.RHE of NiSA/PCFM in both H-type cell and GDE flow-cell; (c) Representation of a GDE device; (d) NiSA/PCFM membrane adopted as GDE and (e) a typical GDE cell in which the catalyst is located onto a gas-diffusion layer through a polymer binder. Reprinted with permission from (Yang H., Q. Lin, C. Zhang, X. Yu, Z. Cheng, G. Li, Q. Hu, X. Ren, Q. Zhang, J. Liu and C. He (2020) Carbon dioxide electroreduction on single-atom nickel decorated carbon membranes with industry compatible current densities. Nat. Commun., **11**, 593). Copyright (2021) Springer Nature*

After a long period of literature results reporting studies about catalysts for CO evolution from CO_2RR, only recently attention has been placed on the development of an efficient Ni SAC for the CO_2 electrochemical conversion into syngas with a tunable CO/H_2 ratio. Zhu W. et al. (2020) synthesized N-doped carbon nanorods containing both Ni single atoms and

Ni nanoparticles (named as NiNP CNRs), which favored CO_2RR to CO and HER respectively. With such a catalyst, syngas with a wide range of CO/H_2 ratios could be obtained by simply tuning the ratio between Ni NPs and Ni single atoms, which could be achieved by controlling the acid etching time after pyrolysis of nickel precursor. As showed in Figure 60, by changing the etching time from 2 hours to 48 hours, the ratio between Ni-N sites and Ni NPs changed from 1:4.9 to 1:0 and, subsequently, a syngas with a CO/H_2 ratio ranging from 1:9 to 19:1, a total current density higher than 15 mA/cm^2 and stability for over 8 hours could be obtained.

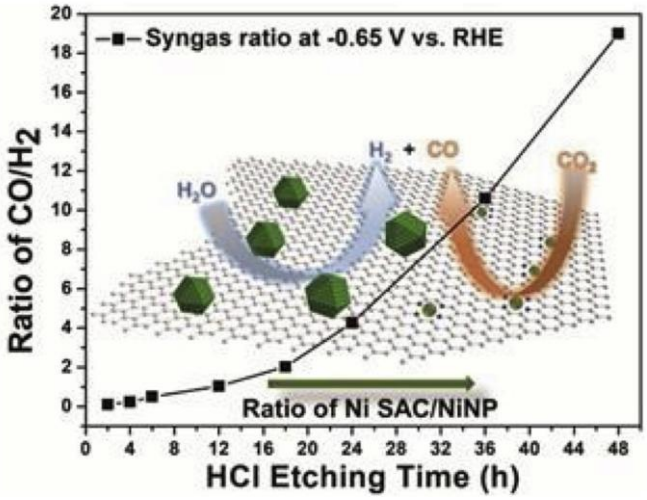

Figure 60. *Ratio of CO/H_2 versus HCl etching time for the NiNP CNRs catalyst. Reprinted with permission from (Zhu W., J. Fu, J. Liu, Y. Chen, X. Li, K. Huang, Y. Cai, Y. He, Y. Zhou, D. Su, J. J. Zhu and Y. Lin (2020) Tuning single atom-nanoparticle ratios of Ni-based catalysts for synthesis gas production from CO_2. Appl. Catal. B Environ., **264**, 118502). Copyright (2021) Elsevier.*

3.3.2 Cobalt-based Single Atom Catalysts

Co single atoms dispersed on N-doped carbon-based materials have been recently explored as good catalysts for the CO_2RR to CO. In contrast to Ni SACs, the typical Co–N_4 moiety does not represent the most active center for CO production. Wang X. et al. (2018) synthesized atomically dispersed Co catalysts on N-doped porous carbon through pyrolysis of a bimetallic Co/Zn ZIF. By varying the pyrolysis temperature, the authors managed to obtain SACs with different coordination numbers for Co (see Figure 61a). In particular, Co–N_4, Co–N_3, and Co–N_2, were synthesized at 800, 900, and

1000 °C, respectively, along with Co NPs for a better comparison. In Figures 61b-g SEM, TEM, HAADF and Selected-area electron-diffraction (SAED) studies revealed that, for instance, the Co-N_2 catalyst retained the morphology of the starting ZIFs after the synthesis and it consisted of single Co atoms homogeneously distributed on the N-C support, with poor crystallinity. On Co-N_2, a CO current density of 18.1 mA/cm^2 was reached at −0.63 V *vs.RHE*, which is a value of 23.3, 7.3, and 2.0 times higher than the ones obtained on Co–N_4, Co–N_3, and Co NPs respectively. Co–N_2 exhibited a maximum CO FE of 95% at −0.68 V *vs.RHE*, while Co–N_3 and Co NPs reached a maximum CO FE of 63% at −0.53 V *vs.RHE* and of around 7% at all the analyzed potentials, respectively. What is more, the Co–N_4 catalyst was found to be rather inactive towards CO_2RR. DFT calculations (see Figure 62) revealed that, on the Co–N_2-based catalyst, the $CO_2^{\cdot-}$* intermediate is more easily formed, which means a higher CO_2RR catalytic activity. On the other hand, on Co NPs the formation of the H* intermediate is much more favored, hence hampering the CO_2RR. As for the Co–N_4 catalyst, the adsorption energies of $CO_2^{\cdot-}$* and H* are high, which means that both HER and CO_2RR require high overpotentials to occur on it. The H* adsorption energy on Co–N_4 is anyhow lower than the one related to $CO_2^{\cdot-}$*, which makes the catalyst superior towards HER.

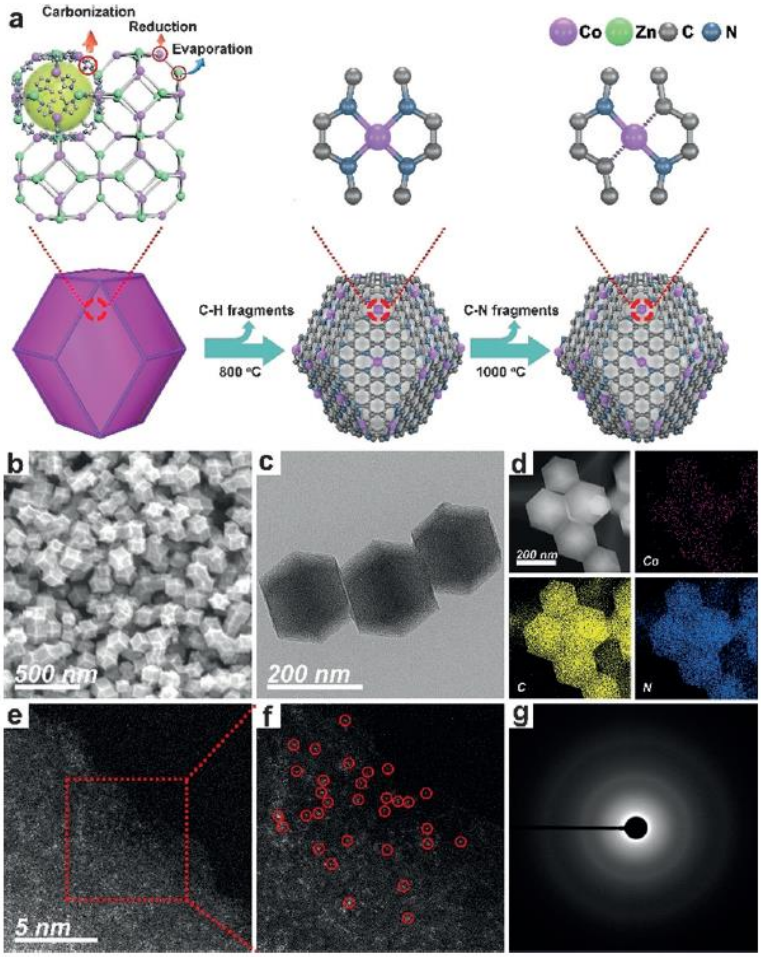

Figure 61. *a) A scheme of the synthesis process of Co-N_4 and Co-N_2. b) SEM and c) TEM images of Co-N_2. d) Examination of the corresponding EDS mapping reveals the homogeneous distribution of Co and N on the carbon support. e),f) Magnified HAADF-STEM images of Co-N_2 shows the atomic dispersion of Co atoms. g) Corresponding SAED pattern of Co-N_2. Reprinted with permission from (Wang X., Z. Chen, X. Zhao, T. Yao, W. Chen, R. You, C. Zhao, G. Wu, J. Wang, W. Huang, J. Yang, X. Hong, S. Wei, Y. Wu and Y. Li (2018) Regulation of Coordination Number over Single Co Sites: Triggering the Efficient Electroreduction of CO_2. Angew. Chem. Int. Ed., **57**, 1944-1948). Copyright (2021) John Wiley and Sons*

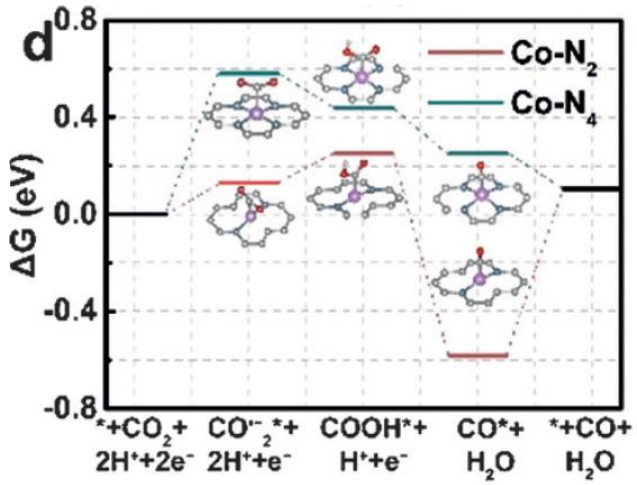

Figure 62. *Gibbs free energy diagrams for CO_2 electroreduction to CO on Co-N_2 and Co-N_4. Reprinted with permission from (Wang X., Z. Chen, X. Zhao, T. Yao, W. Chen, R. You, C. Zhao, G. Wu, J. Wang, W. Huang, J. Yang, X. Hong, S. Wei, Y. Wu and Y. Li (2018) Regulation of Coordination Number over Single Co Sites: Triggering the Efficient Electroreduction of CO_2. Angew. Chem. Int. Ed., **57**, 1944-1948). Copyright (2021) John Wiley and Sons*

Most recently, Pan Y. et al. (2018) synthesized Co single atoms anchored on polymer-derived hollow N-doped porous carbon spheres with Co–N_5 active centers (named as Co–N_5/HNPCSs, see Figure 63), which showed a CO FE of 99.2% and 99.4% at −0.73 V *vs.RHE* and −0.79 V *vs.RHE*, respectively. Similarly, to the previous study, a comparison with SACs synthesized at different pyrolysis temperatures (Co–N_4 and Co–N_3, obtained at 400 and 600 °C respectively) showed the higher performance of the Co-N_5: indeed, the CO FE decreased as the Co–N_x coordination number dropped to 3 and 4. DFT calculations confirmed the importance of the crucial role of the Co-single atom active sites, which must possess a high COOH* intermediate adsorption strength as well as a moderate CO adsorption energy.

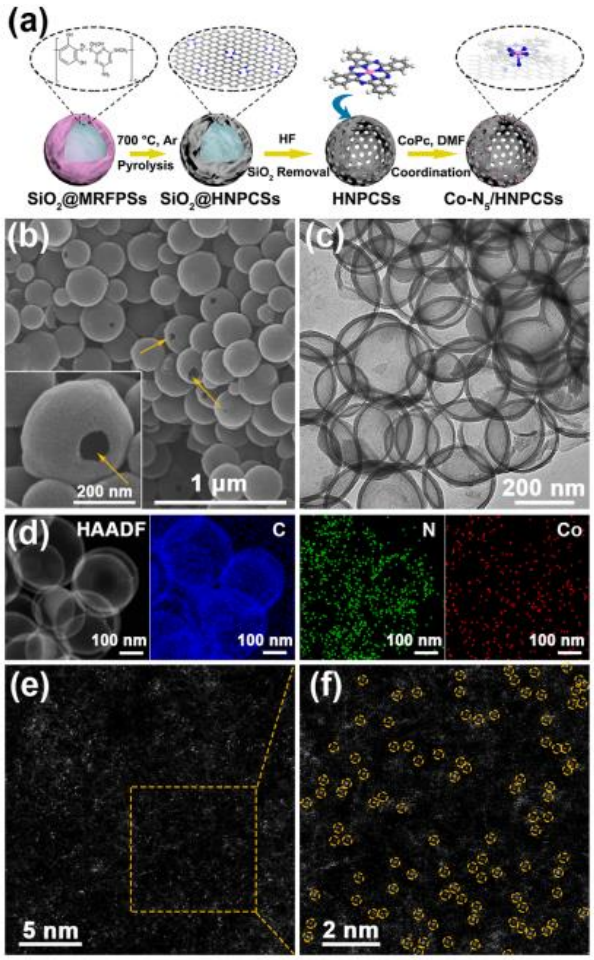

Figure 63. *Co-N_5 as effective active sites for the CO_2RR to CO. (a) Scheme of the Co–N_5/HNPCSs synthesis; (b) SEM, (c) TEM, (d) HAADF-STEM and EDS images of the Co-N_5/HNPCSs catalyst (C atoms in blue, N atoms in green and Co atoms in red). (e, f) Aberration corrected HAADF-STEM image and a further HAADF-STEM magnified image of the Co-N_5/HNPCSs catalyst. Reprinted with permission from (Pan Y., R. Lin, Y. Chen, S. Liu, W. Zhu, X. Cao, W. Chen, K. Wu, W. C. Cheong, Y. Wang, L. Zheng, J. Luo, Y. Lin, Y. Liu, C. Liu, J. Li, Q. Lu, X. Chen, D. Wang, Q. Peng, C. Chen and Y. Li (2018) Design of Single-Atom Co–N_5 Catalytic Site: A Robust Electrocatalyst for CO_2 Reduction with Nearly 100% CO Selectivity and Remarkable Stability. J. Am. Chem. Soc., **140**, 4218-4221). Copyright (2021) American Chemical Society*

Most recent studies are focused on the adoption of Co-based SACs for syngas production. These recent studies focus on the idea that the bifunctionality of the catalyst is the key to enabling a tunable co-generation of CO and H_2. Daiyan et al. (2020) synthesized a Co-single atom decorating, N-doped graphitic carbon shell encapsulating a Co NPs core (Co@CoNC-900) capable of producing a stable H_2/CO ratio ranging from 0.25 to 1 in the -0.3 V÷ -0.8 V *vs.RHE* potential range. As for this catalyst, the authors recognized the following active sites, according to DFT calculations: the graphitic shell encapsulating metallic Co core for the CO_2RR and the Co-N_4 moieties on the top of the shell for HER (see Figure 64). They also tested the effect of the annealing temperature on the H_2/CO ratio from ~1.5 (when the annealing temperature is 800 °C) to 1 (when the annealing temperature is 900 °C) to ~0.5 (when the annealing temperature reaches 1000 °C, within a wide potential range).

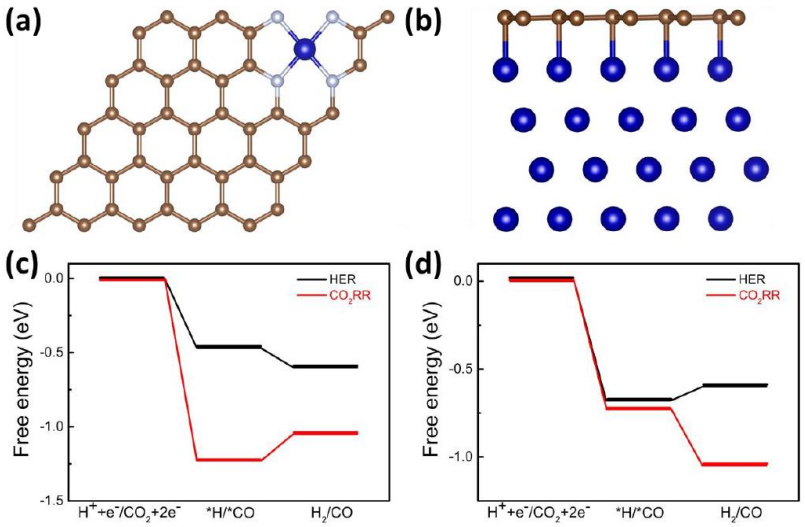

Figure 64. *DFT calculations with Co@CoNC catalysts. Structural models for (a) Co-N_4 and (b) Co encapsulated carbon shell. The C, Co, N and O atoms are represented using brown, dark blue, light blue and red spheres, respectively. The calculated free energy diagrams for CO_2RR and HER on (c) Co-N_4 and (d) modified carbon shells at an intermediate operating potential of -0.6 V. Reprinted with permission from (Daiyan R., R. Chen, P. Kumar, N. M. Bedford, J. Qu, J. M. Cairney, X. Lu and R. Amal (2020) Tunable Syngas Production through CO_2 Electroreduction on Cobalt-Carbon Composite Electrocatalyst. ACS Appl. Mater. Interfaces,* ***12****, 9307-9315). Copyright (2021) American Chemical Society*

On the other hand, Song et al. (2018) proposed that the CO_2RR active sites of the catalyst are the Co–C_2N_2 moieties, while other nitrogen groups, such as graphitic and pyridinic N, can favor HER. In detail, the authors synthesized a Co single atom catalyst supported on a nitrogen-doped 3D hollow carbon structure (named as Co-HNC) for the syngas production through a 900 °C pyrolysis of a ZnO/ZIF core/shell precursor. The chosen precursor and the synthetic process enable to obtain a catalyst with a tridimensional hollowed structure and a sponge-like thin shell with a hierarchical porous system, which favor the mass transport phenomena and make the active sites highly exposed. The result is a catalyst able to guarantee the formation of syngas with a stable CO/H_2 ratio of 1/2 in the potential range -0.7 ÷ -1 V *vs.RHE* and a CO FE of around 35% for applied potentials above −0.8 V. From this work, the importance of the spatial configuration of the adsorbed CO_2 molecule on the active site can also be deduced. Figure 65 shows several configurations but the only model I has a slightly negative binding energy, which means the highest probability of existence when compared with the others. Furthermore, since the O atoms of the CO_2 molecule tend to locate close to the pyridinic N atoms linked to the Co atom, which are active towards HER, this configuration explains why the Co–C_2N_2 moiety favors CO_2RR, while hindering HER.

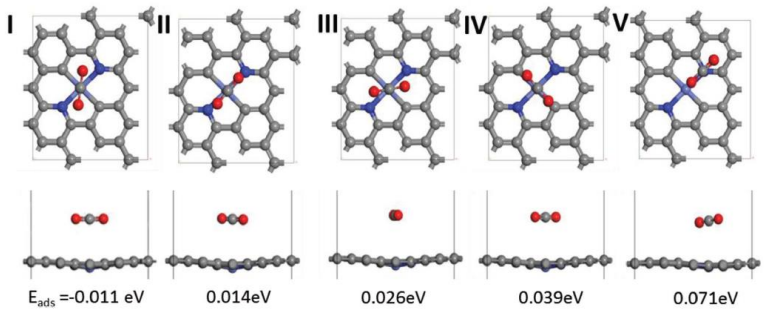

Figure 65. *Top-view and side-view of the different spatial configurations of the CO2 molecule on the Co–C_2N_2 moieties. Reprinted with permission from (Song X., H. Zhang, Y. Yang, B. Zhang, M. Zuo, X. Cao, J. Sun, C. Lin, X. Li and Z, Jiang (2018) Bifunctional Nitrogen and Cobalt Codoped Hollow Carbon for Electrochemical Syngas Production. Adv. Sci., **5**, 1800177). Copyright (2021) John Wiley and Sons*

3.3.3 Iron-based Single Atom Catalysts

Among single atom catalysts for the CO_2RR to CO, Fe-based single atoms catalysts have been also recently explored as single atoms dispersed on N-doped carbon supports. Fe SACs can exhibit high selectivity towards CO, with a maximum achievable CO FE of about 98% at -0.68 *vs.RHE* (Wu et al., 2002), comparable to the values achieved with Co-based and Ni-based SACs. However, unlike them, Fe-N-C electrocatalysts exhibit the highest CO selectivity at low overpotentials, approximately from – 0.43 V *vs.RHE* to – 0.68 V *vs. RHE*. Nonetheless, the current densities recorded on these Fe-based catalysts are rather low, with a maximum total current density (CO and H_2) of around 35 mA/cm^2 at -1.35 V *vs. RHE*. Zhang C. et al. (2018) adopted electrochemically exfoliated graphene-based foils, melamine and 1-butyl3-methylimidazolium tetrachloroferrate ([BMIM]$FeCl_4$) to obtain Fe atoms along with Fe_3C nanocrystals embedded into a graphene nanosheets/bamboo-carbon nanotubes matrix by electrochemical charging and ball-milling followed by annealing. The result is an effective catalyst (named as Fe-N-G/bC) towards CO_2RR which achieved a CO Faradaic efficiency of about 95.8 % at -0.66 V *vs.RHE* and a total current density of around 33 mA/cm^2 at -1.20 V. The authors explained the good activity as a result of the Fe–N_x active sites and the Fe_3C phase, which could lead to synergistic effects in combination with the atomic active sites. Moreover, the hierarchical porous carbon matrix facilitated reactant accessibility and fast pathways for charge and mass transport.

Zhang H. et al. (2018) immobilized Fe atoms on N-doped graphene support (Fe/NG) by annealing a mixture of graphene oxide and $FeCl_3$ in an Ar/NH_3 atmosphere at 650–800 °C, which did not lead to the formation of Fe nanocrystals (as schematized in Figure 66). The existence of Fe single atoms combined with nitrogen atoms in the graphene layers was confirmed by means of both HAADF-STEM and XAFS and the high selectivity to the catalyst towards CO (80% CO FE at -0.57 V *vs.RHE*) could be attributed to a synergistic effect between these two atomic species on graphene. Eventually, DFT helped understand that the synergetic effect of the Fe–N_4 moieties and nitrogen-doping on the graphene surface (the Fe-N_4 + $2N_{g(2)}$ active sites) is the main reason for the high electrochemical performance (see Figure 67). A similar result was found also by Zhu Y. et al. (2020), whose catalyst is constituted by single atomic iron evenly dispersed on N-doped carbon nanosheets obtained by pyrolysis of hemin-doping polyaniline (named as Fe-SA/NCS-X, with X referring to the pyrolysis temperature). Even in this case, DFT results indicated that the presence of graphitic N synergistically improved the CO_2RR activity of the Fe-N_4 active center by reducing the free energy barrier for the formation of the COOH* intermediate.

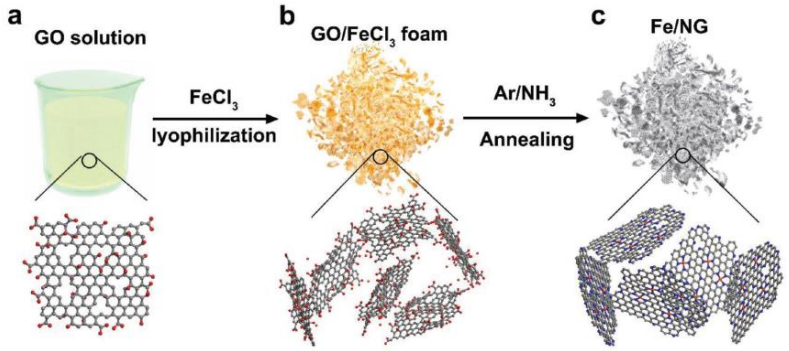

Figure 66. *Scheme of the formation procedure of Fe/NG. a) GO suspension in deionized water; b) Fe/$FeCl_3$ foam obtained by lyophilization of GO and $FeCl_3$; and c) the final Fe/NG catalyst synthesized by annealing at 650–800 °C under Ar/NH_3 atmosphere. Reprinted with permission from (Zhang C., S. Yang, J. Wu, M. Liu, S. Yazdi, M. Ren, J. Sha, J. Zhong, K. Nie, A. S. Jalilov, Z. Li, H. Li, B. I. Yakobson, Q. Wu, E. Ringe, H. Xu, P. M. Ajayan and J. M. Tour (2018) Electrochemical CO_2 Reduction with Atomic Iron-Dispersed on Nitrogen-Doped Graphene. Adv. Energy Mater., **8**, 1703487). Copyright (2021) John Wiley and Sons*

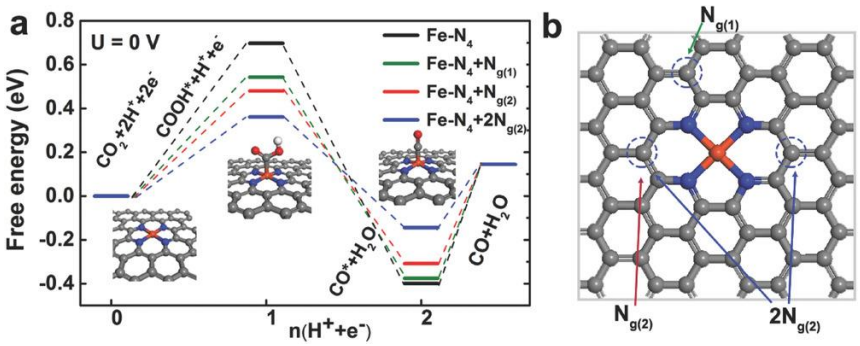

Figure 67. *Fe-N_4 as effective active sites for the CO_2RR to CO. a) Free energy vs. reaction path graph for the CO_2RR to CO on different Fe–N_4 centers for the Fe/NG catalyst. b) Top view-scheme of the Fe/NG catalyst highlighting the Fe–N_4 center (Fe atom in red, N atoms in blue) and the potential nitrogen-substitute atoms. Reprinted with permission from (Zhang C., S. Yang, J. Wu, M. Liu, S. Yazdi, M. Ren, J. Sha, J. Zhong, K. Nie, A. S. Jalilov, Z. Li, H. Li, B. I. Yakobson, Q. Wu, E. Ringe, H. Xu, P. M. Ajayan and J. M. Tour (2018) Electrochemical CO_2 Reduction with Atomic Iron-Dispersed on Nitrogen-Doped Graphene. Adv. Energy Mater., **8**, 1703487). Copyright (2021) John Wiley and Sons*

Cheng et al. (2018c) synthesized a Fe–N–C nanofiber encapsulating iron nitride nanoparticles through its Fe and N co-doped carbon layers (named as Fe–N/CNF) through electrospinning, carbonization, acid-leaching, and nitridation under NH_3. The as-obtained catalyst showed high catalytic activity towards CO_2RR, especially the one obtained after a 20-minutes-nitridation time (Fe–N/CNF-2) which exhibited over 95% of CO Faradaic efficiency at -0.53 V *vs.RHE*. DFT calculations revealed that the desorption of the adsorbed CO from the Fe-N-based shell is easier when the iron nitride core is included. Indeed, in the catalyst without Fe_2N (Fe-N_4-C), CO_2 adsorption is highly exothermic, but this is not an advantage: the binding energy of adsorbed CO on the Fe atom is too strong to enable CO desorption. On the other hand, in the catalyst with the Fe_2N core (Fe_2N@Fe-N_4-C), an overpotential of 0.19 V is required for CO_2 adsorption, but the adsorbed CO can leave more easily the catalyst surface. Following the same reasoning, HER is not favored on the Fe_2N@Fe-N_4-C catalyst (see Figure 68).

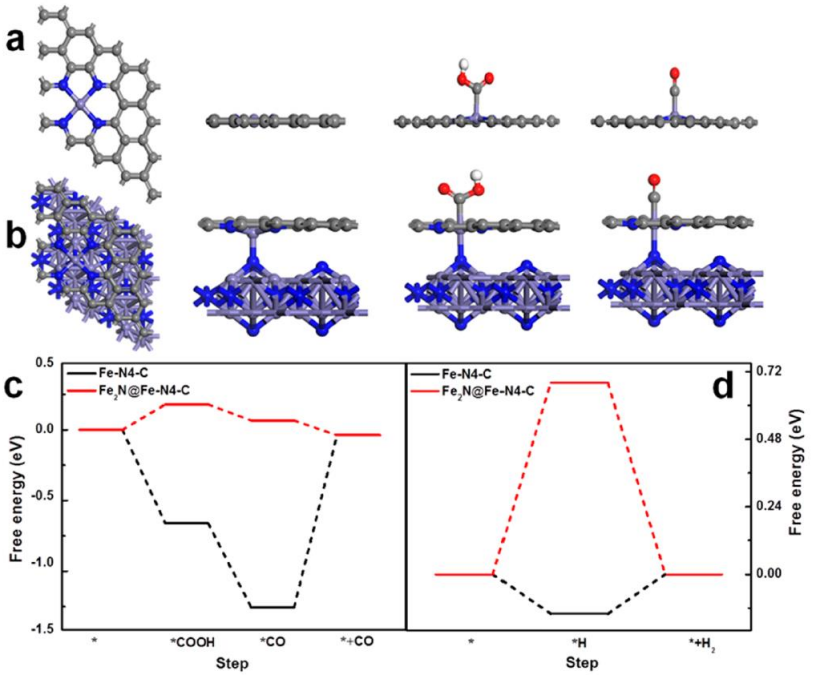

Figure 68. *Visual representation of the CO_2RR processes on Fe−N_4−C (a) and encapsulated Fe_2N@Fe-N_4-C (b). In (c) and (d) the corresponding free-energy profiles of CO_2RR and HER are reported. Reprinted with permission from (Cheng Q., K. Mao, L. Ma, L. Yang, L. Zou, Z. Zou, Z. Hu and H. Yang (2018c) Encapsulation of Iron Nitride by Fe−N−C Shell Enabling Highly Efficient Electroreduction of CO_2 to CO. ACS Energy Lett., **3**, 1205-1211). Copyright (2021) American Chemical Society*

In general, understanding the chemistry of the active sites and the origin of the high CO_2RR activity of these Fe–N_x–C catalysts remains a source of scientific interest due to their complexity deriving from high-temperature treatments. For instance, Pan F. et al. (2018a) synthesized a Fe-N-C catalyst with a low onset potential of -0.29 V *vs.RHE* and explained its high performance through the presence of edge hosted Fe-N_{2+2}−C_8 moieties bridging two armchair-like graphitic layers as active sites for CO_2RR to CO instead of the traditionally proposed Fe–N_4–C_{10} sites anchored on a compact carbon plane, as clarified in Figure 69. The easier occurrence of the CO_2RR is due to the presence of both Fe centers and C atoms with dangling bonds next to N, which adsorb CO*and OH* intermediates respectively, hence leading to the cleavage of the C–O bonding.

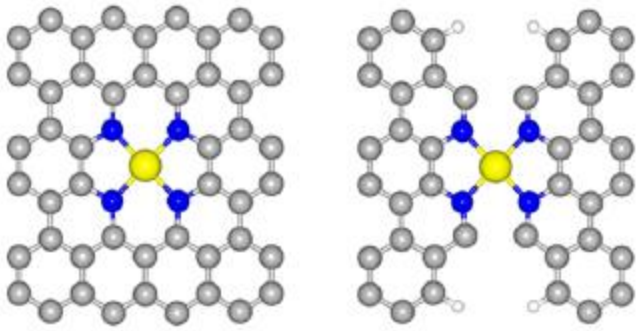

Figure 69. *Visual representation of the chemical structure of Fe–N_4–C_{10}, on the left side, and Fe-N_{2+2}−C_8, on the right side. The yellow, blue and grey spheres in the scheme represent iron, nitrogen and carbon atoms, respectively. Reprinted with permission from (Pan F., H. G. Zhang, K. X. Liu, D. Cullen, K. More, M. Y. Wang, Z. X. Feng, G. F. Wang, G. Wu and Y. Li (2018a) Unveiling active sites of CO_2 reduction on nitrogen-coordinated and atomically dispersed iron and cobalt catalysts. ACS Catal., **8**, 3116-3122). Copyright (2021) American Chemical Society*

Another important issue is not only to identify the active sites but also to guarantee a high exposure of them on the surface support. In the study by Ye et al. (2017), through functionalization of the surface of zeolitic imidazolate framework-8 (ZIF-8) with ammonium ferric citrate (AFC), isolated Fe-N sites were formed on the surface of the catalyst (named as C-AFC©ZIF-8) obtained after a 4-hours pyrolysis treatment under Ar atmosphere at 900 °C and acid leaching (see Figure 70). In comparison with the C-AFC@ZIF-8 catalyst, obtained by means of bulk functionalization of ZIF-8 with AFC, C-AFC©ZIF-8 exhibited much higher catalytic activity in virtue of its highly exposed Fe-N active sites on the surface support. In particular, the maximum CO Faradaic efficiency of C-AFC©ZIF-8 is 93.0% at −0.43 V *vs.RHE* (versus the CO FE of 84 % at the same potential for C-AFC@ZIF-8) and the total current density reaches its maximum value of around 23 mA/cm^2 at -0.85 V *vs.RHE* (versus the value of around 12 mA/cm^2 at the same potential for C-AFC@ZIF-8) and at the maximum iron content of 1.47 %, suggesting the importance of the Fe-N active sites for the catalysis of CO_2RR.

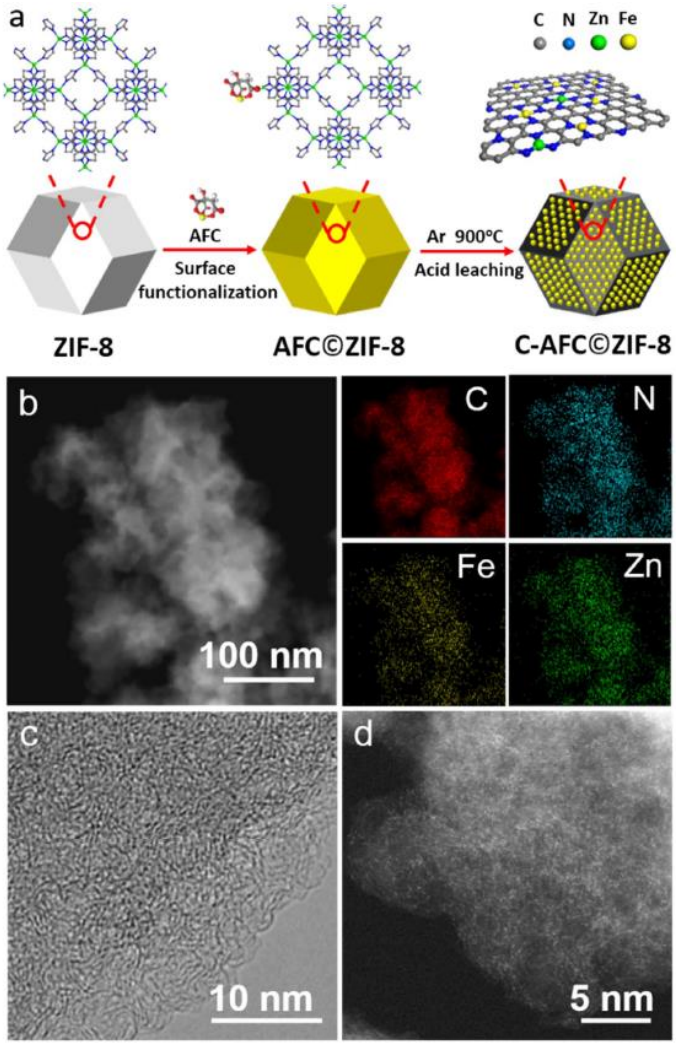

Figure 70. *(a) Scheme of the synthesis process of C-AFC©ZIF-8. (b) HADDF-STEM image and the corresponding EDX maps for C, N, Fe, Zn atoms of C-AFC©ZIF-8. (c) High resolution TEM and (d) High resolution HADDF-STEM image of C-AFC©ZIF-8. Reprinted with permission from (Ye Y. F., F. Cai, H. B. Li, H. H. Wu, G. X. Wang, Y. S. Li, S. Miao, S. H. Xie, R. Si, J. Wang and X. H. Bao (2017) Surface functionalization of ZIF-8 with ammonium ferric citrate toward high exposure of Fe-N active sites for efficient oxygen and carbon dioxide electroreduction. Nano Energy, **38**, 281-289). Copyright (2021) Elsevier.*

Wu et al. (2020) synthesized a Fe-N-C catalyst with highly exposed Fe-N_x active sites through pyrolysis of a 3D sea urchin-like FeOOH-polyaniline (FeOOH-PANI) precursor which also guaranteed large specific surface and electrochemically active surface areas (see Figures 71 and 72). The prepared catalyst achieved a high CO FE of 95% with CO partial current density of 1.9 mA/cm^2 at an overpotential of 530 mV.

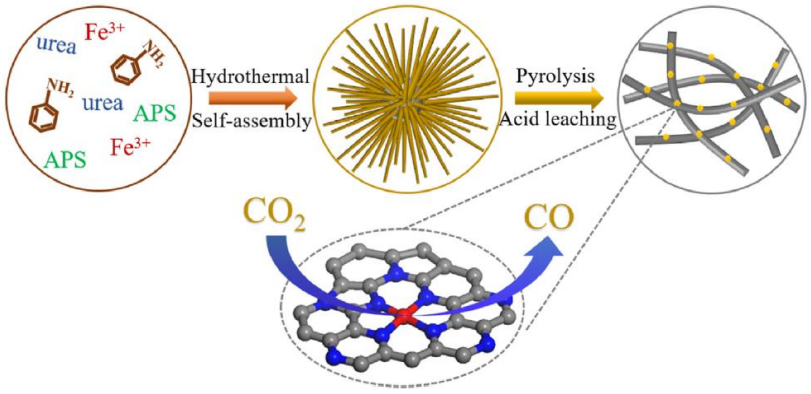

Figure 71. *Scheme of the synthesis of Fe-N-C. Ammonium persulfate (APS), iron(III) chloride hexahydrate, urea and aniline were adopted for the hydrothermal synthesis of the FeOOH-PANI precursor. Reprinted with permission from (Wu S., X. Lv, D. Ping, G. Zhang, S. Wang, H. Wang, X. Yang, D. Guo and S. Fang (2020) Highly exposed atomic Fe–N active sites within carbon nanorods towards electrocatalytic reduction of CO_2 to CO. Electrochim. Acta,* ***340,*** *135930). Copyright (2021) Elsevier*

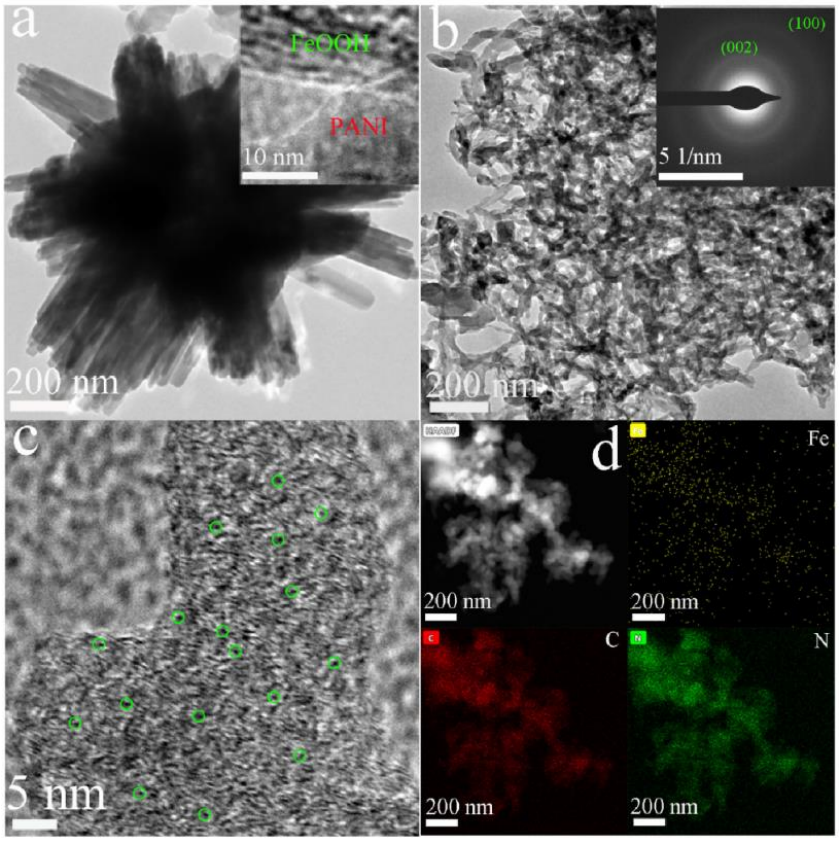

Figure 72. *TEM image of the FeOOH-PANI intermediate (a), the TEM image(b), the high-resolution TEM image (c) and the STEM image with corresponding EDX maps (d) of the FeeNeC catalyst. The inset of Figure (b) represents the SAED patterns of the Fe-N-C catalyst. Single Fe atoms are evidenced with green circles. Reprinted with permission from (Wu S., X. Lv, D. Ping, G. Zhang, S. Wang, H. Wang, X. Yang, D. Guo and S. Fang (2020) Highly exposed atomic Fe–N active sites within carbon nanorods towards electrocatalytic reduction of CO_2 to CO. Electrochim. Acta,* ***340,*** *135930). Copyright (2021) Elsevier*

Recently, similarly to Ni and Co SACs, Fe-based single atom catalysts have been also explored as effective catalysts for the syngas electro-production from CO_2 in aqueous solution. Zhao et al. (2020) prepared a Fe-N-C electrocatalyst from iron chloride and urea-formaldehyde resin through pyrolysis at different temperatures and Fe contents. At optimal carbonization temperature and Fe metallic content of 950 °C and 3%, respectively, and by varying the applied potential in the range between −0.6 V *vs.RHE* to −1.0 V *vs.RHE*, the H_2/CO ratio of the obtained syngas varies from 4 to 1/3, as

shown in Figure 73. This is, indeed, a relatively wide range when compared with the one of noble metal-based catalyst and other M-N-C catalysts.

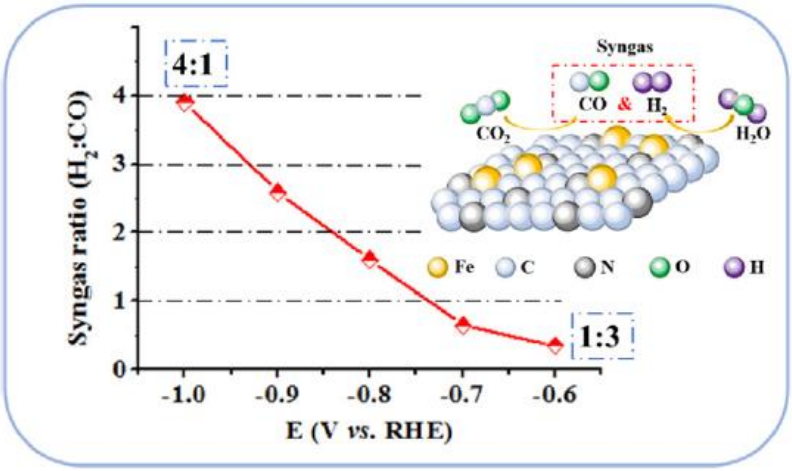

Figure 73. *Plot of H_2/CO ratio versus applied potential vs.RHE for the Fe-N-C catalyst. The inset reports a schematic representation of the catalyst surface. Reprinted with permission from (Zhao J., J. Deng, J. Han, S. Imhanria, K. Chen and W. Wang (2020) Effective tunable syngas generation via CO_2 reduction reaction by non-precious Fe-N-C electrocatalyst. Chem. Eng. J., **389**, 124323). Copyright (2021) Elsevier*

Huan et al. (2017) synthesized Fe-N-C electrocatalysts (named $Fe_{4.0}$d, $Fe_{1.0}$w, $Fe_{1.0}$d, $Fe_{0.5}$d, and $Fe_{0.5}$d-950 according to the different synthesis conditions) with different proportions of Fe single atom centers and Fe nanoparticles. The Fe-N_4 active centers catalyzed the CO production, whereas Fe NPs mainly favored HER (as outlined in Figure 74). Therefore, by varying the Fe-N_4 active centers' percentage from 0 to 100%, syngas with a CO/H_2 ratio in the range between around 0.2 and 4 could be obtained.

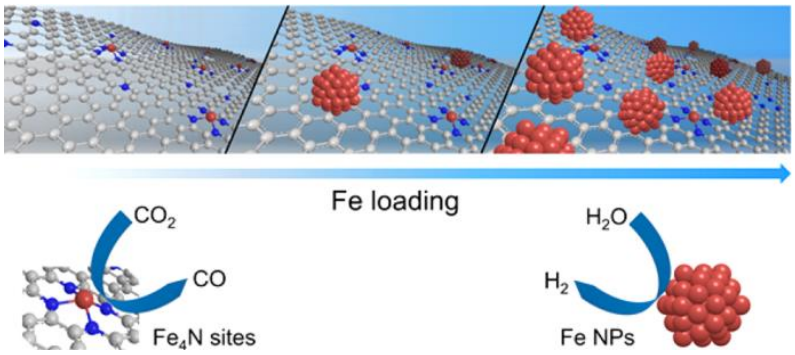

Figure 74. *Schematic representation of the role of Fe-based catalyst in catalyzing either HER or CO_2RR to CO as Fe loading on the carbon support changes. Reprinted with permission from (Huan T. N., N. Ranjbar, G. Rousse, M. Sougrati, A. Zitolo, V. Mougel, F. Jaouen and M. Fontecave (2017) Electrochemical Reduction of CO_2 Catalyzed by Fe-N-C Materials: A Structure−Selectivity Study. ACS Catal., 7, 1520-1525). Copyright (2021) American Chemical Society*

3.3.4 Other metal-based Single Atom Catalysts

According to recent studies, Zn single atoms and Sn single atoms coordinated with N showed high activity and selectivity towards CO_2RR to CO. Zhao et al. (2018) prepared Sn single atoms dispersed on pyridinic N-doped carbon nanofibers (AD-Sn/N-C1000) through electrospinning and pyrolysis at 1000 °C. Figure 75 reports the STEM, HAADF-STEM and EDS images of the as-synthesized catalyst. Unlike Sn NPs on N-doped nanofibers, which exhibited a 62 % FE towards formate, the AD-Sn/N-C1000 catalyst showed a CO Faradaic efficiency of 91% at an overpotential of 490 mV.

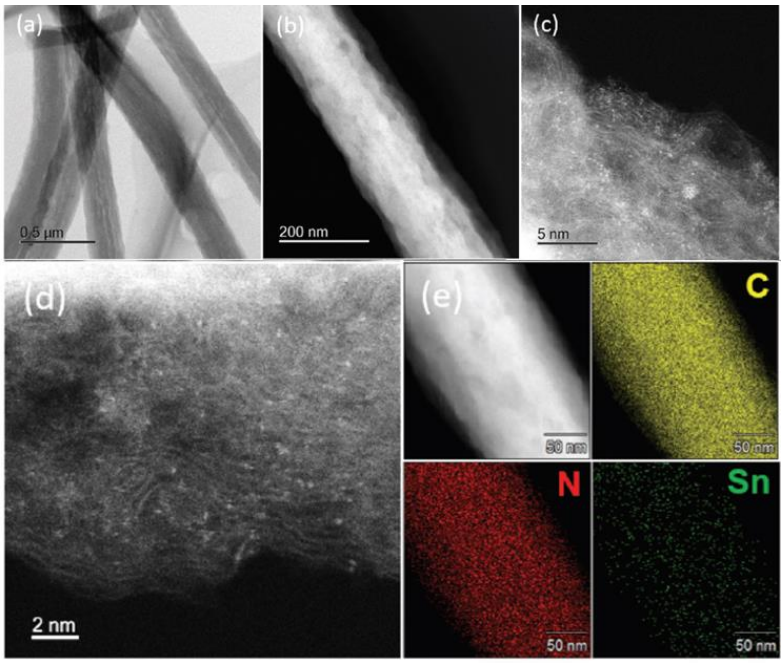

Figure 75. *(a) STEM image of the AD-Sn/N-C1000 catalyst; (b),(c) and (d) HAADF–STEM images of AD-Sn/N-C1000 at scale bars of 200nm, 5nm and 2 nm; (e) corresponding EDS maps with C, N and Sn atoms. Reprinted with permission from (Zhao Y., J. J. Liang, C. Y. Wang, J. M. Ma and G. G. Wallace (2018) Tunable and efficient tin modified nitrogen-doped carbon nanofibers for electrochemical reduction of aqueous carbon dioxide. Adv. Energy Mater., **8**, 1702524-1702535). Copyright (2021) John Wiley and Sons*

On the other hand, Yang F. et al. (2018) produced a cost-effective Zn-N-C type catalyst with atomically dispersed Zn coordinated with N atoms forming Zn-N_4 active sites (ZnN_x/C). The catalyst was tested in a CO_2-saturated, 0.5 M $KHCO_3$ solution, showing high catalytic performance for CO_2RR to CO, such as a low onset potential of 0.13 V, a CO FE of 95% at 0.43 V *vs.RHE* and high stability without significant current losses for 75 hours of test. DFT calculations confirmed that the high activity of ZnN_x/C can be attributed to a synergistic effect between Zn and N atoms in the Zn-N_4 active centers, which is responsible for reducing the energy barrier for the formation of the COOH* intermediate. Figure 76a schematizes the proposed reaction pathway of the CO_2 molecule on the Zn-N_4 active site, while in Figure 76b, the free energy evolution with reaction coordinate of the catalyst is compared with the ones with ZnC_4 and N_4/C as active centers.

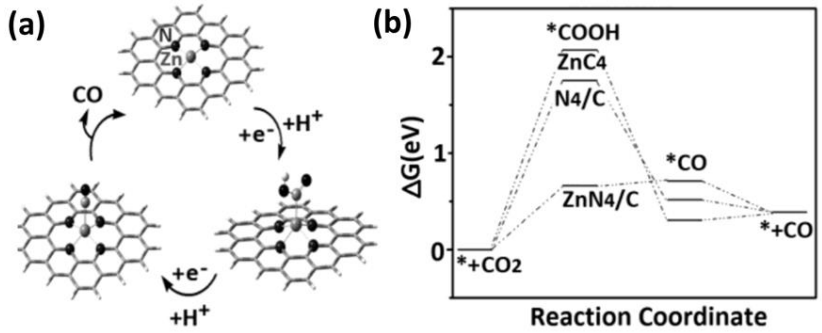

Figure 76. *The proposed reaction pathway for the CO2RR to CO on the Zn-N4 moiety (a) and the free energy diagrams for this reaction on ZnN_4/C, N_4/C and ZnC_4. Reprinted with permission from (Yang F., P. Song, X. Z. Liu, B. B. Mei, W. Xing, Z. Jiang, L. Gu and W. L. Xu (2018) Highly efficient CO_2 electroreduction on ZnN_4-based single-atom catalyst. Angew. Chem. Int. Ed., **57**, 12303-12307). Copyright (2021) John Wiley and Sons*

Copper is typically adopted in its bulk form as an effective catalyst for the CO_2 electro-reduction to high-molecular products such as alcohols and hydrocarbons. However, recently it has been proved that Cu as single atoms can selectively catalyze the CO formation. For instance, Xu et al. (2020) proposed the synthesis, through a two-step pyrolysis method, of single Cu atoms embedded in 2D N-doped graphene support (named as Cu–N_4–NG). HAADF-STEM images in Figure 77 confirmed the existence of Cu single atoms on the support. In contrast with the Cu particles-based catalyst, which exhibited relatively low selectivity towards CO in favor of H_2 generation, Cu–N_4–NG favors CO generation, as can be deduced from DFT calculations (see Figure 78). Moreover, electrochemical tests confirmed that Cu–N_4–NG exhibited a much higher CO Faradaic efficiency of 80.6 % at −1.0 V *vs.RHE*. This is mainly due to the presence of Cu–N_4 sites which highly facilitated the CO_2 activation step, whereas the graphene substrate promoted water dissociation which provides protons involved in the CO_2RR process. N-doped graphene-supported Cu particles

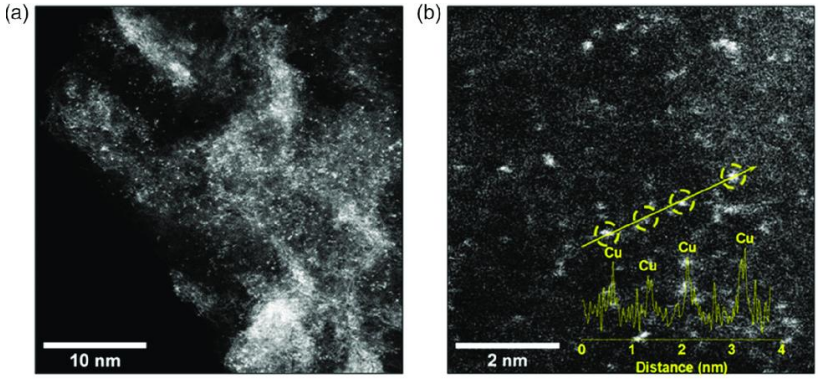

Figure 77. *(a) HAADF-STEM image of Cu–N_4–NG. (b) Hugh magnification HAADF-STEM image of Cu–N_4–NG. In the inset, a line profile along the arrow direction is reported, with Cu atoms evidenced by yellow circles. Reprinted with permission from (Xu, C., X. Zhi, A. Vasileff, D. Wang, B. Jin, Y. Jiao, Y. Zheng and S. Z. Qiao (2020) Highly Selective Two-Electron Electrocatalytic CO_2 Reduction on Single-Atom Cu Catalysts. Small Structures, **2**, 2000058). Copyright (2021) John Wiley and Sons*

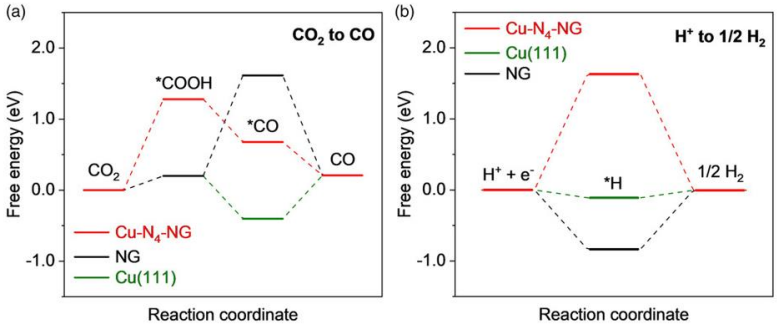

Figure 78. *Free energy diagrams versus reaction coordinate for (a) the CO_2RR to CO and (b) the HER on Cu-N_4-NG, NG and Cu (111) (i.e. Cu-NG) catalyst. Reprinted with permission from Xu, C., X. Zhi, A. Vasileff, D. Wang, B. Jin, Y. Jiao, Y. Zheng and S. Z. Qiao (2020) Highly Selective Two-Electron Electrocatalytic CO_2 Reduction on Single-Atom Cu Catalysts. Small Structures, **2**, 2000058). Copyright (2021) John Wiley and Sons*

Cheng et al. (2021) confirmed the effectiveness of the Cu-N_4 site for the catalysis of the CO_2RR to CO since it can guarantee an appropriate binding energy strength of COOH*and CO* intermediates and, therefore, boost CO generation. In particular, the authors successfully synthesized Cu single atoms dispersed on a N-C support through a MOF-assisted method. The

synthesis is schematized in Figure 79a. The Cu/Zn-ZIF was firstly prepared starting from a mixture of $Zn(NO_3)_2 \cdot 6H_2O$ and $Cu(OAc)2 \cdot H_2O$ in methanol (MeOH) through in situ incorporation of Cu^{2+} ions into a ZIF-8 framework, which partially replaced Zn^{2+} nodes to coordinate with 2-methylimidazole (2-MeIm). After pyrolysis under Ar atmosphere for 3 hours at various temperatures (800, 900, 1000, and 1100 °C), the catalyst was obtained. The catalyst obtained at 1110 °C, named as Cu-N_4-C/1100, was selected as the best one among the synthesized ones. SEM and TEM images, EDS maps, HRTEM and HAADF-STEM images and SAED pattern confirmed the nature of single Cu atoms homogeneously dispersed on N-C nanoparticles which inherited the rhombododecahedral shape of ZIF-8 (see Figures 79b-g). In the electrochemical tests, the catalyst achieved a maximum CO Faradaic Efficiency of 98 % at -0.9 V *vs.RHE* and high stability for at least 40 hours of test, proving its high performance.

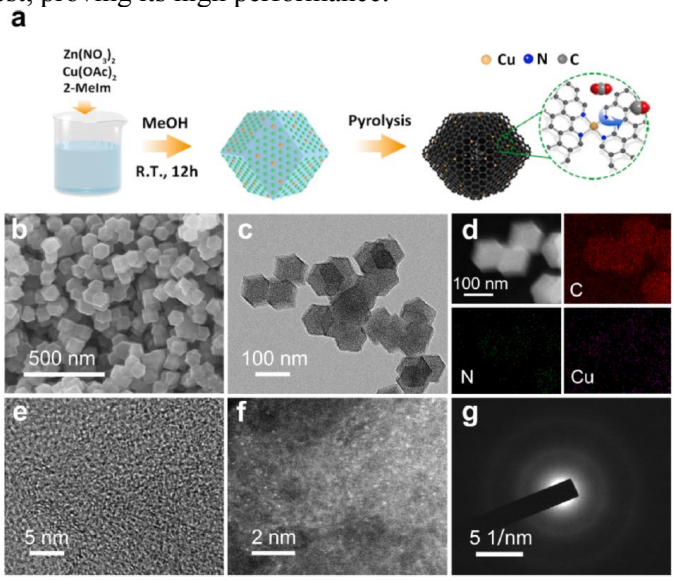

Figure 79. *(a) Scheme of the synthesis procedure for Cu-Nx-C/T. (b) SEM image, (c) TEM and (d) the corresponding EDS maps of Cu-N_4-C/1100. (e) HRTEM images, (f)HAADF-STEM images and (g) SAED pattern of the aforementioned catalyst. Reprinted with permission from (Cheng H., X. Wu, X. Li, X. Nie, S. Fan, M. Feng, Z. Fan, M. Tan, Y. Chen and G. He (2021) Construction of atomically dispersed Cu-N_4 sites via engineered coordination environment for high-efficient CO_2 electroreduction. Chem. Eng. J., **407**, 126842). Copyright (2021) Elsevier*

Chen et al. (2021) prepared Cu single atoms on a nitrogenated carbon-based catalyst (named as Cu-N-C). The Cu-N_3 sites of the catalyst were proved to highly promote the *CO desorption. Indeed, in a gas-tight H-type cell, Cu-N-C reached a high CO faradaic efficiency of 98 % at −0.67 V *vs.RHE* and high durability (Faradaic Efficiency remains above 90% over 20 hours of tests). The same catalyst was also tested in an electrolyte flow cell configuration, exhibiting an even higher CO Faradaic Efficiency of 99.9 % at -0.67 V *vs.RHE* due to the boosted rate of CO_2 diffusion.

DFT calculations revealed the reason for the improved performance of the catalyst: the Cu–N_3 site is located on an extended carbon plane with six nitrogen vacancies which stabilize the active site, while three unoccupied N sites are spontaneously saturated by protons during the CO_2RR. Therefore, the hydrogen bonds formed between the O atom of *COOH and the H atom of adjacent protons contribute to dramatically reducing the energy barrier of *COOH formation. After the first proton-coupled electron transfer process, the hydrogen bond disappears and the adsorbed *CO species are easily released, hence guaranteeing the CO production.

Pan F. et al. (2018b) synthesized, other than Ni, Fe and Co-based SACs, also Mn-N-C and Cr-N-C catalysts through pyrolysis of a solid obtained by drying a water mixture of urea, citric acid and metal precursor. The Mn-based and Co-based single atom catalysts exhibited comparable maximum CO FE (72% and 70% respectively), while the overpotential of Mn-N-C required for reaching the maximum CO selectivity was 260 mV lower than the one of Cr-N-C. Anyhow, it can be observed that both Mn and Cr showed lower catalytic performance towards CO formation compared to single atom catalysts such as Ni and Fe, as shown in Figure 80.

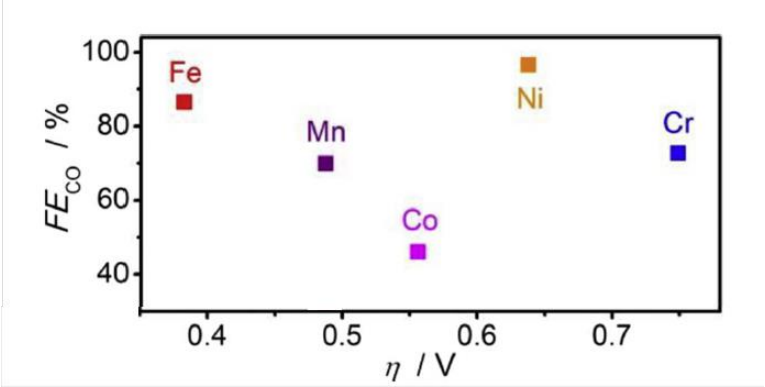

Figure 80. *Maximum CO Faradaic efficiencies versus applied potential for five different M-N-C catalysts, with M=Fe, Mn, Co, Ni and Cr. Reprinted with permission from (Pan F., W. Deng, C. Justiniano and Y. Li (2018b) Identification of champion transition metals centers in metal and nitrogen-codoped carbon catalysts for CO_2 reduction. Appl. Catal. B Environ., **226**, 463-472). Copyright (2021) Elsevier*

Manganese was also the key element in the catalyst prepared by Feng et al. (2020). Instead of a Mn-N_4-based structure embedded in graphene support, the authors proposed the synthesis of a more efficient catalyst consisting of Mn-N_3 sites embedded in graphitic carbon nitride (g-C_3N_4) on carbon nanotubes (named as Mn–C_3N_4/CNT). DFT calculations proved that the unusual Mn-N_3 site is responsible for a higher performance of the catalyst by favoring the formation of the COOH* intermediate much more than the typical Mn-N_4-G catalyst (see Figure 81). Indeed, Mn–C_3N_4/CNT exhibited a 98.8% CO Faradaic efficiency with a CO partial current density of 14.0 mA/cm^2 at a low overpotential of 0.44 V *vs.RHE*. in aqueous electrolyte, outperforming all the Mn-N_4-based SACs previously reported in the literature.

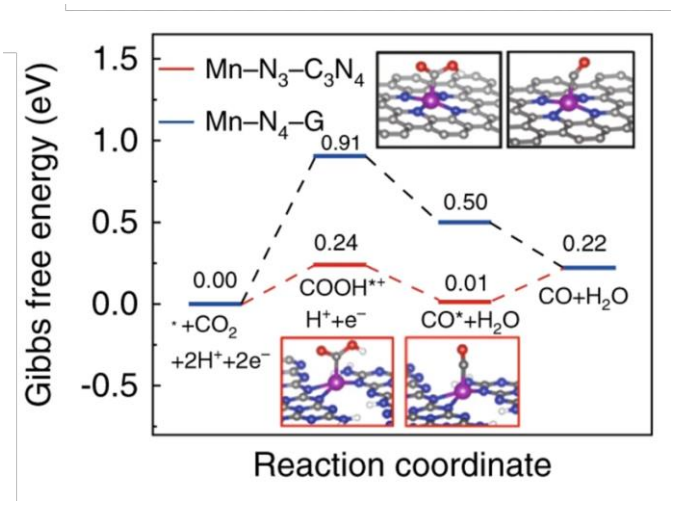

Figure 81. *Gibbs free energies associated to the reaction steps of CO_2RR to CO for Mn–N_3–C_3N_4 and Mn–N_4-G. The diagram evidences the superiority of the Mn–N_3–C_3N_4 over the Mn–N_4-G, since the former requires less energy than the latter for the COOH* formation (i.e. the rate limiting step of the reaction). Reprinted with permission from (Feng J., H. Gao, L. Zheng, Z. Chen, S. Zheng, C. Jiang, H. Dong, L. Liu, S. Zhang and X. Zhang (2020) A Mn-N_3 single-atom catalyst embedded in graphitic carbon nitride for efficient CO_2 electroreduction. Nat. Commun., **11**, 4341). Copyright (2021) Nature Research*

Starting from the idea of reducing the amount of Pd in Pd-based nanostructured catalysts for the CO_2RR, He et al. (2020b) prepared a N-doped carbon-supported Pd SAC (named as Pd-NC) with a low Pd loading of 2.95 wt% (indeed, as the authors stated, the commonly adopted Pd loading for this kind of catalysts is of around 10 wt%).

Through several characterization techniques as well as by means of DFT calculations, the authors revealed the unique coordination nature of Pd atoms with N atoms in Pd-N_4 active centers which helps stabilize and activate the adsorbed CO_2, hence guaranteeing CO generation at low overpotentials. In comparison with commercial palladium on carbon (Pd/C), which shows high selectivity towards HER, the Pd-NC exhibited a moderate selectivity also towards CO_2RR to CO, with a CO Faradaic efficiency of 55% at -0.50 V *vs.RHE* (see Figure 82).

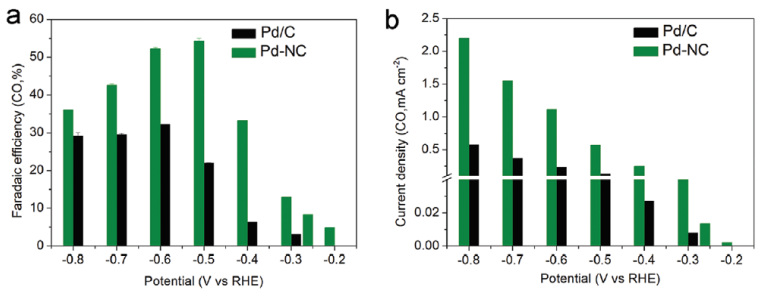

Figure 82. *(a) CO Faradaic efficiencies and (b) partial current densities of CO at several applied potentials for both Pd/C (black) and Pd-NC (green) catalysts. Reprinted with permission from (He Q., J. H. Lee, D. Liu, Y. Liu, Z. Lin, Z. Xie, S. Hwang, S. Kattel, L. Song and J. G. Chen (2020b) Accelerating CO_2 Electroreduction to CO Over Pd Single-Atom Catalyst. Adv. Funct. Mater., **30**, 2000407Copyright (2021) John Wiley and Sons*

A more recent and novel approach is to develop catalysts whose active sites consist of two, three adjacent atoms or a-few-atom sub-nanoclusters which can show a comparable or even better catalytic activity compared with single atom catalysts. For instance, as for the CO production from CO_2 electro-reduction reaction, Li et al. (2002) reported the synthesis of a dual-atom Ag_2/graphene catalyst (Ag_2-G) for CO_2 electrochemical reduction to CO: starting from graphene oxide (GO) and binuclear Ag complex ({[Ag(NO3-O)(phtz-N)]2(μ-phtz-N,N′)2}), a mixture of these two compounds was obtained in dimethyl sulfoxide (DMSO), followed by lyophilization of the product of centrifugation and its subsequent annealing at 550 °C for 2 hours under N_2 flow (see Figure 83).

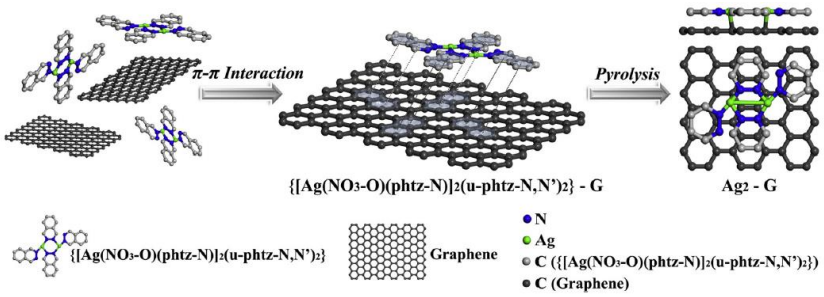

Figure 83. *Scheme of the synthesis of dual-atom Ag_2-G catalyst. Reprinted with permission from (Li Y., C. Chen, R. Cao, Z. Pan, H. He and K. Zhou (2020) Dual-atom Ag_2/graphene catalyst for efficient electroreduction of CO_2 to CO. Appl. Catal. B Environ., **268**, 118747). Copyright (2021) Elsevier*

The Ag_2-G active site consists of two adjacent Ag atoms, each of them coordinated with three nitrogen atoms, and the AgN_3-AgN_3 sites are linked to the graphene matrix through strong Ag-C bonds. While CO_2 interacts with the Ag single atom of Ag-N_4 sites in the more conventional Ag_1-G catalyst (i.e. single Ag catalyst) only with its carbon atom, both the carbon and the oxygen atoms of carbon dioxide interact at once with the two Ag atoms of AgN_3-AgN_3 sites in Ag_2-G, which makes the reaction intermediates on the latter catalyst more stable (as shown in the diagram in Figure 84). Consequently, Ag_2-G showed high CO_2RR to CO performance, such as a low onset potential of -0.25 V *vs. RHE*, a high CO FE up to 93.4 % with a current density of 11.87 mA/cm^2 at -0.7 V *vs.RHE* as well as stability for 36 hours of tests, hence proving its superiority on the single atom Ag_1/graphene and the traditional Ag NPs.

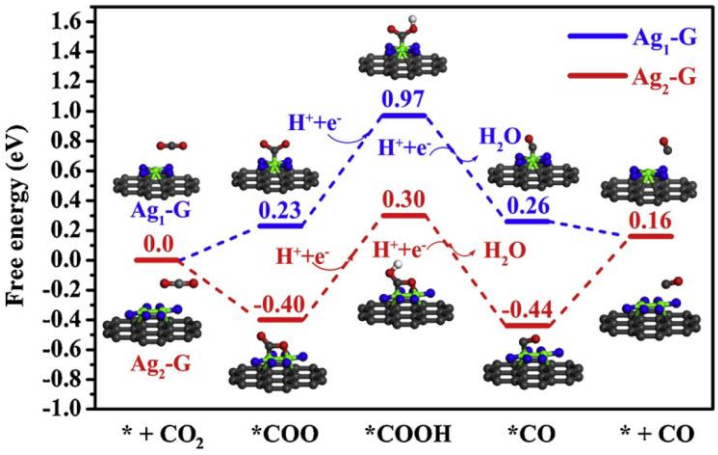

Figure 84. *Free energy values related to the CO_2RRto CO reaction pathways for both single atom Ag_1-G and dual atom Ag_2-G. Reprinted with permission from (Li Y., C. Chen, R. Cao, Z. Pan, H. He and K. Zhou (2020) Dual-atom Ag_2/graphene catalyst for efficient electroreduction of CO_2 to CO. Appl. Catal. B Environ., **268**, 118747). Copyright (2021) Elsevier*

3.4 Summary and future perspectives

In summary, metals such as Ni, Fe, Co, Zn, etc. in the form of single atom catalysts, especially bound to N through either covalent bonds or coordination bonds, and embedded in a conductive support have been tested and found as valuable and effective approaches to reduce CO_2 and produce syngas:

1) First of all, they are more economical than traditional Au and Ag-based nanostructured catalysts, consisting of lower quantities of more readily available and low-cost metals dispersed on low-cost and highly conductive supports such as carbon-based materials. A cost/power analysis, performed on a CO_2 plant fed with 13750 tons/day of CO_2 and producing syngas, revealed that when adopting M-N-C catalysts rather than Ag-based catalysts, in a flow-cell, less power is required for the reactions to occur (Delafontaine et al., 2020).

2) At the same time, they are highly active towards CO_2RR due to their unique characteristics, which distinguish them from their nanoparticle-based counterparts: low-coordination state and homogeneity of catalytically active sites with maximum metal utilization efficiency i.e. all the catalytic active sites of the metal are exposed to the reactants.

3) Finally, these catalysts exhibit a higher selectivity towards CO_2RR to CO than towards HER, when compared with their nano-sized counterparts,

as a consequence of the nature of their active sites. Indeed, the metal single atoms are often organized in the form of M-N_x active sites (where M= metal), on which chemisorption of atomic hydrogen is not favored because: (i) the adsorption step of H^+ ions require higher energy (typically, a 0.3 eV penalty is recorded for the formation of H_{ads}) and (ii) HER proceeds through a Volmer-Heyrovsky mechanism rather than through a faster Volmer-Tafel one (Bagger et al., 2017; Hu et al., 2018). Furthermore, nitrogen atoms not only contribute to increasing activity and selectivity of the transition metals single atoms but nitrogen incorporation into a carbon matrix can also play an effective role in stabilizing the highly energetic single atoms through coordination bonds, avoiding their aggregation (Kim et al., 2014).

4) Moreover, with the aim of producing syngas, the CO/H_2 ratio can be tuned in a wide range not only by varying the type and morphology of metals and supports but also by changing the size of the active phase, for instance by reaching a definite proportion of HER-active nanoparticles and CO_2RR-active single atoms, which corresponds to a precise syngas ratio (Zhu Y. et al., 2020).

However, there are still some challenges to overcome for further development and scale-up of these catalysts. New routes can be and need to be explored for the development of more efficient catalysts with lower onset potentials and higher current densities at ambient conditions.

Firstly, not only new metals should be explored in monometallic SACs but, also and above all, more focus should be placed on the development of multimetallic SACs which are expected to show improved catalytic activity in virtue of novel synergistic mechanisms generated by the interaction between different metals, as it happens for the nano-sized counterparts (Kim et al., 2014; Clark et al., 2017). In addition, the combination of different metals with a non-metal, also different form N, is a further route, which can lead to lowered overpotential for CO formation as a consequence of a bi-functional effect obtained by combining atoms of different metals, i.e. atoms with different binding energies towards the COOH* and H* intermediates. Indeed, an efficient catalyst for CO_2RR to CO must be able to stabilize COOH* without stabilizing CO* by a similar amount (Figure 85), as it naturally occurs with enzymes which possess two different functional sites: one of them bonds the C-end of CO* and COOH*, while the other one can stabilize the O group in COOH* favoring the C-O cleavage (Hansen et al., 2013).

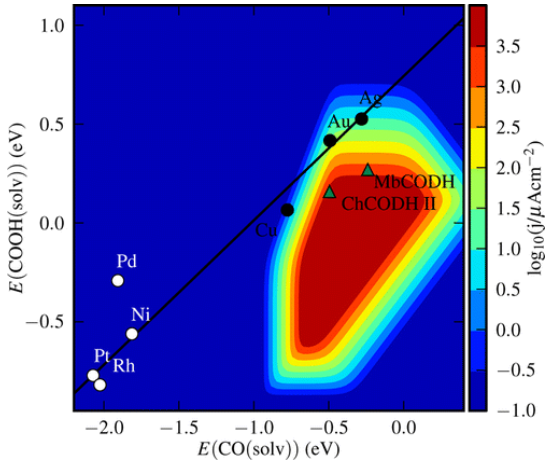

Figure 85. *Kinetic volcano plot for the CO evolution at a 0.35 V overpotential on different transition metals. It shows that on transition metals the weaker is the CO adsorption on the catalyst, i.e., the higher the CO rate production is, the weaker is, however, also the COOH* adsorption on the catalyst itself, which means that higher overpotential will be needed to guarantee the starting of the CO evolution reaction. Enzymes such as MbCODH and ChCODH II do not obey to this linear relationship, showing superior CO_2RR activity at low overpotentials. Reprinted with permission from (Hansen H. A., J. B. Varley, A. A. Peterson and J. K. Nørskov (2013) Understanding Trends in the Electrocatalytic Activity of Metals and Enzymes for CO_2 Reduction to CO. J. Phys. Chem. Lett., **4**, 388-394). Copyright (2021) American Chemical Society*

Furthermore, the majority of the thus far reported studies focus on testing the electrochemical performance of the catalysts in a batch-type H-cell configuration. In this case, scaled-up conditions are not reproducible due to inefficient mass transport phenomena, poor mixing, additional losses due to membrane resistance, and very low current densities. In order to verify the effectiveness of the catalysts on a scaled-up electrochemical environment, flow-reactors such as membrane reactors and microfluidic reactors should be adopted for tests, along with incorporating the catalyst within GDE in order to solve the CO_2 solubility limitations, thus fart adopted in a few cases (Yang et al., 2020; Möller et., 2019).

Moreover, further attention should be paid to the choice of the support and to the study of its influence on the catalysis of the atomic centers dispersed on it. Currently, most of the developed SACs for CO_2RR are supported on carbon-based materials such as graphene-based materials and carbon nanotubes. However, many other supports could be analyzed and compared, such as oxides, nitrides, and transition metal dichalcogenides.

Moreover, defects, either natural or artificially created, could work as anchoring sites to stabilize single atoms, enabling higher metal loadings and avoiding agglomeration, which is another critical issue for SACs. In particular, among defects, cation and anion vacancies are the most adopted to guarantee the anchorage of metal single atoms to metal compounds-based supports. More specifically, metal oxides can use their cation vacancies as anchoring sites. For instance, $Ni(OH)_2$ has been recently used to anchor Pt single atoms through Ni^{2+} vacancies (Zhang J. et al., 2018), TiO_2 single-crystal nanosheets were doped with Rh atoms by means of Ti^{4+} centers (Ida et al., 2015) and Al_2O_3 bonded Pt clusters through coordinatively unsaturated pentacoordinate Al^{3+} centers (Kwak et al., 2009). Deng et al. (2015) prepared, through a one-pot chemical method which adopts $(NH_4)_6Mo_7O_{24}$, H_2PtCl_6, and CS_2 as precursors, isolated Pt atoms anchored on few-layer MoS_2 nanosheets as an efficient catalyst for the HER. HAADF-STEM results highlighted that the single Pt atoms substitute some of the Mo atoms. As previously mentioned, anions vacancies represent a second type of anchoring site. For instance, oxygen vacancies can be formed in metal oxides, as in TiO_2 nanosheets for the stabilization of Au single atoms (Wan et al., 2018). Another type of anion vacancy is the sulfur vacancy, which can be obtained by the chemical exfoliation of transition metal chalcogenides such as MoS_2. Liu G. et al. (2017) synthesized Co single atoms dispersed on MoS_2 monolayers by firstly chemically exfoliating bulk MoS_2 and then mixing these sheets with thiourea-based Co species via sulfur vacancies. The authors observed that the strong covalent bonds between Co atoms and sulfur vacancies of MoS_2 are the main reason for the high activity, stability, and selectivity of the catalyst towards hydrodeoxygenation reaction. Although many studies have been performed, and many other interesting perspectives suggested, these materials have never been tested for the CO_2RR to CO or for the syngas electro-production. This could be a trigger for the future development of more performing SACs towards these reactions

Chapter 4:
New nano-structured catalyst for the electro-reduction of CO_2 and H_2O to syngas

4.1 Introduction

In the following chapter, the synthesis of a new M-N-C type single atoms-based catalyst for the electro-reduction of CO_2 and H_2O to syngas is reported.

As mentioned in the previous chapter, one of the keys for further advancements in the research for more effective catalysts for this reaction could be the design and the development of multimetallic SACs, which are expected to show improved catalytic activity due, for instance, to novel synergistic mechanisms generated by the interaction between different metals, as it happens for the nano-sized counterparts (Kim et al., 2014; Clark et al., 2017). Currently, only a few examples can be found in this direction (Cheng et al., 2018). In particular, Ren et al. (2019) synthesized a bi-atomic nickel and iron–nitrogen, carbon-based catalyst (Ni/Fe-N-C) for CO production through an ion-exchange strategy based on the pyrolysis of a Zn/Ni/Fe zeolitic imidazolate framework. Experimental results and DFT calculations revealed that the Ni/Fe-N dual-site works according to a different mechanism. It lowers the energy barrier for both the formation of the COOH* intermediate and the desorption of CO* when a previous CO* is already present on the active site, leading to superior CO_2RR activity. On the other hand, and with the primary aim of producing syngas, He et al. (2020) explored the catalytic activity of both Ni and Co single atoms dispersed on N-doped carbons (TM-NC with TM=Co and/or Ni), founding that the Ni-NC catalyst is active towards CO_2RR to CO evolution (>56 mA/cm^2 at −1.0 V *vs.RHE*), whereas the Co-NC catalyst exhibits a favorable HER activity (>58 mA/cm^2 at −1.0 V *vs.RHE*). On the basis of that, the authors synthesized single-atom catalysts, including Co and Ni, with different Co/Ni ratios

(CoN-NC). The CoNi-NC catalysts exhibit a total current density as high as 74 mA/cm^2 at −1.0 V_{RHE} with tunable CO/H_2 ratios (ranging from 0.23 to about 3.30) and with the sum of CO and H_2 faradaic efficiencies almost equal to 100 %.

Starting from the above-mentioned study, a modification of the previous synthesis with lower temperature has been carried out, in order to produce a bimetallic single atom catalyst, consisting of Co and Zn atoms dispersed on a carbon support and coordinated to N atoms, named as ZnCo-NC. Zn atoms, indeed, have never been adopted in such a combination, although previous literature studies have shown their good activity towards the catalysis of the CO_2RR to CO (Yang F. et al., 2018) whereas Co single atoms demonstrated their selectivity towards HER (Daiyan et al., 2020). N atoms contribute to increasing the activity and stability of the metal single atoms by coordinating with them to form peculiar active centers. On the other hand, it is undeniable the contribution to the whole activity and stability given by carbonaceous supports (Varela et al., 2019). Indeed, these supports can stably incorporate single metal atoms within their structure through their vacancies and defects avoiding their agglomeration and, unlike metal oxides, possess intrinsic conductivity, which makes them suitable for electrochemical reactions being able to enhance electron transfer (Sahoo et al., 2019; Yang S. et al., 2017). In particular, several studies reported the beneficial effect of the presence of carbon supports, which can control the adsorption energy on metal centers through local electron density modification due to electrons donation or withdrawal (Ramaswamy et al., 2013; Jiang et al., 2016; Wang et al., 2019)

4.2 Materials and methods

4.2.1 ZnCo-NC SAC preparation

Firstly, glucose (0.125 g) and dicyandiamide (DICY, 2.5 g) were dissolved in 100 mL of deionized water. Afterward, two aqueous solutions containing the transition metal precursors, i.e. 1mL of 0,00625 M of cobalt (II) chloride hexahydrate ($CoCl_2 \cdot 6H_2O$) and 1mL of 0.00625 M of zinc (II) chloride anhydrous ($NiCl_2$) were added dropwise to the solution. The mixture was then stirred and air-dried overnight in order to let the water evaporate and the final product was smashed into powder. The above-mentioned powder was placed in a crucible with a cover and underwent pyrolysis in a tubular furnace after being heated with a rate of 3 °C/min till 800 °C and then maintained at this temperature for 1 hour under nitrogen flow (100 mL/min). Eventually, the sample was recovered from the crucible, after being quickly cooled down to room temperature.

4.2.2 Methods

Field emission scanning electron microscopy (FESEM) images were acquired through a LEO 1525 electron microscope, equipped with an energy dispersive X-ray (EDX) probe. Raman spectrum of the sample was recorded with a Renishaw inVia spectrometer at a 514 nm wavelength. A Leica DMLM optical microscope connected on-line with the instrument allowed to collect optical images. Moreover, thermogravimetric analysis (TGA) was carried out by means of a SDTQ 600 Analyzer (TA Instruments) with a 3 K/min heating rate under nitrogen flow in order to study the pyrolysis steps.
Before performing electrochemical tests, 1 mg of the sample was dispersed in a mixed solution of deionized water (0.7 mL), isopropyl alcohol (0.2 mL) and 0.5 wt% Nafion solution (0.1 mL), followed by sonication for 30 minutes to form a homogeneous ink. Afterward, the catalyst ink was loaded onto a glassy carbon electrode adopted as the working electrode and dried at room temperature. Electrochemical experiments were carried out by means of an Autolab PGSTAT302N potentiostat equipped with a FRA32M frequency response analyzer module. The electrolytic cell consisted of a three-electrode setup. Indeed, a SPE would have not been a good choice for this reaction since the closeness between working and counter electrodes would have surely led to the re-oxidation of products. As above-mentioned, glassy carbon was used as the working electrode, while saturated calomel electrode (SCE) was chosen as the reference electrode and platinum wire was adopted as the counter electrode. The potentials were converted to the reversible hydrogen electrode (RHE) by the Nerst equation at 25 °C (eq. (9)):

$$E_{RHE} = E_{SHE} + 0.0591 \cdot pH + 0.241\ V \quad (9)$$

The adopted electrolytic solution was a 0.5 M $KHCO_3$ solution with pH=8.5. For the measurements with CO_2, 10 mL/min of gas were bubbled for 30 minutes in the electrolytic cell before the test started. Lastly, the output gas was examined through a gas chromatography-mass spectrometry analysis, through a Thermo Scientific FOCUS GC-ISQ Single Quadrupole MS equipped with a TG-POLAR capillary column (0.25 μm×0.25 mm×60 m).

4.3 Results and discussion for ZnCo-NC

4.3.1 Characterization

SEM images, in Figure 86, showed the existence of a three-dimensional network of porous carbonaceous support. Moreover, the corresponding EDX

maps in Figure 87 confirmed the existence of Co, Zn and N elements on the carbon support, along with oxygen, probably due to the adsorption of H_2O vapors on the support itself. By looking at the maps, it is worth noticing that the Co and Zn maps cannot be superimposed, suggesting the presence of two separated active centers, comprising Co and Zn for the catalysis of CO_2RR to CO and HER, respectively.

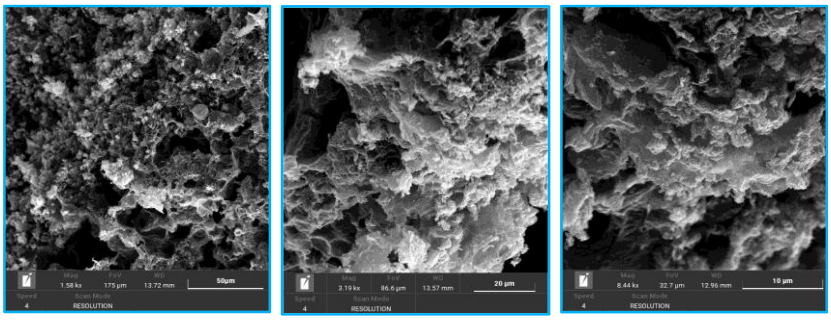

Figure 86. *SEM images of ZnCo-NC at different magnifications (scale bars: 50, 20 and 10µm)*

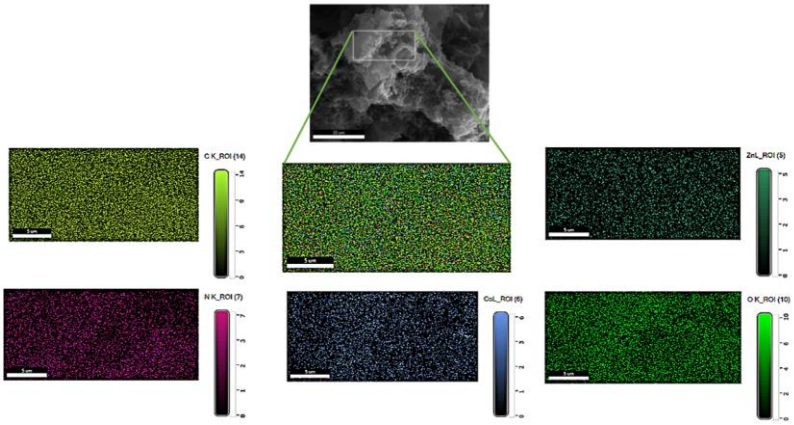

Figure 87. *SEM image of ZnCo-NC (scale bar: 20 µm) and corresponding EDX maps*

Raman spectroscopy was also carried out on the sample in order to understand the nature and the grade of the order of the graphitic support. The spectrum, reported in Figure 88, exhibited the typical bands of graphitic carbonaceous materials, namely the D band (at about 1355 cm^{-1}), the G band (at about 1560 cm^{-1}) and the 2D band (at about 2850 cm^{-1}). I_D/I_G ratio (I_G=621,652; I_D=532: I_D/I_G=0.86) is 0.86, suggesting a rather high level of

disorder of the material, therefore the possible presence of defects on it which could act as anchoring sites for the atomic metal centers.

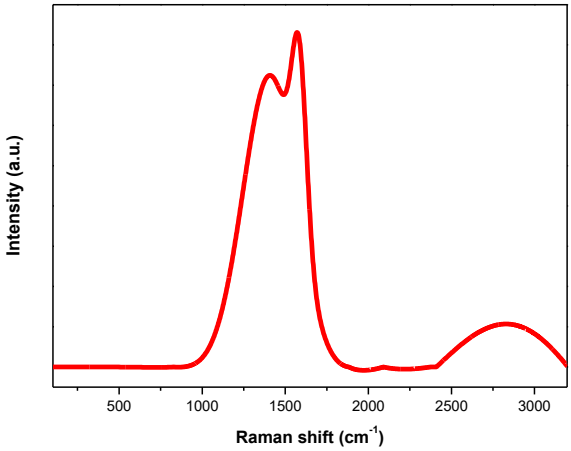

Figure 88. *Raman spectrum of ZnCo-NC*

In Figure 89, the TGA curve of the mixed powder of $CoCl_2 \cdot 6H_2O$, $NiCl_2$, glucose and DICY is reported. Since the test parameters were the same as the ones of the pyrolysis in the tubular furnace (i.e. from room temperature to 800 °C at a heating rate of 3 C°/min under a 100 mL/min nitrogen flow) this characterization is particularly interesting in order to prove what happened to the powder during thermal treatment. After a weight loss due to adsorbed water and crystal water between 100 °C and 200 °C, the main weight loss is in the range of 230-800 °C and it is due to the decomposition of dicyandiamide, along with the calcination of the small percentage of glucose present in the powder. A previous study on their decomposition (Liu et al., 2018) proved that, in the range 550-750 °C, DICY assembles into graphitic carbon nitride (g-C_3N_4) which serves as a template to guide the condensation of graphene patches derived from glucose calcination between its layers. Onto g-C_3N_4 layers, nitrogen atoms with lone-pair electrons attract Co and Zn metal atoms, creating active centers which will eventually move to the carbon support at a temperature higher than 750 °C, when the remaining g-C_3N_4 will completely decompose. The residue at 800 °C is the catalyst.

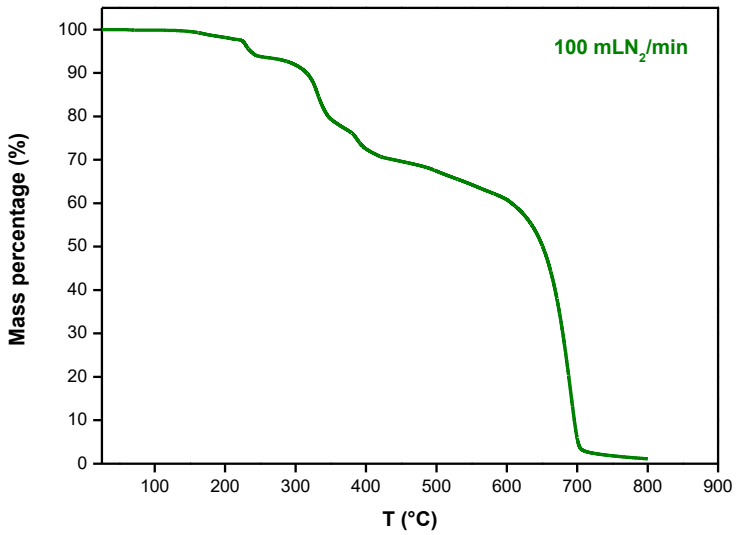

Figure 89. *TGA curve of the mixed powder of metal from room temperature to 800 °C at a heating rate of 3 C°/min under a 100 mL/min nitrogen flow*

4.3.2 Electrochemical tests

In Figure 90, polarization curves of the glassy carbon support and the ZnCo-NC catalyst at 10mV/sec in a 0.5 M $KHCO_3$ solution both with and without CO_2 bubbling are reported. From the graphs, it is clearly visible that the onset potential of the catalyst is much lower than the one of pure glassy carbon in both the $KHCO_3$ and CO_2-saturated $KHCO_3$ solutions. Indeed, in both solutions, ZnCo-NC exhibited negligible values of around -0.2 V *vs.RHE*. What is also worth noticing is that the similarity between the curves obtained with and without the CO_2 bubbling in the $KHCO_3$ solution was probably due to a smaller amount of already dissolved CO_2 from the carbonate equilibrium, as the HCO_3^- anion exists in solution at pH of around 8 and the CO_2 bubbling process did not change such pH significantly (Zhong et al., 2014). Furthermore, as can be better inferred from Figure 91, in which cyclic voltammograms both in a CO_2-saturated environment and without CO_2 are reported, the cathodic current of ZnCo-NC markedly increased in the presence of CO_2, reaching 60 mA/cm^2 at -1.16 V *vs.RHE* in the CO_2-saturated $KHCO_3$ solution. The steep increase in current density, as well as the difference between the curves, proved that the catalyst is sensitive to an increase of CO_2 in the solution, suggesting its efficiency towards CO_2RR to CO.

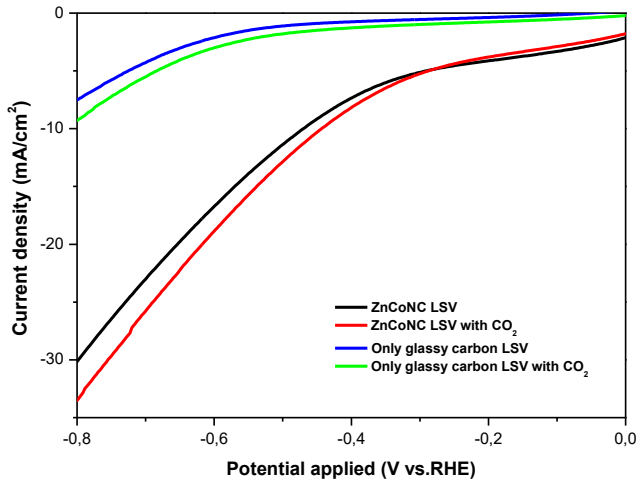

Figure 90. *Polarization curves of the glassy carbon support and the ZnCo-NC catalyst at 10 mV/sec in a 0.5 M $KHCO_3$ solution both with and without CO_2*

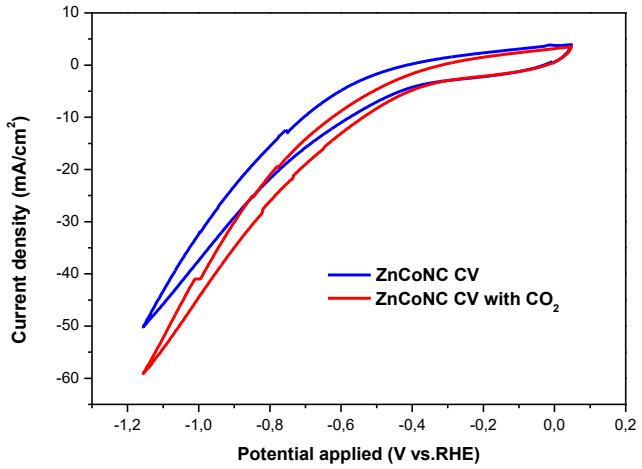

Figure 91. *Cyclic voltammetry curves of ZnCo-NC catalyst at 50 mV/sec in a 0.5 M $KHCO_3$ solution both with and without CO_2*

However, cyclic voltammograms alone cannot provide conclusive evidence for the occurred CO_2 reduction. Therefore, the CO_2 reduction products in the gas phase were quantitatively analyzed using gas chromatography/mass spectrometry (GC-MS), by withdrawals in the CO_2-saturated electrolytic solution every 30-minutes electrolysis under increasing

constant potentials. From the GC-MS analysis it emerged that the only recovered gaseous products are CO and H_2 and the syngas obtained showed a CO/H_2 ratio ranging widely from about 23 to 0.2 in the potential range -0.3÷ -1 V *vs.RHE* (see Figure 92).

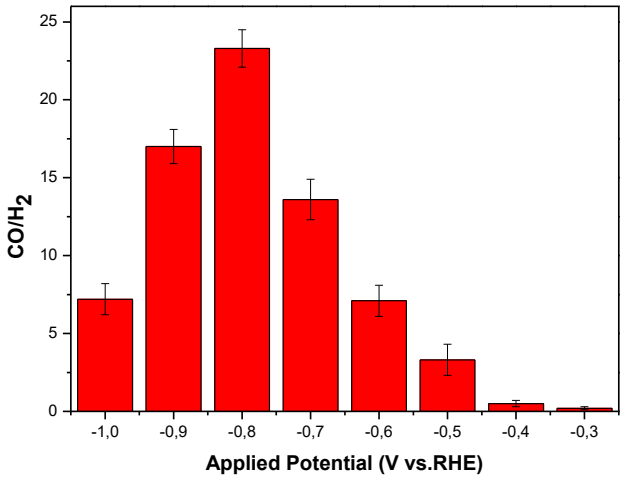

Figure 92. *Experimental measured CO/H_2 ratio at different applied potentials in the range -0.3÷1 V vs.RHE.*

In Table 5, a comparison of the synthesized catalyst with the most performing SACs in current literature is reported, showing the excellent performance of ZnCo-NC, whose onset potential and maximum current density values are some of the lowest and the highest, respectively, and whose CO_2/H_2 ratio varies in a very wide range as applied potential changes, which means that the obtained syngas could be adopted as feedstock to several industrial processes, such as Fischer-Tropsch, methanol and ethanol synthesis processes (Hernández et al., 2017).

Table 5. *Comparison between ZnCo-NC and the most recent metal SACs for the CO and syngas electro-production from CO_2 in aqueous electrolyte solution at ambient pressure and temperature*

Catalyst	Max total current density [mA/cm^2]	CO/H_2 ratio	Ref.
Ni-N-C	~25 at – 0.95 V	-	Hu et al., 2018
Ni-N-Gr	~4 at -2.20 V	-	Su et al., 2016
Ni-NG	~28 at -0.90 V	-	Jiang et al., 2018
SA-Ni/N-CS	~32 at -1.20 V	-	Yuan et al., 2020
Ni-N_4-C	36.20 at −0.91 V	-	Li et al., 2017
Ni SACs/N-C	20 at -1.20 V	-	Zhao et al., 2017
Ni-N-MEGO	~25 at -0.76 V	-	Cheng et al., 2018a
NiSA-N-CNT	~36 at – 0.65 V	-	Cheng et al., 2018b
Ni-CTF	4.50 at -1.20 V	-	Su et al., 2018
NiSAC/NiNP CNRs	~13÷~27.5 in the range -0.60 V÷-0.80 V	0.11÷19	Zhu W. et al., 2020
Ni/NCNTs-50	~50 at -1.20 V	-	Hou et al., 2020
Co-N_2	~45 at -0.90 V	-	Wang X. et al., 2018
Co-HNC	~25 at -1.40 V	It remains stable at 0.5 in the potential range -0.7 ÷ -1 V.	Song et al., 2018
Co-N_5/HNPCSs	~18 at -0.90 V	-	Pan Y. et al., 2018
Co-N-C	18 at -0.88 V	-	Pan F. et al., 2018b

Co@CoNC-900	~8 at -0.80 V	4÷1	Daiyan et al., 2020
CoSA-N-CNT	-	-	Cheng et al., 2018b
CoFeSA-N-CNT	-	-	Cheng et al., 2018b
Fe-N-G/bC	~33 at -1.20 V	-	Zhang C. et al., 2018
Fe/NG-750	~7.30 at -0.80 V	-	Zhang H. et al., 2018
Fe–N/CNF-2	~18 at -0.80 V	-	Cheng et al., 2018c
Fe-N-C	~15 at -0.90 V	-	Pan F. et al., 2018a
C-AFC©ZIF-8	~23 at -0.85 V	-	Ye et al., 2017
Fe–N–C-0.5	~20 at -0.90 V	-	Wu et al., 2020
Fe-SA/NCS-700	~35 at -1.35 V	-	Zhu Y. et al., 2020
Fe-N-C	~11 at -1.20 V	0.25÷ ~3	Zhao et al., 2020
Fe-N-C	~18 at -0.88 V	-	Pan F. et al., 2018b
$Fe_{0.5}$d	~19 at -0.90 V	0.2÷4	Huan et al., 2017
AD-Sn/N-C1000	~17.60 at -1 V	-	Zhao et al., 2018
Pd-NC	-	-	He et al., 2020b
Ag_2-G	44.30 at -1 V	--	Li et al., 2020
Cr-N-C	13 at -1 V	-	Pan F. et al., 2018b
Mn-N-C	~7.50 at -0.95 V	-	Pan F. et al., 2018b
Mn-C_3N_4/CNT	~38 at – 0.90 V	-	Feng et al., 2020

Ni/Fe-N-C	23.70 at -1 V	-	Ren et al., 2019
Cu–N_4–NG	~9 at -1.30 V	-	Xu et al., 2020
Cu-N-C (H-type cell)	~22 at -1.10 V	-	Chen et al., 2021
Cu-N_4-C/1100	~15 at -1.20 V	-	Cheng et al., 2021
ZnN_x/C	~37.50 at -1.10 V	-	Yang F. et al., 2018
CoNi-NC	~74 at -1 V	0.23÷ ~3.30	He et al., 2020
ZnCo-NC	60 at -1.16 V	0.3÷23	This work

Conclusions

In conclusion, the following PhD thesis aimed at answering some of the most relevant and critical issues in the field of energetic sustainability, namely related to green hydrogen production and to atmospheric carbon dioxide reduction and revalorization, by adopting the typical approaches of Nanotechnology to catalysis of water and/or carbon dioxide electrolysis at ambient conditions. In particular, the necessity of advancement, in terms of catalyst efficiency and stability, with respect to the current state-of-the-art nanomaterials for the catalysis of the hydrogen evolution reaction, i.e. the cathodic half-reaction of water splitting, was the first objective to reach. Therefore, in order to meet this goal, the first part of the project focused on the design of novel nano-structured catalysts for the HER with the intention of (i) adopting a reduced amount of platinum, a too much expensive and scarcely available although necessary metal, and (ii) studying new combinations of small quantities of other metals with platinum, as well as by adopting more economic and, at the same time, highly efficient supports. Therefore, two new nano-electrocatalysts were synthesized, PtRh and PtRh/MoS_2, with a scalable, simple, and cost-effective bottom-up wet chemistry synthesis approach. The as-prepared catalysts were tested towards HER, proving to be more efficient than most of the current HER catalysts reported in the literature so far, with some of the lowest overpotentials and Tafel slopes. This experimental campaign led to publishing a study in the *Chemical Engineering Journal* (Sarno M. et al., 2019b), which proved the efficiency and versatility of the as-prepared nanomaterials, capable not only of effectively catalyzing the HER but showing excellent performance towards the methanol oxidation reaction (MOR) as well.

In the second part of the thesis, the focus has been placed on the catalysis of the same reaction under the same conditions with the exception of the substitution of the typical acid electrolyte solution with real seawater in the electrolytic cell. The adoption of readily available and highly conductive seawater in the process of green hydrogen electro-production represents,

indeed, a real opportunity to significantly reduce the production costs and the complexity of the process itself. However, a mature state of the art on the topic is still missing because the hundreds of different impurities of seawater can easily induce catalyst poisoning (especially when it comes with platinum-based catalysts), hence the catalysts prepared for the "conventional" HER do not represent the most suitable choice. Therefore, efforts have been devoted to designing two novel nano-structured catalysts capable of efficiently working in seawater and exhibiting high stability in the new electrolytic environment, such as a trimetallic alloy (NiRuIr_G) and a quaternary nanostructure (RuOs_G), both supported on graphene. Once again, they were synthesized through a wet-chemistry, easily reproducible and scalable synthesis approach, and the as-prepared catalysts were tested in an electrolytic cell with seawater, showing remarkable performance when compared to the data available in the current scientific literature and platinum itself, especially when it comes to stability, with NiRuIr_G maintaining a constant current density at 0.23 V *vs. RHE* for over 200 hours of test. This last catalyst was, indeed, the object of a study published in the *Electrochemistry Communications* journal (Sarno M. et al., 2020).

Eventually, during the third year, a parallel, but at the same time, equally relevant step forward towards sustainability has been taken, by focusing on an evolution of the distilled water splitting, which also involves the co-electrolysis of a detrimental greenhouse gas, such as CO_2. This process would enable, indeed, both the reduction of the carbon footprint and the valorization of the captured CO_2 through its conversion, along with water, into a mixture of carbon monoxide and hydrogen, i.e. a syngas with a more easily tunable CO/H_2 ratio for its application as upstream feed to several industrial processes. From an accurate search and evaluation of the available scientific literature on the most efficient catalysts adopted for the process, it emerged that catalytic activity and stability can be significantly increased by turning from metal-based nano-sized catalysts to metal single atom catalysts (SACs) in the M-N-C form. Since the literature on this cutting-edge topic is still limited, mainly focusing on the synthesis of single atoms of a sole metal on a N-C support, the aim of the last part of this project was to explore a new route, consisting of regulating the H_2 and CO production by preparing two metals on the same carbonaceous support with dual N-M active sites. Following this idea, a novel dual-active sites single atom catalyst for the syngas electro-production has been prepared through a simple pyrolysis method, adopting nontoxic glucose as carbon precursor and very small quantities of two economic metals, namely zinc and cobalt. The as-prepared catalyst, named as ZnCo-NC, showed higher performance than most of the current catalysts reported in the literature.

As for future perspectives, especially regarding syngas electro-production, further research must be surely carried out, both in terms of new formulations of the prepared catalyst and choice of different electrochemical

systems. Regarding the first approach, an interesting idea would be to change the relative proportion of the metals in the catalyst, evaluating the influence of the new formulations on the CO/H_2 ratio of the final product. This could be of practical relevance since, as previously mentioned, mixtures with different relative percentages of CO and H_2 could be used as feedstock for the synthesis of different chemicals. As for the second approach, it is worth mentioning that experiments were carried out in a standard electrolytic cell with a typical three-electrode set-up. In this case, scaled-up conditions are not reproducible due to inefficient mass transport phenomena, poor mixing, additional losses due to membrane resistance, and very low current densities. Furthermore, without separation between cathodic and anodic compartments, it is likely that reduction products could be re-oxidized at the anode, hence lowering the catalyst performance. In order to verify the effectiveness of the catalysts on a scaled-up electrochemical environment, flow-reactors such as membrane reactors and microfluidic reactors could be adopted for tests on the prepared catalyst, along with incorporating the catalyst within GDE in order to solve the CO_2 solubility limitations, hence coming closer to a possible industrial-scale application of the synthesized nanomaterial.

Conclusions

Bibliography

Abdel-Aal H. K., K. M. Zohdy and M. Abdel Kareem (2010) Hydrogen Production Using Sea Water Electrolysis. *Open Fuel Cell J.*, **3**, 1-7. DOI: 10.2174/1875932701003010001

Allied Market Research (2021) Green Hydrogen Market Outlook: 2028. https://www.alliedmarketresearch.com/green-hydrogen-market-A11310

Arul Raj I. and K. I. Vasu (1990) Transition metal-based hydrogen electrodes in alkaline solution — electrocatalysis on nickel based binary alloy coatings. *J. Appl. Electrochem.*, **20**, 32-38. https://doi.org/10.1007/BF01012468

Asset T., S. T. Garcia, S. Herrera, N. Andersen, Y. Chen, E. J. Peterson, I. Matanovic, K. Artyushkova, J. Lee, S. D. Minteer, S. Dai, X. Pan, K. Chavan, S. C. Barton, P. Atanassov (2019) Investigating the Nature of the Active Sites for the CO_2 Reduction Reaction on Carbon-Based Electrocatalysts. *ACS Catal.*, **9**, 7668-7678. https://doi.org/10.1021/acscatal.9b01513

Badawy W. A, H. E. Feky, N. H. Helal and H. H. Mohammed (2013) Cathodic hydrogen evolution on molybdenum in NaOH solutions. *Int. J. Hydrog. Energy*, **38**, 9625-9632. https://doi.org/10.1016/j.ijhydene.2013.05.098

Bagger A., W. Jub, A. S. Varela, P. Strasser and J. Rossmeisl (2017) Single site porphyrine-like structures advantages over metals for selective electrochemical CO_2 reduction. *Catal. Today*, **288**, 74-78. https://doi.org/10.1016/j.cattod.2017.02.028

Basu S., S. J. Lehman, J. B. Miller, A. E. Andrews, C. Sweeney, K. R. Gurney, X. Xu, J. Southon and P. P. Tans (2020) Estimating US fossil fuel CO_2 emissions from measurements of ^{14}C in atmospheric CO_2. *Proc. Natl. Acad. Sci. USA*, **117**, 13300-13307. https://doi.org/10.1073/pnas.1919032117

BCC Publishing (2018) BCC Research Reference Staff Reports. Syngas Chemicals: Global Markets to 2022.

Benson E. E., C. P. Kubiak, A. J. Sathrum and J. M. Smieja (2009) Electrocatalytic and homogeneous approaches to conversion of CO2to liquid fuels. *Chem. Soc. Rev.*, **38**, 89-99. https://doi.org/10.1039/B804323J

Bloomberg (2017) One of the Rarest Precious Metals Is on Best Run in a Decade. https://www.bloomberg.com/news/articles/2017-03-07/one-of-the-rarest-precious-metals-is-on-the-best-run-in-a-decade.

Centi G. and S. Perathoner (2009) Opportunities and prospects in the chemical recycling of carbon dioxide to fuels. *Catal. Today*, **148**, 191-205. https://doi.org/10.1016/j.cattod.2009.07.075

Chen C. H., D. Wu, Z. Li, R. Zhang, C. G. Kuai, X. R. Zha, C. K. Dong, S. Z. Qiao, H. Liu and X. W. Du (2019) Ruthenium-Based Single-Atom Alloy with High Electrocatalytic Activity for Hydrogen Evolution. *Adv. Energy Mater.,* **9**, 1803913. https://doi.org/10.1002/aenm.201803913

Chen I. W. P., C. H. Hsiao, J. Y. Huang, Y. H. Peng and C. Y. Chang (2019) Highly Efficient Hydrogen Evolution from Seawater by Biofunctionalized Exfoliated MoS_2 Quantum Dot Aerogel Electrocatalysts That Is Superior to Pt. *ACS Appl. Mater. Interfaces*, **11**, 14159-14165. https://doi.org/10.1021/acsami.9b02582

Chen M., J. Kim, J. P. Liu, H. Fan and S. Sun (2006) Synthesis of FePt Nanocubes and Their Oriented Self-Assembly. *J. Am. Chem. Soc.*, **128**, 7132-7133. https://doi.org/10.1021/ja061704x

Chen M., J. P. Liu and S. Sun (2004) One-Step Synthesis of FePt Nanoparticles with Tunable Size. *J. Am. Chem. Soc*., **126**, 8394-8395. https://doi.org/10.1021/ja047648m

Chen S., Y. Li, Z. Bu, F. Yang, J. Luo, Q. An, Z. Zeng, J. Wang and S. Deng (2021) Boosting CO_2-to-CO Conversion on a Robust Single-Atom Copper Decorated Carbon Catalyst by Enhancing Intermediate Binding Strength. *J. Mater. Chem. A*, **9**, 1705-1712. https://doi.org/10.1039/D0TA08496D

Chen Y., C. W. Li and M. W. Kanan (2012) Aqueous CO_2 Reduction at Very Low Overpotential on Oxide-Derived Au Nanoparticles. *J. Am. Chem. Soc.*, **134**, 19969-19972. https://doi.org/10.1021/ja309317u

Cheng H., X. Wu, X. Li, X. Nie, S. Fan, M. Feng, Z. Fan, M. Tan, Y. Chen and G. He (2021) Construction of atomically dispersed Cu-N_4 sites via engineered coordination environment for high-efficient CO_2 electroreduction. *Chem. Eng. J.*, **407**, 126842. https://doi.org/10.1016/j.cej.2020.126842

Cheng Q., K. Mao, L. Ma, L. Yang, L. Zou, Z. Zou, Z. Hu and H. Yang (2018c) Encapsulation of Iron Nitride by Fe−N−C Shell Enabling Highly Efficient Electroreduction of CO_2 to CO. *ACS Energy Lett.*, **3**, 1205-1211. https://doi.org/10.1021/acsenergylett.8b00474

Cheng Y., S. Zhao, B. Johannessen, J. P. Veder, M. Saunders, M. R. Rowles, M. Cheng, C. Liu, M. F. Chisholm, R. De Marco, H. M. Cheng, S. Z. Yang and S. P. Jiang (2018b) Atomically Dispersed Transition Metals on

Carbon Nanotubes with Ultrahigh Loading for Selective Electrochemical Carbon Dioxide Reduction. *Adv. Mater.*, **30**, Zhang. https://doi.org/10.1002/adma.201706287

Cheng Y., S. Zhao, H. Li, S. He, J. P. Veder, B. Johannessen, J. Xiao, S. Lu, J. Pan, M. F. Chisholm, S. Z. Yang, C. Liu, J. G. Chen and S. P. Jiang (2018a) Unsaturated edge-anchored Ni single atoms on porous microwave exfoliated graphene oxide for electrochemical CO_2. *Appl. Catal. B Environ.*, **243**, 294-303. https://doi.org/10.1016/j.apcatb.2018.10.046

Clark E. L., C. Hahn, T. F. Jaramillo and A. T. Bell (2017) Electrochemical CO_2 Reduction over Compressively Strained CuAg Surface Alloys with Enhanced Multi-Carbon Oxygenate Selectivity. *J. Am. Chem. Soc.*, **139**, 15848-15857. https://doi.org/10.1021/jacs.7b08607

Cobo S., J. Heidkamp, P. A. Jacques, J. Fize, V. Fourmond, L. Guetaz, B. Jousselme, V. Ivanova, H. Dau, S. Palacin, M. Fontecave and V. Artero (2012) A Janus cobalt-based catalytic material for electro-splitting of water. *Nat. Mater.*, **11**, 802-807. https://doi.org/10.1038/nmat3385

Cordón J., G. Jiménez-Osés, J. M. López-de-Luzuriaga and M. Monge. (2017) The key role of Au-substrate interactions in catalytic gold subnanoclusters. *Nat. Commun.*, **8**, 1657. https://doi.org/10.1038/s41467-017-01675-1.

Cortright R. D., R. R. Davda and J. A. Dumesic (2002) Hydrogen from catalytic reforming of biomass-derived hydrocarbons in liquid water. *Nature*, **418**, 964-967. https://doi.org/10.1038/news020826-5

Daiyan R., R. Chen, P. Kumar, N. M. Bedford, J. Qu, J. M. Cairney, X. Lu and R. Amal (2020) Tunable Syngas Production through CO_2 Electroreduction on Cobalt-Carbon Composite Electrocatalyst. *ACS Appl. Mater. Interfaces*, **12**, 9307-9315. https://doi.org/10.1021/acsami.9b21216

Davis S. J. and K. Caldeira (2010a) Consumption-based accounting of CO_2 emissions. *Proc. Natl. Acad. Sci. USA*, **107**, 5687-5692. https://doi.org/10.1073/pnas.0906974107

Davis S. J., K. Caldeira and H. D. Matthews (2010b) Future CO_2 Emissions and Climate Change from Existing Energy Infrastructure. *Science*, **329**, 1330-1333. https://doi.org/10.1126/science.1188566

Delafontaine L., T. Asset and P. Atanassov (2020) Metal–Nitrogen–Carbon Electrocatalysts for CO_2 Reduction towards Syngas Generation. *ChemSusChem*, **13**, 1688-1698. https://doi.org/10.1002/cssc.201903281

Deng J., H. Li, J. Xiao, Y. Tu, D. Deng, H. Yang, H. Tian, J. Li, P. Ren and X. Bao (2015) Triggering the electrocatalytic hydrogen evolution activity of the inert two-dimensional MoS_2 surface *via* single-atom metal doping. *Energy Environ. Sci.*, **8**, 1594-1601. https://doi.org/10.1039/C5EE00751H

Dincer I. and C. Acar (2015) Review and evaluation of hydrogen production methods for better sustainability. *Int. J. Hydrog. Energy*, **40**, 11094-11111. https://doi.org/10.1016/j.ijhydene.2014.12.035

Doherty F., H. Wang, M. Yang and B. R. Goldsmith (2020) Nanocluster and single-atom catalysts for thermocatalytic conversion of CO and CO_2. *Catal. Sci. Technol.,***10**, 5772-5791. https://doi.org/10.1039/D0CY01316A

Domínguez-Crespo M. A., E. Ramírez-Meneses, A. M. Torres-Huerta, V. Garibay-Febles and K. Philippot (2012) Kinetics of hydrogen evolution reaction on stabilized Ni, Pt and Ni–Pt nanoparticles obtained by an organometallic approach. *Int. J. Hydrog. Energy,* **37***,* 4798-4811. https://doi.org/10.1016/j.ijhydene.2011.12.109

Ede S. R., U. Nithiyanantham and S. Kundu (2014) Enhanced catalytic and SERS activities of CTAB stabilized interconnected osmium nanoclusters. *Phys. Chem. Chem. Phys.,* **16**, 22723-22734. https://doi.org/10.1039/C4CP03068K

Elezovic N. R., V. D. Jovic and N. V. Krstajic (2005) Kinetics of the hydrogen evolution reaction on Fe–Mo film deposited on mild steel support in alkaline solution. *Electrochim. Acta*, **50**, 5594-5601. https://doi.org/10.1016/j.electacta.2005.03.037

Endrődi B., G. Bencsik, F. Darvas, R. Jones, K. Rajeshwar and C. Janáky (2017) Continuous-flow electroreduction of carbon dioxide. *Prog. Energy Combust. Sci.* **62**, 133-154. https://doi.org/10.1016/j.pecs.2017.05.005

European Commission (2020) COMMUNICATION FROM THE COMMISSION TO THE EUROPEAN PARLIAMENT, THE COUNCIL, THE EUROPEAN ECONOMIC AND SOCIAL COMMITTEE AND THE COMMITTEE OF THE REGIONS- A hydrogen strategy for a climate-neutral Europe A hydrogen strategy for a climate-neutral Europe. COM(2020) 301 final. https://ec.europa.eu/energy/sites/ener/files/hydrogen_strategy.pdf

Fang Z., B. Bueken, D. E. De Vos and R. A. Fischer (2015) Defect-Engineered Metal–Organic Frameworks. *Angew. Chem. Int. Ed.*, **54**, 7234-7254. https://doi.org/10.1002/anie.201411540

Feng J., H. Gao, L. Zheng, Z. Chen, S. Zheng, C. Jiang, H. Dong, L. Liu, S. Zhang and X. Zhang (2020) A Mn-N_3 single-atom catalyst embedded in graphitic carbon nitride for efficient CO_2 electroreduction. Nat. Commun., **11**, 4341. https://doi.org/10.1038/s41467-020-18143-y

Gao S., G. D. Li, Y. Liu, H. Chen, L. L. Feng, Y. Wang, M. Yang, D. Wang, S. Wang and X. Zou (2015) Electrocatalytic H_2 production from seawater over Co, N-codoped nanocarbons. *Nanoscale,* **7**, 2306-2316. https://doi.org/10.1039/C4NR04924A

Garg S., M. Li, A. Z. Weber, L. Ge, L. Li, V. Rudolph, G. Wang and T. E. Rufford (2020) Advances and challenges in electrochemical CO_2 reduction processes: an engineering and design perspective looking beyond new catalyst materials. *J. Mater. Chem. A,* **8**, 1511-1544. https://doi.org/10.1039/C9TA13298H

Global Monitoring Laboratory- Earth System Research Laboratories (2021) Trends in Atmospheric Carbon Dioxide. https://gml.noaa.gov/ccgg/trends/

Golgovici F., A. Pumnea, A. Petica, A. C. Manea, O. Brincoveanu, M. Enachescu and L. Anicai (2018) Chem. Pap. Ni–Mo alloy nanostructures as cathodic materials for hydrogen evolution reaction during seawater electrolysis. *Chem. Pap*. **72**, 1889-1903. https://doi.org/10.1007/s11696-018-0486-7

Gong, M., W. Zhou, M. C. Tsai, J. Zhou, M. Guan, M. C. Lin, B. Zhang, Y. Hu, D. Y. Wang, J. Yang, S. J. Pennycook, B. J. Hwang and H. Dai (2014) Nanoscale nickel oxide/nickel heterostructures for active hydrogen evolution electrocatalysis. *Nat. Commun.*, **5**, 4695. https://doi.org/10.1038/ncomms5695

Guadagno L., M. Sarno, U. Vietri, M. Raimondo, C. Cirillo and P. Ciambelli (2015) Graphene based structural adhesive to enhance adhesion performance. *RSC Advances*, **5**, 27874-27886. https://doi.org/10.1039/C5RA00819K

Hall D. S., C. Bock, B. R. MacDougall (2013). The Electrochemistry of Metallic Nickel: Oxides, Hydroxides, Hydrides and Alkaline Hydrogen Evolution. *J. Electrochem. Soc.*, **160**, F235-F243. https://doi.org/10.1149/2.026303jes

Han B., R. Lang, B. T. Qiao, A. Q. Wang and T. Zhang (2017) Highlights of the major progress in single-atom catalysis in 2015 and 2016. *Chin. J. Catal.*, **38**, 1498-1507. https://doi.org/10.1016/S1872-2067(17)62872-9

Han S. G., D. D. Ma, S. H. Zhou, K. Zhang, W. B. Wei, Y. Du, X. T. Wu, Q. Xu, R. Zou and Q. L. Zhu (2021) Fluorine-tuned single-atom catalysts with dense surface Ni-N_4 sites on ultrathin carbon nanosheets for efficient CO_2 electroreduction. *Appl. Catal. B: Environ.*, **283,** 119591. https://doi.org/10.1016/j.apcatb.2020.119591

Hansen H. A., J. B. Varley, A. A. Peterson and J. K. Nørskov (2013) Understanding Trends in the Electrocatalytic Activity of Metals and Enzymes for CO_2 Reduction to CO. *J. Phys. Chem. Lett.*, **4**, 388-394. https://doi.org/10.1021/jz3021155

He Q., D. Liu, J. H. Lee, Y. Liu, Z. Xie, S. Hwang, S. Kattel, L. Song and J. G. Chen (2020a) Electrochemical Conversion of CO_2 to Syngas with Controllable CO/H_2 Ratios over Co and Ni Single-Atom Catalysts. *Angew. Chem. Int. Ed.*, **59**, 3033-3037. https://doi.org/10.1002/anie.201912719

He Q., J. H. Lee, D. Liu, Y. Liu, Z. Lin, Z. Xie, S. Hwang, S. Kattel, L. Song and J. G. Chen (2020b) Accelerating CO_2 Electroreduction to CO Over Pd Single-Atom Catalyst. *Adv. Funct. Mater.*, **30**, 2000407. https://doi.org/10.1002/adfm.202000407

Hernández S., M. A. Farkhondehfal, F. Sastre, M. Makkee, G. Saracco and N. Russo (2017) Syngas Production from Electrochemical Reduction of

CO2: Current Status and Prospective Implementation. *Green Chem.,* **19,** 2326-2346. https://doi.org/10.1039/C7GC00398F

Hod I., M. D. Sampson, P. Deria, C. P. Kubiak, O. K. Farha and J. T. Hupp (2015) Fe-Porphyrin-Based Metal–Organic Framework Films as High-Surface Concentration, Heterogeneous Catalysts for Electrochemical Reduction of CO_2. *ACS Catal.*, 5, 6302-6309. https://doi.org/10.1021/acscatal.5b01767

Hou Y., Y. L. Liang, P. C. Shi, Y. B. Huang and R. Cao (2020) Atomically dispersed Ni species on N-doped carbon nanotubes for electroreduction of CO_2 with nearly 100% CO selectivity. *Appl. Catal. B Environ.*, **271**, 11892. https://doi.org/10.1016/j.apcatb.2020.118929

Hu X. M., H. H. Hval, E. T. Bjerglund, K. J. Dalgaard, M. R. Madsen, M. M. Pohl, E. Welter, P. Lamagni, K. B. Buhl, M. Bremholm, M. Beller, S. U. Pedersen, T. Skrydstrup and K. Daasbjerg (2018) Selective CO_2 Reduction to CO in Water using Earth-Abundant Metal and Nitrogen-Doped Carbon Electrocatalysts. *ACS Catal.*, **8**, 6255-6264. https://doi.org/10.1021/acscatal.8b01022

Huan T. N., N. Ranjbar, G. Rousse, M. Sougrati, A. Zitolo, V. Mougel, F. Jaouen and M. Fontecave (2017) Electrochemical Reduction of CO_2 Catalyzed by Fe-N-C Materials: A Structure−Selectivity Study. *ACS Catal.*, *7*, 1520-1525. https://doi.org/10.1021/acscatal.6b03353

Huang X., Z. Zeng, S. Bao, M. Wang, X. Qi, Z. Fan and H. Zhang (2013) Solution-phase epitaxial growth of noble metal nanostructures on dispersible single-layer molybdenum disulfide nanosheets. *Nat. Commun*., **4**, 1444. https://doi.org/10.1038/ncomms2472

Ida S., N. Kim, E. Ertekin, S. Takenaka and T. Ishihara (2015) Photocatalytic Reaction Centers in Two-Dimensional Titanium Oxide Crystals. *J. Am. Chem. Soc*., **137**, 239-244. https://doi.org/10.1021/ja509970z

IEA (2021) Global carbon dioxide emissions are set for their second-biggest increase in history, https://www.iea.org/news/global-carbon-dioxide-emissions-are-set-for-their-second-biggest-increase-in-history

Jiang K., S. Siahrostami, A. J. Akey, Y. B. Li, Z. Y. Lu, J. Lattimer, Y. F. Hu, C. Stokes, M. Gangishetty, G. X. Chen, Y. W. Zhou, W. Hill, W. B. Cai, D. Bell, K. R. Chan, J. K. Nørskov, Y. Cui and H. T. Wang (2017) Transition-Metal Single Atoms in a Graphene Shell as Active Centers for Highly Efficient Artificial Photosynthesis. *Chem*, **3**, 950-960. https://doi.org/10.1016/j.chempr.2017.09.014

Jiang K., S. Siahrostami, T. T. Zheng, Y. F. Hu, S. Hwang, E. Stavitski, Y. D. Peng, J. Dynes, M. Gangisetty, D. Su, K. Attenkofer and H. T. Wang (2018) Isolated Ni single atoms in graphene nanosheets for high-performance CO_2 reduction. *Energy Environ. Sci.*, **11**, 893-903. https://doi.org/10.1039/C7EE03245E

Jiang W. J., L. Gu, L. Li, Y. Zhang, X. Zhang, L. Zhang, J. Wang, J. S. Hu, Z. Wei and L. J. Wan (2016) Understanding the high activity of Fe-N-C electrocatalysts in oxygen reduction: Fe/Fe_3C nanoparticles boost the activity of $Fe\text{-}N_x$. *J. Am. Chem. Soc.*, **138**, 3570-3578. https://doi.org/10.1021/jacs.6b00757

Jouny M., W. Luc and F. Jiao (2018) General Techno-Economic Analysis of CO_2 Electrolysis Systems. *Ind. Eng. Chem. Res.*, **57**, 2165-2177. https://doi.org/10.1021/acs.iecr.7b03514

Kalogirou S. A. (2005) Seawater desalination using renewable energy sources. *Prog. Energy Combust. Sci*., **31**, 242-281. https://doi.org/10.1016/j.pecs.2005.03.001

Kibsgaard, J., Z. Chen, B. N. Reinecke and T. F. Jaramillo (2012) Engineering the surface structure of MoS_2 to preferentially expose active edge sites for electrocatalysis. *Nat. Mater.*, **11**, 963-969. https://doi.org/10.1038/nmat3439

Kim D., J. Resasco, Y. Yu, A. M. Asiri and P. Yang (2014) Synergistic geometric and electronic effects for electrochemical reduction of carbon dioxide using gold–copper bimetallic nanoparticles. *Nat. Commun*., **5**, 4948. https://doi.org/10.1038/ncomms5948

Kim, J., K. Park, D. R. Yang and S. Hong (2019) A comprehensive review of energy consumption of seawater reverse osmosis desalination plants. *Appl. Energy,* **254**, 113652. https://doi.org/10.1016/j.apenergy.2019.113652

Kitchin J. R., J. K. Nørskov, M. A. Barteau and J. G. Chen (2004) Modification of the surface electronic and chemical properties of Pt(111) by subsurface 3d transition metals. *J. Chem. Phys*., **120**, 10240-10246. https://doi.org/10.1063/1.1737365

Kong, D., H. Wang, J. J. Cha, M. Pasta, K. J. Koski, J. Yao and Y. Cui (2013) Synthesis of MoS_2 and $MoSe_2$ films with vertically aligned layers. *Nano Lett.*, **13**, 1341-1347. https://doi.org/10.1021/nl400258t

Krstajic N. and S. Trasatti (1998) Cathodic behaviour of RuO_2-doped Ni/Co_3O_4 electrodes in alkaline solutions: hydrogen evolution. *J. Appl. Electrochem.,* **28**, 1291-1297. https://doi.org/10.1023/A:1003444110172

Kuang Y., M. J. Kenney, Y. Meng, W. H. Hung, Y. Liu, J. E. Huang, R. Prasanna, P. Li, Y. Li, L. Wang, M. C. Lin, M. D. McGehee, X. Sun and H. Dai (2019) Solar-driven, highly sustained splitting of seawater into hydrogen and oxygen fuels. *Proc. Natl. Acad. Sci. USA*, **116** 6624-6629. https://doi.org/10.1073/pnas.1900556116

Kwak J. H., J. Hu, D. Mei, C. W. Yi, D. H. Kim, C. H. F. Peden, L. F. Allard and J. Szanyi (2009) Coordinatively Unsaturated Al^{3+} Centers as Binding Sites for Active Catalyst Phases of Platinum on $\gamma\text{-}Al_2O_3$. *Science*, **325**, 1670-1670. DOI: 10.1126/science.1176745

Lecuyer C., F. Quignard, A. Choplin, D. Olivier and J. M. Basset (1991) Surface Organometallic Chemistry on Oxides: Selective Catalytic

Low-Temperature Hydrogenolysis of Alkanes by a Highly Electrophilic Zirconium Hydride Complex Supported on Silica. *Angew. Chem. Int. Ed.*, **30**, 1660-1661. https://doi.org/10.1002/anie.199116601

Lee C., X. Wei, J. W. Kysar and J. Hone (2008) Measurement of the elastic properties and intrinsic strength of monolayer graphene. *Science*, **321**, 385-388. DOI: 10.1126/science.1157996

Li H., Q. Tang, B. He and P. Yang (2016) Robust electrocatalysts from an alloyed Pt–Ru–M (M = Cr, Fe, Co, Ni, Mo)-decorated Ti mesh for hydrogen evolution by seawater splitting. *J. Mater. Chem. A*, **4,** 6513-6520. https://doi.org/10.1039/C6TA00785F

Li J., X. Li, H. J. Zhai and L. S. Wang (2003) Au_{20}: A Tetrahedral Cluster. *Science*, **299**, 864-867. DOI: 10.1126/science.1079879

Li K. and D. Xue (2006) Estimation of Electronegativity Values of Elements in Different Valence States. *J. Phys. Chem. A*, **110**, 11332-11337. https://doi.org/10.1021/jp062886k

Li L., N. Zhao, W. Wei and Y. Sun (2013) A review of research progress on CO_2 capture, storage, and utilization in Chinese Academy of Sciences. *Fuel*, **108**, 112-130. https://doi.org/10.1016/j.fuel.2011.08.022

Li X., W. Bi, M. Chen, Y. Sun, H. Ju, W. Yan, J. Zhu, X. Wu, W. Chu, C. Wu and Y. Xie (2017) Exclusive Ni−N_4 Sites Realize Near-Unity CO Selectivity for Electrochemical CO_2 Reduction. *J. Am. Chem. Soc.*, **139**, 14889-14892. https://doi.org/10.1021/jacs.7b09074

Li Y. C., D. Zhou, Z. Yan, R. H. Gonçalves, D. A. Salvatore, C. P. Berlinguette and T. E. Mallouk (2016) Electrolysis of CO_2 to Syngas in Bipolar Membrane-Based Electrochemical Cells. *ACS Energy Lett.,* 1, 1149-1153. https://doi.org/10.1021/acsenergylett.6b00475

Li Y., C. Chen, R. Cao, Z. Pan, H. He and K. Zhou (2020) Dual-atom Ag_2/graphene catalyst for efficient electroreduction of CO_2 to CO. *Appl. Catal. B Environ.*, **268**, 118747. https://doi.org/10.1016/j.apcatb.2020.118747

Li Y., H. Wang, L. Xie, Y. Liang, G. Hong and H. Dai (2011) MoS_2 Nanoparticles Grown on Graphene: An Advanced Catalyst for the Hydrogen Evolution Reaction *J. Am. Chem. Soc.*, **133**, 7296-7299. https://doi.org/10.1021/ja201269b

Li, Q., L. Wu, G W., D. Su, H. Lv, S. Zhang, W. Zhu, A. Casimir, H. Zhu, A. Mendoza-Garcia, and S. Sun (2015) New Approach to Fully Ordered fct-FePt Nanoparticles for Much Enhanced Electrocatalysis in Acid. *Nano Lett.*, **15**, 2468-2473. https://doi.org/10.1021/acs.nanolett.5b00320

Lim, S. C., C. Y. Chan, K. T. Chen, K and H. Y. Tuan (2019) Synthesis of popcorn-shaped gallium-platinum ($GaPt_3$) nanoparticles as highly efficient and stable electrocatalysts for hydrogen evolution reaction. *Electrochim. Acta,* **297**, 288-296. https://doi.org/10.1016/j.electacta.2018.11.152

Lin S., H, Zhao, L. Zhu, T. He, S. Chen, C. Gao, and L. Zhang (2021) Seawater desalination technology and engineering in China: A review. *Desalination*, **498**, 114728. https://doi.org/10.1016/j.desal.2020.114728

Ling T., D. Y. Yan, Y. Jiao, H. Wang, Y. Zheng, X. Zheng, J. Mao, X. W. Du, Z. Hu, M. Jaroniec and S. Z. Qiao (2016) Engineering surface atomic structure of single-crystal cobalt (II) oxide nanorods for superior electrocatalysis. *Nat. Commun*., **7**, 12876. https://doi.org/10.1038/ncomms12876

Liu D., C. Wu, S. Chen, S. Ding, Y. Xie, C. Wang, T. Wang, Y. A. Haleem, Z. ur Rehman, Y. Sang, Q. Liu, X. Zheng, Y. Wang, B. Ge, H. Xu, Li Song (2018) In situ trapped high-density single metal atoms within graphene: Iron-containing hybrids as representatives for efficient oxygen reduction. *Nano Res.,* **11***,* 2217-2228. doi:10.1007/s12274-017-1840-8

Liu D., L. Li and T. You (2017) Superior catalytic performances of platinum nanoparticles loaded nitrogen-doped graphene toward methanol oxidation and hydrogen evolution reaction. *J. Colloid Interface Sci*., **487**, 330-335. https://doi.org/10.1016/j.jcis.2016.10.038

Liu G., A. W. Robertson, M. M. J. Li, W. C. H. Kuo, M. T. Darby, M. H. Muhieddine, Y. C. Lin, K. Suenaga, M. Stamatakis, J. H. Warner and S. C. E. Tsang (2017) MoS_2 monolayer catalyst doped with isolated Co atoms for the hydrodeoxygenation reaction. *Nat. Chem.*, **9**, 810-816. https://doi.org/10.1038/nchem.2740

Liu Q., Z. Yan, N. L. Henderson, J. C. Bauer, D. W. Goodman, J. D. Batteas, R. E. Schaak (2009) Synthesis of CuPt Nanorod Catalysts with Tunable Lengths. *J. Am. Chem. Soc*., **131**, 5720-5721. https://doi.org/10.1021/ja810151r

Lu Q. and F. Jiao (2016) Electrochemical CO_2 reduction: Electrocatalyst, reaction mechanism, and process engineering. *Nano Energy* 29, 439-456. https://doi.org/10.1016/j.nanoen.2016.04.009.

Ma Y. Y., C. X. Wu, X. J. Feng, H. Q. Tan, L. K. Yan, Y. Liu, Z. H. Kang, E. B. Wang and Y. G. Li (2017) Highly efficient hydrogen evolution from seawater by a low-cost and stable CoMoP@C electrocatalyst superior to Pt/C**.** *Energy Environ. Sci.*, **10**, 788-798. https://doi.org/10.1039/C6EE03768B

Martín A. J., G. O. Larrazábal and J. Pérez-Ramírez (2015) Towards sustainable fuels and chemicals through the electrochemical reduction of CO_2: lessons from water electrolysis. *Green Chem*., **17**, 5114-5130. https://doi.org/10.1039/C5GC01893E

McCrory C. C. L., S. Jung, I. M. Ferrer, S. M. Chatman, J. C. Peters and T. F. Jaramillo (2015) Benchmarking Hydrogen Evolving Reaction and Oxygen Evolving Reaction Electrocatalysts for Solar Water Splitting Devices**.** *J. Am. Chem. Soc.,* **137**, 4347–4357 https://doi.org/10.1021/ja510442p

Möller T., W. Ju, A. Bagger, X. Wang, F. Luo, T. N. Thanh, A. S. Varela, J. Rossmeisl and P. Strasser (2019) Efficient and Selective CO_2 to CO Electrolysis on Solid NiN-C Catalysts at Industrial Current Densities. *Energy Environ. Sci.*, **12**, 640-647. https://doi.org/10.1039/C8EE02662A

Mourdikoudis S. and L. M. Liz-Marzán (2013) Oleylamine in Nanoparticle Synthesis. *Chem. Mater.* **25**, 1465-1476. https://doi.org/10.1021/cm4000476

Najafabadi A. T. (2013) CO_2 chemical conversion to useful products: An engineering insight to the latest advances toward sustainability. *Int. J. Energy Res.*, **37**, 485-499. https://doi.org/10.1002/er.3021

Neagu C., H. Jansen, H. Gardeniers, and M. Elwenspoek (2000) The electrolysis of water: An actuation principle for MEMS with a big opportunity. *Mechatron.*, **10**, 571-581. https://doi.org/10.1016/S0957-4158(99)00066-5

Niu X., Q. Tang, B. He and P. Yang (2016) Robust and stable ruthenium alloy electrocatalysts for hydrogen evolution by seawater splitting. *Electrochim. Acta*, **208**, 180-187. https://doi.org/10.1016/j.electacta.2016.04.184

Ojani R., J. B. Raoof and E. Hasheminejad (2013) One-step electroless deposition of Pd/Pt bimetallic microstructures by galvanic replacement on copper substrate and investigation of its performance for the hydrogen evolution reaction. *Int. J. Hydrog. Energy*, **38**, 92-99. https://doi.org/10.1016/j.ijhydene.2012.10.015

Oliveira R. T. S., M. C. Santos, P. A. P. Nascente, L. O. S. Bulhões and E. C. Pereira (2008) Nanogravimetric and voltammetric studies of a Pt-Rh alloy surface and its behavior for methanol oxidation. *Int. J. Electrochem. Sci.,* **3**, 970-979.

Pan F., H. G. Zhang, K. X. Liu, D. Cullen, K. More, M. Y. Wang, Z. X. Feng, G. F. Wang, G. Wu and Y. Li (2018a) Unveiling active sites of CO_2 reduction on nitrogen-coordinated and atomically dispersed iron and cobalt catalysts. *ACS Catal.*, **8**, 3116-3122. https://doi.org/10.1021/acscatal.8b00398

Pan F., W. Deng, C. Justiniano and Y. Li (2018b) Identification of champion transition metals centers in metal and nitrogen-codoped carbon catalysts for CO_2 reduction. *Appl. Catal. B Environ.*, **226**, 463-472. https://doi.org/10.1016/j.apcatb.2018.01.001

Pan Y., R. Lin, Y. Chen, S. Liu, W. Zhu, X. Cao, W. Chen, K. Wu, W. C. Cheong, Y. Wang, L. Zheng, J. Luo, Y. Lin, Y. Liu, C. Liu, J. Li, Q. Lu, X. Chen, D. Wang, Q. Peng, C. Chen and Y. Li (2018) Design of Single-Atom Co–N_5 Catalytic Site: A Robust Electrocatalyst for CO_2 Reduction with Nearly 100% CO Selectivity and Remarkable Stability. *J. Am. Chem. Soc.*, **140**, 4218-4221. https://doi.org/10.1021/jacs.8b00814

Pangarkar B. L., S. K. Deshmukh, V. S. Sapkal and R. S. Sapkal (2014). Review of membrane distillation process for water purification.

Desalin. Water Treat., **57***,* 2959-2981. https://doi.org/10.1080/19443994.2014.985728

Park K. W., J. H. Choi, B. K. Kwon, S. A. Lee, Y. E. Sung, H. Y. Ha, S. A. Hong, H. Kim, A. Wieckowski (2002) Chemical and Electronic Effects of Ni in Pt/Ni and Pt/Ru/Ni Alloy Nanoparticles in Methanol Electrooxidation. *J. Phys. Chem. B,* **106**, 1869-1877. https://doi.org/10.1021/jp013168v

Pentland N., J. O'M. Bockris and E. Sheldon (1957) Hydrogen Evolution Reaction on Copper, Gold, Molybdenum, Palladium, Rhodium, and Iron: Mechanism and Measurement Technique under High Purity Conditions. *J. Electrochem. Soc*., **104**, 182-194; DOI:10.1149/1.2428718

Qiao B., A. Wang, X. Yang, L. F. Allard, Z. Jiang, Y. Cui, J. Liu, J. Li and T. Zhang (2011) Single-Atom Catalysis of CO Oxidation using Pt_1/FeO_x. *Nat. Chem.*, **3**, 634-641. https://doi.org/10.1038/nchem.1095

Qiao B., J. X. Liang, A. Wang, C. Q. Xu, J. Li, T. Zhang and J. J. Liu (2015) Ultrastable single-atom gold catalysts with strong covalent metal-support interaction (CMSI). *Nano Res.*, **8**, 2913-2924. https://doi.org/10.1007/s12274-015-0796-9

Qiao J., Y. Liu, F. Hong, J. Zhang (2014) A review of catalysts for the electroreduction of carbon dioxide to produce low-carbon fuels. *Chem. Soc. Rev.,* **43***,* 631-675. https://doi.org/10.1039/C3CS60323G

Quaino P., F. Juarez, E. Santos and W. Schmickler (2014) Volcano plots in hydrogen electrocatalysis – uses and abuses. *Beilstein J. Nanotechnol.,* **5**, 846-854. https://doi.org/10.3762/bjnano.5.96

Ramaswamy N., U. Tylus, Q. Jia and S. Mukerjee (2013) Activity Descriptor Identification for Oxygen Reduction on Nonprecious Electrocatalysts: Linking Surface Science to Coordination Chemistry. *J. Am. Chem. Soc.*, **135**, 15443-15449. https://doi.org/10.1021/ja405149m

Raoof J. B., R. Ojani, S. A. Esfeden and S. R. Nadimi (2010) Fabrication of bimetallic Cu/Pt nanoparticles modified glassy carbon electrode and its catalytic activity toward hydrogen evolution reaction. *Int. J. Hydrog. Energy*, **35**, 3937-3944. https://doi.org/10.1016/j.ijhydene.2010.02.073

Rasamani K. D., F. Alimohammadi and Y. Sun (2017) Interlayer-expanded MoS_2. *Mater. Today*, **20**, 83-91. https://doi.org/10.1016/j.mattod.2016.10.004

Ren W., X. Tan, W. Yang, C. Jia, S. Xu, K. Wang, S. C. Smith and C. Zhao (2019) Isolated Diatomic Ni-Fe Metal–Nitrogen Sites for Synergistic Electroreduction of CO_2. *Angew. Chem. Int. Ed.*, **58**, 6972-6976. https://doi.org/10.1002/anie.201901575

Ross M. B., C. T. Dinh, Y. Li, D. Kim, P. De Luna, E. H. Sargent, P. Yang (2017) Tunable Cu Enrichment Enables Designer Syngas Electrosynthesis from CO_2. *J. Am. Chem. Soc.*, **139**, 9359-9363. https://doi.org/10.1021/jacs.7b04892

Rowley-Neale S. J., D. A. C. Brownson, G. C. Smith, D. A. Sawtell, P. J. Kelly, C. E. Banks (2015) 2D nanosheet molybdenum disulphide (MoS_2)

modified electrodes explored towards the hydrogen evolution reaction. *Nanoscale,* **7**, 18152-18168. https://doi.org/10.1039/C5NR05164A

Ruban A., B. Hammer, P. Stoltze, H. L. Skriver and J. K. Nørskov (1997) Surface electronic structure and reactivity of transition and noble metals. *J. Mol. Catal. Chem.,* **115**, 421-429. https://doi.org/10.1016/S1381-1169(96)00348-2

Sahoo S. K., Y. Ye, S. Lee, J. Park, H. Lee, J. Lee and J. W. Han (2019) Rational Design of TiC-Supported Single-Atom Electrocatalysts for Hydrogen Evolution and Selective Oxygen Reduction Reactions**.** *ACS Energy Lett.*, **4,** 126-132. https://doi.org/10.1021/acsenergylett.8b01942

Sarno M. and E. Ponticorvo (2017a) Effect of the amount of nickel sulphide, molybdenum disulphide and carbon nanosupport on a Tafel slope and overpotential optimization. *Nanotechnology*, **28**, 214003. DOI: 10.1088/1361-6528/aa6bd3

Sarno M. and E. Ponticorvo (2017b) Much enhanced electrocatalysis of Pt/PtO2 and low platinum loading Pt/PtO_2-Fe_3O_4 dumbbell nanoparticles*Int. J. Hydrog. Energy*, **42**, 23631-23638. https://doi.org/10.1016/j.ijhydene.2017.03.017

Sarno M., C. Cirillo, E. Ponticorvo and P. Ciambelli (2015) Synthesis and Characterization of Mo_2C/MoO_3 Nanohybrid as Electrocatalyst for Hydrogen Evolution Reaction. *Chem. Eng. Trans*., **43**, 943-948. https://doi.org/10.3303/CET1543158

Sarno M., D. Sannino, C. Leone and P. Ciambelli (2012) Evaluating the Effects of Operating Conditions on the Quantity, Quality and Catalyzed Growth Mechanisms of CNTs. J. *Mol. Catal. A-Chem.*, **357**, 26-38. https://doi.org/10.1016/j.molcata.2012.01.014

Sarno M., E. Ponticorvo and C. Cirillo (2016) Self-Suspended Nanoparticles for N-Alkylation Reactions: A New Concept for Catalysis*J. Phys. Chem. Solids*, **99**, 138-147. https://doi.org/10.1002/open.201900104

Sarno M., E. Ponticorvo and D. Scarpa (2019a) Controlled PtIr nanoalloy as an electro-oxidation platform for methanol reaction and ammonia detection. *Nanotechnology*, **30**, 394004. DOI: 10.1088/1361-6528/ab2c3c

Sarno M., E. Ponticorvo and D. Scarpa (2019b) PtRh and PtRh/MoS_2 nano-electrocatalysts for methanol oxidation and hydrogen evolution reactions. *Chem. Eng. J.,* **377**, 120600. https://doi.org/10.1016/j.cej.2018.12.060

Sarno M., E. Ponticorvo and D. Scarpa (2020) Active and stable graphene supporting trimetallic alloy-based electrocatalyst for hydrogen evolution by seawater splitting. *Electrochem. Commun.,* **111**, 106647 https://doi.org/10.1016/j.elecom.2019.106647

Schneider J., H. Jia, K. Kobiro, D. E. Cabelli, J. T. Muckerman and E. Fujita, E (2012) Nickel(II) macrocycles: highly efficient electrocatalysts for the selective reduction of CO_2 to CO. *Energy Environ. Sci.*, *5*, 9502-9510. https://doi.org/10.1039/C2EE22528J.

Shah M. A. (2012) Growth of uniform nanoparticles of platinum by an economical approach at relatively low temperature. *Sci. Iran*., **19**, 964-966. https://doi.org/10.1016/j.scient.2012.02.027

Sheng W., S. Kattel, S. Yao, B. Yan, Z. Liang, C. J. Hawxhurst, Q. Wu and J. G. Chen (2017) Electrochemical reduction of CO_2 to synthesis gas with controlled CO/H_2 ratios. *Energy Environ. Sci.*, **10**, 1180-1185. https://doi.org/10.1039/C7EE00071E

Shervedani R. K., A. H. Alinoori and A. R. Madram (2008) Electrocatalytic Activities of Nickel-phosphorous Composite Coating Reinforced with Codeposited Graphite Carbon for Hydrogen Evolution Reaction in Alkaline Solution. *J. New Mater. Electrochem. Syst.*, 2008, **11**, 259-265.

Song L. J. and H. M. Meng (2010) Effect of carbon content on Ni–Fe–C electrodes for hydrogen evolution reaction in seawater. *Int. J. Hydrog. Energy*, **35**, 10060-10066. https://doi.org/10.1016/j.ijhydene.2010.08.003

Song X., H. Zhang, Y. Yang, B. Zhang, M. Zuo, X. Cao, J. Sun, C. Lin, X. Li and Z, Jiang (2018) Bifunctional Nitrogen and Cobalt Codoped Hollow Carbon for Electrochemical Syngas Production. *Adv. Sci.*, **5**, 1800177. https://doi.org/10.1002/advs.201800177

Spasojevic M., N. Krstajic, P. Despotov, R. Atanasoski and K. Popov (1984) The evolution of hydrogen on cobalt-molybdenum coating: polarization characteristics. *J. Appl. Electrochem.*, **14**, 265-266. https://doi.org/10.1007/BF00618745

Speck F. D., J. H. Kim, G. Bae, A. H. Joo, K. J. J. Maryhofer, C. H. Choi and S. Cherevko (2021) Single-Atom Catalysts: A Perspective toward Application in Electrochemical Energy Conversion. *JACS Au*, **1**, 1086-1100. https://doi.org/10.1021/jacsau.1c00121

Štrbac S., I. Srejić and Z. Rakočević (2018) Electrocatalysis of Hydrogen Evolution Reaction on Au(111) by Spontaneously Deposited Iridium in Acid Solution. *J. Electrochem. Soc.* **165**, J3335-J3341. DOI: 10.1149/2.0441815jes

Su P., K. Iwase, T. Harada, K. Kamiya and S. Nakanishi (2018) Covalent triazine framework modified with coordinatively-unsaturated Co or Ni atoms for CO electrochemical reduction. *Chem. Sci*., **9**, 3941-3947. https://doi.org/10.1039/C8SC00604K

Su, P., K. Iwase, S. Nakanishi, K. Hashimoto and K. Kamiya (2016) Nickel-Nitrogen-Modified Graphene: An Efficient Electrocatalyst for the Reduction of Carbon Dioxide to Carbon Monoxide. *Small*, **12**, 6083-6089. https://doi.org/10.1002/smll.201602158

Szkaradek K., K. Buzar, E. Pidko and B. M. Szyja (2018) Supported Ru metalloporphyrins for the electrocatalytic CO_2 conversion. *ChemCatChem,* **10***,* 1814-1820. https://doi.org/10.1002/cctc.201701045

Tan W., B. Cao, W. Xiao, M. Zhang, S. Wang, S. Xie, D. Xie, F. Cheng, Q. Guo and P. Liu (2019) Electrochemical Reduction of CO_2 on Hollow

Cubic Cu_2O@Au Nanocomposites. *Nanoscale Res. Lett.*, **14,** 63. https://doi.org/10.1186/s11671-019-2892-3

The International Copper Association ICA (2017) Copper demand for electric cars to rise nine-fold by 2027. https://www.reuters.com/article/us-copper-demand-electric-vehicles-idUSKBN1940PC

Tran P. D., T. V. Tran, M. Orio, S. Torelli, Q. D. Truong, K. Nayuki, Y. Sasaki, S. Y. Chiam, R. Yi, I. Honma, J. Barber and V. Artero (2016) Coordination polymer structure and revisited hydrogen evolution catalytic mechanism for amorphous molybdenum sulfide. *Nat. Mater.,* **15**, 640-646. https://doi.org/10.1038/nmat4588

Tripkovic V., M. Vanin, M. Karamad, M. E. Björketun, K. W. Jacobsen, K. S. Thygesen and J. Rossmeisl (2013) Electrochemical CO_2 and CO Reduction on Metal-Functionalized Porphyrin-like Graphene. *J. Phys. Chem. C,* **117***,* 9187-9195. https://doi.org/10.1021/jp306172k

Valden M., X. Lai, D. W. Goodman (1998) Onset of Catalytic Activity of Gold Clusters on Titania with the Appearance of Nonmetallic Properties. *Science,* **281**, 1647-1650. DOI: 10.1126/science.281.5383.1647

Van Santen R. A., A. De Koster and T. Koerts (1990) The quantum chemical basis of the Fischer-Tropsch reaction. *Catal. Lett.*, **7**, 1-14. https://doi.org/10.1007/BF00764488

Varela A. S., W. Ju, A. Bagger, P. Franco, J. Rossmeisl, and P. Strasser (2019) Electrochemical reduction of CO_2 on Metal-Nitrogen-doped carbon catalysts. *ACS Catal.*, **9**, 7270-7284. https://doi.org/10.1002/aenm.201703614

Veeramalai C. P., F. Li, Y. Liu, Z. Xu, T. Guo and T. W. Kim (2016) Enhanced field emission properties of molybdenum disulphide few layer nanosheets synthesized by hydrothermal method. *Appl. Surf. Sci*., **389**, 1017-1022.

Verma S., X. Lu, S. Ma, R. I. Masel and P. J. A. Kenis (2016) The effect of electrolyte composition on the electroreduction of CO_2 to CO on Ag based gas diffusion electrodes. *Phys. Chem. Chem. Phys.*, **18**, 7075-7084. https://doi.org/10.1039/C5CP05665A

Wan J., W. Chen, C. Jia, L. Zheng, J. Dong, X. Zheng, Y. Wang, W. Yan, C. Chen, Q. Peng, D. Wang and Y. Li (2018) Defect Effects on TiO_2 Nanosheets: Stabilizing Single Atomic Site Au and Promoting Catalytic Properties. *Adv. Mater.*, **30**, 1705369. https://doi.org/10.1002/adma.201705369

Wang A., J. Li and T. Zhang (2018) Heterogeneous single-atom catalysis. *Nat. Rev. Chem.*, **2**, 65-81. https://doi.org/10.1038/s41570-018-0010-1

Wang W., Q. Jia, S. Mukerjee and S. Chen (2019) Recent insights into the oxygen-reduction electrocatalysis of Fe/N/C materials. ACS *Catal.*, **9**, 10126-10141. https://doi.org/10.1021/acscatal.9b02583

Wang X., Z. Chen, X. Zhao, T. Yao, W. Chen, R. You, C. Zhao, G. Wu, J. Wang, W. Huang, J. Yang, X. Hong, S. Wei, Y. Wu and Y. Li (2018)

Regulation of Coordination Number over Single Co Sites: Triggering the Efficient Electroreduction of CO_2. *Angew. Chem. Int. Ed*., **57**, 1944-1948. https://doi.org/10.1002/anie.201712451

Waszczuk P., A. Wieckowski, P. Zelenay, S. Gottesfeld, C. Coutanceau, J. M. Léger and C. Lamy (2001) Adsorption of CO poison on fuel cell nanoparticle electrodes from methanol solutions: a radioactive labeling study. *J. Electroanal. Chem.*, **511**, 55-64. https://doi.org/10.1016/S0022-0728(01)00559-9

Weekes D. M., D. A. Salvatore, A. Reyes, A. Huang and C. P. Berlinguette (2018) Electrolytic CO_2 Reduction in a Flow Cell. *Acc. Chem. Res.*, **4**, 910-918. https://doi.org/10.1021/acs.accounts.8b00010

Weng X., Y. Liu, K. K. Wang, J. J. Feng, J. Yuan, A. J. Wang and Q. Q. Xu (2016) Single-step aqueous synthesis of AuPt alloy nanodendrites with superior electrocatalytic activity for oxygen reduction and hydrogen evolution reaction. *Int. J. Hydrog. Energy*, **41**, 18193-18202. https://doi.org/10.1016/j.ijhydene.2016.07.160

Wu S., X. Lv, D. Ping, G. Zhang, S. Wang, H. Wang, X. Yang, D. Guo and S. Fang (2020) Highly exposed atomic Fe–N active sites within carbon nanorods towards electrocatalytic reduction of CO_2 to CO. *Electrochim. Acta*, **340,** 135930. https://doi.org/10.1016/j.electacta.2020.135930

Xu, C., X. Zhi, A. Vasileff, D. Wang, B. Jin, Y. Jiao, Y. Zheng and S. Z. Qiao (2020) Highly Selective Two-Electron Electrocatalytic CO_2 Reduction on Single-Atom Cu Catalysts. *Small Structures*, **2**, 2000058. https://doi.org/10.1002/sstr.202000058

Yan D., Y. Li, J. Huo, R. Chen, L. Dai and S. Wang (2017) Defect Chemistry of Nonprecious-Metal Electrocatalysts for Oxygen Reactions. *Adv. Mater*., **29**, 1606459. https://doi.org/10.1002/adma.201606459

Yang F., P. Song, X. Z. Liu, B. B. Mei, W. Xing, Z. Jiang, L. Gu and W. L. Xu (2018) Highly efficient CO_2 electroreduction on ZnN_4-based single-atom catalyst. *Angew. Chem. Int. Ed.*, **57**, 12303-12307. https://doi.org/10.1002/anie.201805871

Yang H. B., S. F. Hung, S. Liu, K. D. Yuan, S. Miao, L. P. Zhang, X. Huang, H. Y. Wang, W. Z. Cai, R. Chen, J. J. Gao, X. F. Yang, W. Chen, W, Y. Q. Huang, H. M. Chen, C. M. Li, T. Zhang and B. Liu (2018) Atomically dispersed Ni(i) as the active site for electrochemical CO_2 reduction. *Nat. Energy*, **3**, 140-147. https://doi.org/10.1038/s41560-017-0078-8

Yang H., Q. Lin, C. Zhang, X. Yu, Z. Cheng, G. Li, Q. Hu, X. Ren, Q. Zhang, J. Liu and C. He (2020) Carbon dioxide electroreduction on single-atom nickel decorated carbon membranes with industry compatible current densities. *Nat. Commun*., **11**, 593. https://doi.org/10.1038/s41467-020-14402-0

Yang L., P. Liu, J. Li and B. Xiang (2017) Two-Dimensional Material Molybdenum Disulfides as Electrocatalysts for Hydrogen Evolution. *Catalysts*, **7**, 285-302. https://doi.org/10.3390/catal7100285

Yang S., Y. J. Tak, J. Kim, A. Soon and H. Lee (2017) Support Effects in Single-Atom Platinum Catalysts for Electrochemical Oxygen Reduction. *ACS Catal.*, **7**, 1301-1307. https://doi.org/10.1021/acscatal.6b02899

Yang X. F., A. Q. Wang, B. T. Qiao, J. Li, J. Y. Liu and T. Zhang (2013) Single-Atom Catalysts: A New Frontier in Heterogeneous Catalysis. *Acc. Chem. Res.*, **46**, 1740-1748. https://doi.org/10.1021/ar300361m

Ye Y. F., F. Cai, H. B. Li, H. H. Wu, G. X. Wang, Y. S. Li, S. Miao, S. H. Xie, R. Si, J. Wang and X. H. Bao (2017) Surface functionalization of ZIF-8 with ammonium ferric citrate toward high exposure of Fe-N active sites for efficient oxygen and carbon dioxide electroreduction. *Nano Energy*, **38**, 281-289. https://doi.org/10.1016/j.nanoen.2017.05.042

Yen P. C., R. S. Chen, C. C. Chen, Y. S. Huang and K. K. Tiong (2004) Growth and characterization of OsO_2 single crystals. *J. Cryst. Growth,* **262**, 271-276. https://doi.org/10.1016/j.jcrysgro.2003.10.021

Yu X. X., T. Y. Hua, X. Liu, Z. P. Yan, P. Xu and P. W. Du (2014) Nickel-Based Thin Film on Multiwalled Carbon Nanotubes as an Efficient Bifunctional Electrocatalyst for Water Splitting. *ACS Appl. Mater. Interfaces*, **6**, 15395-15402. https://doi.org/10.1021/am503938c

Yuan C. Z., L. Y. Zhan, S. J. Liu, F. Chen, H. J. Lin, X. L. Wu and J. R. Chen (2020) Semi-sacrificial template synthesis of single-atom Ni sites supported on hollow carbon nanospheres for efficient and stable electrochemical CO_2 reduction. *Inorg. Chem. Front.,* **7***,* 1719-1725. https://doi.org/10.1039/C9QI01688K

Zhang A., S. Yu, Y. Jiang, L. Jia, X. Xia, W. Ye and C. Wang (2015) A novel Pt@Te-reduced graphene oxide/polyimide composite catalyst for hydrogen evolution *Int. J. Hydrog. Energy* **40**, 16238-16247. https://doi.org/10.1016/j.ijhydene.2015.10.001

Zhang C., S. Yang, J. Wu, M. Liu, S. Yazdi, M. Ren, J. Sha, J. Zhong, K. Nie, A. S. Jalilov, Z. Li, H. Li, B. I. Yakobson, Q. Wu, E. Ringe, H. Xu, P. M. Ajayan and J. M. Tour (2018) Electrochemical CO_2 Reduction with Atomic Iron-Dispersed on Nitrogen-Doped Graphene. *Adv. Energy Mater.*, **8**, 1703487. https://doi.org/10.1002/aenm.201703487

Zhang H., J. Wang, Z. Zhao, H. Zhao, M. Cheng, A. Li, C. Wang, J. Wang and J. Wang (2018) The synthesis of atomic Fe embedded in bamboo-CNTs grown on graphene as a superior CO_2 electrocatalyst. *Green Chem*., **20**, 3521-3529. https://doi.org/10.1039/C8GC01466C

Zhang J., X. Wu, W. C. Cheong, W. Chen, R. Lin, J. Li, L. Zheng, W. Yan, L. Gu, C. Chen, Q. Peng, D. Wang and Y. Li (2018) Cation vacancy stabilization of single-atomic-site $Pt_1/Ni(OH)_x$ catalyst for diboration of alkynes and alkenes. *Nat. Commun.*, **9**, 1002. https://doi.org/10.1038/s41467-018-03380-z

Zhang L., J. M. T. A. Fischer, Y. Jia, X. Yan, W. Xu, X. Wang, J. Chen, D. Yang, H. Liu, L. Zhuang, M, Hankel, D. J. Searles, K. Huang, S. Feng, C. L. Brown and X. Yao (2018) Coordination of Atomic Co–Pt Coupling Species at Carbon Defects as Active Sites for Oxygen Reduction Reaction. *J. Am. Chem. Soc.*, **140**, 10757-10763. https://doi.org/10.1021/jacs.8b04647

Zhang Q., K. Kusada, D. Wu, T. Yammamoto, T. Toriyama, S. Matsumura, S. Kawaguchi, Y. Kubota and H. Kitagawa (2018) Selective control of fcc and hcp crystal structures in Au–Ru solid-solution alloy nanoparticles. *Nat. Commun.*, **9**, 510. https://doi.org/10.1038/s41467-018-02933-6

Zhang X. F., H. B. Meng, H. Y. Chen, J. J. Feng, K. M. Fang, and A. J. Wang (2019) Bimetallic PtCo alloyed nanodendritic assemblies as an advanced efficient and robust electrocatalyst for highly efficient hydrogen evolution and oxygen reduction. *J. Alloys Compd.*, **786,** 232-239. https://doi.org/10.1016/j.jallcom.2019.01.321

Zhao C., X. Dai, T. Yao, W. Chen, X. Wang, J. Wang, J. Yang, S. Wei, Y. Wu and Y. Li (2017) Ionic Exchange of Metal–Organic Frameworks to Access Single Nickel Sites for Efficient Electroreduction of CO_2. *J. Am. Chem. Soc.*, **139**, 8078-8081. https://doi.org/10.1021/jacs.7b02736

Zhao J., J. Deng, J. Han, S. Imhanria, K. Chen and W. Wang (2020) Effective tunable syngas generation via CO_2 reduction reaction by non-precious Fe-N-C electrocatalyst. *Chem. Eng. J.*, **389**, 124323. https://doi.org/10.1016/j.cej.2020.124323

Zhao Y., J. J. Liang, C. Y. Wang, J. M. Ma and G. G. Wallace (2018) Tunable and efficient tin modified nitrogen-doped carbon nanofibers for electrochemical reduction of aqueous carbon dioxide. *Adv. Energy Mater.*, **8**, 1702524-1702535. https://doi.org/10.1002/aenm.201702524

Zhong H., K. Fujii and Y. Nakano (2014) Effect of $KHCO_3$, K_2CO_3 and CO_2 on the Electrochemical Reduction of CO_2 into Organics on a Cu Electrode for the Solar Energy Conversion and Storage. *Mater. Res. Soc. Symp. Proc.,* **1640***,* 1052. https://doi.org/10.1557/opl.2014.404

Zhu C., S. Fu, Q. Shi, D. Du and Y. Lin (2017) Single-Atom Electrocatalysts. *Angew. Chem. Int. Ed.*, **56**, 13944-13960. https://doi.org/10.1002/anie.201703864

Zhu D. D., J. L. Liu and S. Z. Qiao (2016) Recent Advances in Inorganic Heterogeneous Electrocatalysts for Reduction of Carbon Dioxide. *Adv. Mater.*, **28**, 3423-3452. https://doi.org/10.1002/adma.201504766

Zhu J., L. Hu, P. Zhao, L. Y. S. Lee and K. Y. Wong (2019) Recent Advances in Electrocatalytic Hydrogen Evolution Using Nanoparticles. *Chem. Rev.,* **120**, 851-918. https://doi.org/10.1021/acs.chemrev.9b00248

Zhu L. L., H.P. Lin, Y. Y. Li, F. Liao, Y. Lifshitz, M. Sheng, S. T. Lee and M. Shao (2016) A rhodium/silicon co-electrocatalyst design concept to surpass platinum hydrogen evolution activity at high overpotentials. *Nat. Commun.*, **7**, 12272. https://doi.org/10.1038/ncomms12272

Zhu W., J. Fu, J. Liu, Y. Chen, X. Li, K. Huang, Y. Cai, Y. He, Y. Zhou, D. Su, J. J. Zhu and Y. Lin (2020) Tuning single atom-nanoparticle ratios of Ni-based catalysts for synthesis gas production from CO_2. *Appl. Catal. B Environ.*, **264**, 118502. https://doi.org/10.1016/j.apcatb.2019.118502

Zhu W., R. Michalsky, O. Metin, H. Lv, S. Guo, C. J. Wright, X. Sun, A. A. Peterson and S. Sun (2013) Monodisperse Au Nanoparticles for Selective Electrocatalytic Reduction of CO_2 to CO. *J. Am. Chem. Soc.*, **135**, 16833-16836. https://doi.org/10.1021/ja409445p

Zhu Y., X. Li, X. Wang, K. Lv, G. Xiao, J. Feng, X. Jiang, M. Fang and Y. Zhu (2020) Single-Atom Iron-Nitrogen Catalytic Site with Graphitic Nitrogen for Efficient Electroreduction of CO_2. *ChemistrySelect*, **5**, 1282-1287. https://doi.org/10.1002/slct.201904529

Zou M. S., X. Y. Guo, H. T. Huang, R. J. Yang and P. Zhang (2012) Preparation and characterization of hydro-reactive Mg–Al mechanical alloy materials for hydrogen production in seawater. *J. Power Sources*, **219**, 60-64. https://doi.org/10.1016/j.jpowsour.2012.07.008

List of simbols

Symbol	Meaning	Units
η	Reaction overpotential	V
J	Current density	A/m^2 or mA/cm^2 or mA/g
2θ	Diffraction angle	°
$E°$	Standard reduction potential	V
F	Faraday constant	s·A/mol
mol	Numbers of moles	mol
A	Active area of electrode	A
t	Electrolysis reaction time	s
FE	Faradaic efficiency	-
E_{RHE}	Potential vs. reversible hydrogen electrode	V
E_{SCE}	Potential vs. saturated calomel electrode	V
I_D	Intensity of Raman D band	-
I_G	Intensity of Raman G band	-